NASA CR-161,666

A Reproduced Copy

OF

NASA CR-161,666

Page Numbering Consistent With The Order of Original Document

NASA CONTRACTOR
REPORT

NASA CR-161666

LASER-HEATED THRUSTER - FINAL REPORT

By N. H. Kemp and R. H. Krech
Physical Sciences, Inc.
30 Commerce Way
Woburn, Massachusetts 01801

Final Report

September 1980

Prepared for

NASA - George C. Marshall Space Flight Center
Marshall Space Flight Center, Alabama 35812

(NASA-CR-161666) LASER-HEATED THRUSTER Final Report, 1 Sep. 1979 - 10 Aug. 1980 (Physical Sciences, Inc.) 157 p
HC A08/MF A01 CSCL 21d G3/20

N81-21124
Unclas
42057

1 Report No	2 Government Accession No	3 Recipient's Catalog No
NASA CR-161666		

4 Title and Subtitle	5 Report Date
LASER-HEATED THRUSTER - FINAL REPORT	September 1980
	6 Performing Organization Code

7 Author(s)	8 Performing Organization Report No
N. H. Kemp and R. H. Krech	PSI TR-220
	10 Work Unit No

9 Performing Organization Name and Address	11 Contract or Grant No
Physical Sciences, Inc. 30 Commerce Way Woburn, Massachusetts 01801	NAS8-33097
	13 Type of Report and Period Covered Contractor 1 September 1979 - 10 August 1980

12 Sponsoring Agency Name and Address	14 Sponsoring Agency Code
National Aeronautics and Space Administration Washington, DC 20546	

15 Supplementary Notes

Technical Monitor: Lee W. Jones, MSFC

16 Abstract

The objective of this research study was to develop computer codes for the design of the thrust chamber of a rocket whose propellant gas is heated by a CW laser beam. Together with the previous Interim Report (NASA CR-161665, PSI TR-205), this report documents the results of the study. Most of the work dealing with the gas properties important to CW laser propulsion is presented in the Interim Report. This report presents (1) simplified models of laser-heated thrusters which are useful for approximate parametric studies and performance mapping, (2) computer programs useful for thrust chamber design, and (3) the results of a shock tube experiment to measure the absorption coefficient of 10.6 μm radiation in hot water vapor. The simplified approximate models of laser-heated thrusters show that the average wall heating rates are within a range that can be dealt with by current rocket wall cooling techniques, and that a large fraction of the laser power can be put into the gas, compared to the energy lost to the walls. They also show that small-scale thrusters with measurable thrust can be tested using a 30 kw CW 10.6 μm laser. There are two thrust chamber design programs. One is for seeded hydrogen, with both low temperature and high temperature seeds, which absorbs the laser radiation continuously, starting at the inlet gas temperature, the second is for hydrogen seeded with cesium, in which a laser-supported combustion wave stands near the gas inlet, and heats the gas up to a temperature at which the gas can absorb the laser energy. Both programs produce physically reasonable results, though they have only been exercised on one or two sample cases. Further experience is needed with them to explore their usefulness.

Preliminary experimental results are given for the absorption coefficient of 10.6 μm radiation in water vapor at temperatures from 1100 K to 3100 K. They show values which are about 60 percent of the values obtained from the literature and used in the computer programs.

17 Key Words (Suggested by Author(s))	18 Distribution Statement
	Unclassified-Unlimited V. A. McCool Director Structures & Propulsion Lab

19 Security Classif. (of this report)	20 Security Classif. (of this page)	21 No. of Pages	22 Price
Unclassified	Unclassified	158	NTIS

ACKNOWLEDGEMENT

During the period covered by this report, computing assistance was provided by W. Jeffrey Robins and John Cronin. Dr. Robert Root advised on the formulation of the radiation models and contributed Appendix F. The experimental work was carried out with the advice of Dr. Evan Pugh, Dr. Peter Nebolsine and Dr. David Rosen. Kevin Riley provided assistance with the set-up of the shock tube facility. The technical monitor for NASA/Marshall Spaceflight Center was Mr. Lee W. Jones, whose interest and understanding proved very helpful throughout this work.

FOREWORD

This report is the second of two which have resulted from contract NAS8-33097 between Physical Sciences Inc. and the NASA Marshall Spaceflight Center, for a research study entitled "Laser-Heated Thruster." The first report is an Interim Report, dated February 1980, PSI TR-205. The present report is the Final Report PSI TR-220.

The effort accomplished under the contract, over the period September 1, 1978 through September 30, 1980, is documented in these two reports. Together they present the technical work performed. The Interim Report contains most of the work on laser absorption physics, radiation physics, thermodynamics and transport properties, and the preliminary version of the thrust chamber design computer program. In this Final Report the first five chapters contain a summary of all the work, which can serve as an Executive Summary. The nine appendices of this Final Report contain the details of additional technical work not presented in the Interim Report. The two reports should be read together to obtain complete documentation of the work accomplished.

TABLE OF CONTENTS

LIST OF FIGURES

LIST OF FIGURES (Cont.)

LIST OF FIGURES (Cont.)

LIST OF TABLES

I. INTRODUCTION

This report is the fifth in a series of reports written for NASA by Physical Sciences Inc. on the subject of CW laser propulsion and laser-heated thrusters. The first three reports were written under sponsorship of the NASA Lewis Research Center, while the fourth and the present (fifth) ones were written under sponsorship of NASA Marshall Spaceflight Center.

The first report (Ref. 1) presented a study of the mechanisms by which laser energy can be absorbed into a gas. It also reported on a study of the flow of an ideal gas in a nozzle, when undergoing laser energy absorption. The stability of this absorption process to small disturbances was also considered.

The second report (Ref. 2) dealt primarily with the flow of hydrogen which is absorbing 10.6 μm laser radiation by inverse Bremsstrahlung. The hydrogen was treated as a real gas in chemical equilibrium. The flow was quasi-one-dimensional. Radiation losses from the hot hydrogen were included by studying its radiative properties and constructing a simple model to use in the flow equations. The pure hydrogen laser-heated thruster requires the presence of a laser supported combustion (LSC) wave at the entrance to the heating chamber to provide the absorption mechanism. In Ref. 2 the properties of this wave were estimated rather crudely.

A third report (Ref. 3) focused on the structure of LSC waves in equilibrium hydrogen absorbing 10.6 μm radiation, to provide more detailed information on this important element of pure hydrogen thrusters. A one-dimensional model was constructed, including radiation losses and axial radiation transport. Several two-dimensional effects were incorporated into this one-dimensional model, including laser beam convergence and transverse conduction and radiation losses. The relation between laser intensity and mass flow per unit area into the wave was determined numerically. A one-dimensional expansion of the heated hydrogen to a nozzle throat was also calculated for one case. Peak hydrogen temperatures of 20,000 K were found in LSC waves.

These studies for NASA/Lewis led to the general conclusion that laser energy could be used to heat hydrogen in a stable manner, but the resulting gas was very hot and would lose a substantial portion of its energy by radiation. It became clear that further studies should focus on ways to reduce the heat losses and the associated wall-cooling problems.

At the same time, the sponsorship of laser propulsion work within NASA was shifted to the Marshall Spaceflight Center, under whose aegis PSI has continued their studies. The present report is the second under Marshall sponsorship, representing the final report on a two-year research study. This work has explored some alternatives to the pure hydrogen rocket, which will permit operation at lower temperature with smaller losses and less-stringent wall-cooling requirements. It has developed two-dimensional (axisymmetric) computer programs useful for the design of the thrust chamber of a laser-heated thruster.

One approach to reducing the gas temperature is to seed the hydrogen with a small amount of easily ionizable gas, such as an alkali metal-vapor. This seed will produce electrons at a much lower temperature than hydrogen. Since electrons are a necessary element for laser energy absorption by inverse Bremsstrahlung, this will permit absorption to start at a lower temperature than in pure hydrogen, and so result in a lower temperature gas. An LSC wave is still needed to heat the gas from the inlet temperature up to the temperature at which sufficient ionization has occurred to permit laser energy absorption. This LSC wave operates in seeded hydrogen, and will have a different wave speed vs. intensity relationship than a pure hydrogen LSC wave. One of the tasks in the present study was modification of the pure hydrogen LSC wave model developed in Ref. 3 to include the presence of cesium vapor seed.

A second approach to reducing the gas temperature is to seek laser energy absorbers which operate at the inlet gas temperature and continue absorbing all the laser energy as the gas temperature rises. This requires a low temperature absorber as well as a medium temperature absorber. The latter can again be an alkali metal vapor, such as cesium. The former must be a molecular absorber "tuned" to the particular laser radiation being used.

Candidate molecular absorbers were identified based on the studies of Ref. 1. A likely candidate for low temperature absorption of 10.6 μm radiation is water vapor, which will absorb this radiation until it dissociates around 4,000 K, after which the alkali metal vapor will produce enough electrons to let inverse Bremsstrahlung absorption become effective. With both low and medium temperature absorbers, there is no need for the use of the LSC wave mechanism to provide the initial gas heating. The absorption proceeds continuously from the inlet temperature until all the laser energy is absorbed. This heating mode will be referred to as continuous heating, in contrast to the LSC wave heating mode, where only medium and high temperature (hydrogen) absorbers are used.

The continuous heating mode can also be used with other laser wavelengths. For CO lasers, with radiation around 5.3 μm, Ref. 1 suggests that either NO or H_2O can function as the low temperature absorbers. In this case, there is also a molecular absorber, CO, which survives to medium temperature (at least 6,000 K), and could be used instead of the alkali metal vapor seed. It is advantageous to avoid this latter seed, if possible, because its high molecular weight reduces the rocket specific impulse.

Introducing seeds into the primary propellant gas complicates the gas storage and supply system, since it requires going from a mono-propellant to a bi-propellant or tri-propellant system, although the seeds do not have to be kept separate from the primary propellant in this case. There is another possible approach to reducing the temperature which does not require any seeds. This idea is to provide a co-flowing buffer gas around the central laser-heated hydrogen core, which can act as an insulator for the walls. After the core is heated, it will mix with the buffer and finally provide a uniformly heated gas flow at a lower temperature to be expanded and provide thrust. The buffer gas can also be hydrogen at the same inlet conditions as the core gas. The only difference is that the laser beam diameter is smaller than the gas stream diameter, so only the central part of the gas is heated by the laser. If this approach yields satisfactory specific impulse, and low enough wall heating to be handled, it is perhaps the simplest and most desirable one.

The present study was undertaken to provide the tools for assessing specific examples of these three alternate approaches to CW laser-heated thrusters. We have considered the following combinations of laser wavelength and propellant gas mixtures:

1. CO_2 (10.6 μm) radiation with H_2/Cs (LSC wave heating mode)
2. CO_2 (10.6 μm) radiation with H_2/H_2O/Cs (continuous heating mode)
3. CO (5.3 μm) radiation with H_2/CO/NO or H_2/CO/H_2O (continuous heating mode)
4. CO_2 (10.6 μm) radiation with H_2/H_2 buffer (LSC wave heating mode)

To evaluate each of these alternatives the following physical properties of the gas, mixture must be modeled:

1. Laser energy absorption properties.
2. Radiative and absorptive properties.
3. Thermodynamic and transport properties.

These gas properties must be incorporated in a gas flow model which includes the relevant effects of heating by laser energy absorption, gas radiation emission and absorption, and the usual flow effects of convection and heat transfer.

In the interim report issued under the present study (Ref. 4) most of the physical properties of the gas mixtures were presented. The absorption of 10.6 and 5.3 μm radiation by inverse Bremsstrahlung, and by water vapor, and the absorption of 5.3 μm radiation by H_2O, CO and NO were described. The radiative and absorptive properties of the important radiating species in the gas mixtures were modeled. The thermodynamic and transport properties of a mixture of hydrogen and cesium up to 20,000 K were developed, for use in LSC wave calculations. (For the other gases, in the continuous heating mode, standard chemical equilibrium codes can be used, since the temperatures of interest for continuous heating do not go much beyond 6,000 K.)

Also contained in the interim report was an axisymmetric flow model for the continuous heating mode, including a laser beam shape, and a radiation model for the particular case of a 30 atm mixture of $H_2/H_2O/Cs$ = 0.945/0.05/0.005.

The present final report presents additional work performed since August 1979. It should be looked upon as supplementary to the interim report (Ref. 4), and does not repeat the material of that report. The two reports, taken together, present the work accomplished under the present contract with NASA/MSFC.

Chapter II of this report describes some results obtained using simple flow models for the LSC wave heating and continuous heating modes. These models can be used for mapping out the regions of interesting thrusters and providing order-of-magnitude estimates of their performance and heating properties. They provide very useful simple tools for parametric evaluation of laser-heated thrusters. The details of the models are given in Appendices A, B, C and D.

Chapter III describes the axisymmetric flow thrust chamber design codes for both heating modes, as well as the LSC wave code whose output is needed for the LSC wave heating mode design code. The details of the flow models are provided in Appendices E, F, G, and H.

During the early part of the present study, a literature survey was made of the absorption coefficient of water vapor for 10.6 μm radiation. It was found that the literature showed a steep minimum near 500 K, predicted theoretically, and a number of emission experiments which tended to confirm this minimum. However, there appeared to be no laser absorption experiments on water above room temperature. Then a report appeared (Ref. 5) in which laser absorption measurements were made in a laser-heated gas. The values of absorption coefficient presented there were an order of magnitude or more above the values in the rest of the literature. In view of the importance of water vapor as a possible low temperature absorber, it was decided by NASA/MSFC and PSI to perform a laser absorption experiment on water vapor heated in a shock tube, where the gas conditions could be predicted very

reliably. The results of this experiment are presented in Chapter IV of this report; the details of the experiment are given in Appendix I.

The conclusions which can be drawn from the work performed during the present study are set forth in Chapter V.

II. SIMPLIFIED MODELS OF LASER-HEATED THRUSTERS

Parametric studies of laser-heated thrusters can be facilitied by the use of simplified models of the thrust chamber, which contain the essential physical elements of the thruster, but can be implemented in small, fast computer programs. Such models can be used to map out the operating characteristics of laser-heated thrusters, and describe approximately the regions of power, performance and wall heating in which they operate. These maps can then be used to indicate how engineering constraints, such as maximum wall heating rates, limit the performance of thrusters which can be built. This, in turn, provides information about what thrusters are likely to lead to useful rocket engines. The maps can also be helpful in designing experiments to prove the feasibility of laser-heated thrusters.

In order to provide this important information, PSI has developed simplified models for both the LSC wave and continuous modes of gas heating. These models are described in Appendices B and A, respectively. They relate the following thruster parameters:

F = Thrust
I_{sp} = Vacuum specific impulse
P_L = Incident laser power
$\bar{Q}_w$ = Average wall heating rate
R = Thrust chamber radius
L = Thrust chamber length

The models are implemented in simple, fast computer programs which use the thermodynamic state of the gas and some of the above parameters as inputs. They use conservation of mass, momentum and energy to calculate the other parameters. Included are estimates for convective and radiative wall heating. The thrust chamber geometry is modeled by a cylinder. In the continuous heating mode the wall heating is calculated by taking the gas temperature to be uniform at the highest temperature, which is the exit temperature. In the LSC wave heating mode, the losses from the LSC wave are also calculated

using the highest temperature in the wave, and those from the mixed gas region are found using the exit temperature. These are believed to be conservative estimates of the losses. On the other hand, the wall heating rate is the average over the chamber walls, and does not consider the possibility of hot spots along the chamber length.

The results of these models are expected to be accurate to better than an order of magnitude, and perhaps as good as a factor of two or three. With that understanding, they should be very useful in mapping out thruster parameters.

The models have been exercised to provide some examples of the results which can be obtained. Figure 1 shows a map for an H_2/H_2 buffer thruster absorbing 10.6 μm radiation in the LSC wave heating mode at a pressure of 3 atm. It covers the range of 5 kN to 0.5 kN thrust (1124 to 112 pounds), and I_{sp} of 1094, 1402 and 2007. The combination of laser intensity I_L and mass flow per unit area $\dot{m}_A$ is appropriate to a hydrogen LSC wave, as calculated in Ref. 3. The laser power required varies from 3 to 60 MW, and the average wall heating rate from 0.8 to 4 MW/m^2 (80 to 400 W/cm^2). If one recalls that the power in the exhaust is $P_G = F_g\ I_{sp}/2$, then it varies from 2.7 MW at 0.5 kN, 1100 s to 49 MW at 5 kN, 2000 s. Thus a large percent of the laser energy goes into the gas, making for an efficient absorption process. The heating rates appear to be in a range that can be handled with fairly conventional cooling methods. The wall heating is dominated by radiative rather than convective contributions.

A similar map for 30 atm is shown in Fig. 2, with the appropriate mass flow for the same laser intensity. It shows very similar results, with some reduction of heating rates at the same thrust and I_{sp}, primarily because the LSC wave is thinner at the higher pressure, because of enhanced laser energy absorption coefficients. The decrease in LSC wave size also changes the relative contributions of radiation and convection to the wall heating, making the convective contribution dominate.

Turning to the continuous heating mode, we have calculated some cases for a gas mixture of $H_2/H_2O/Cs$ = 0.945/0.05/0.005 absorbing 10.6 μm radiation. This mode does not have a relation between intensity and mass

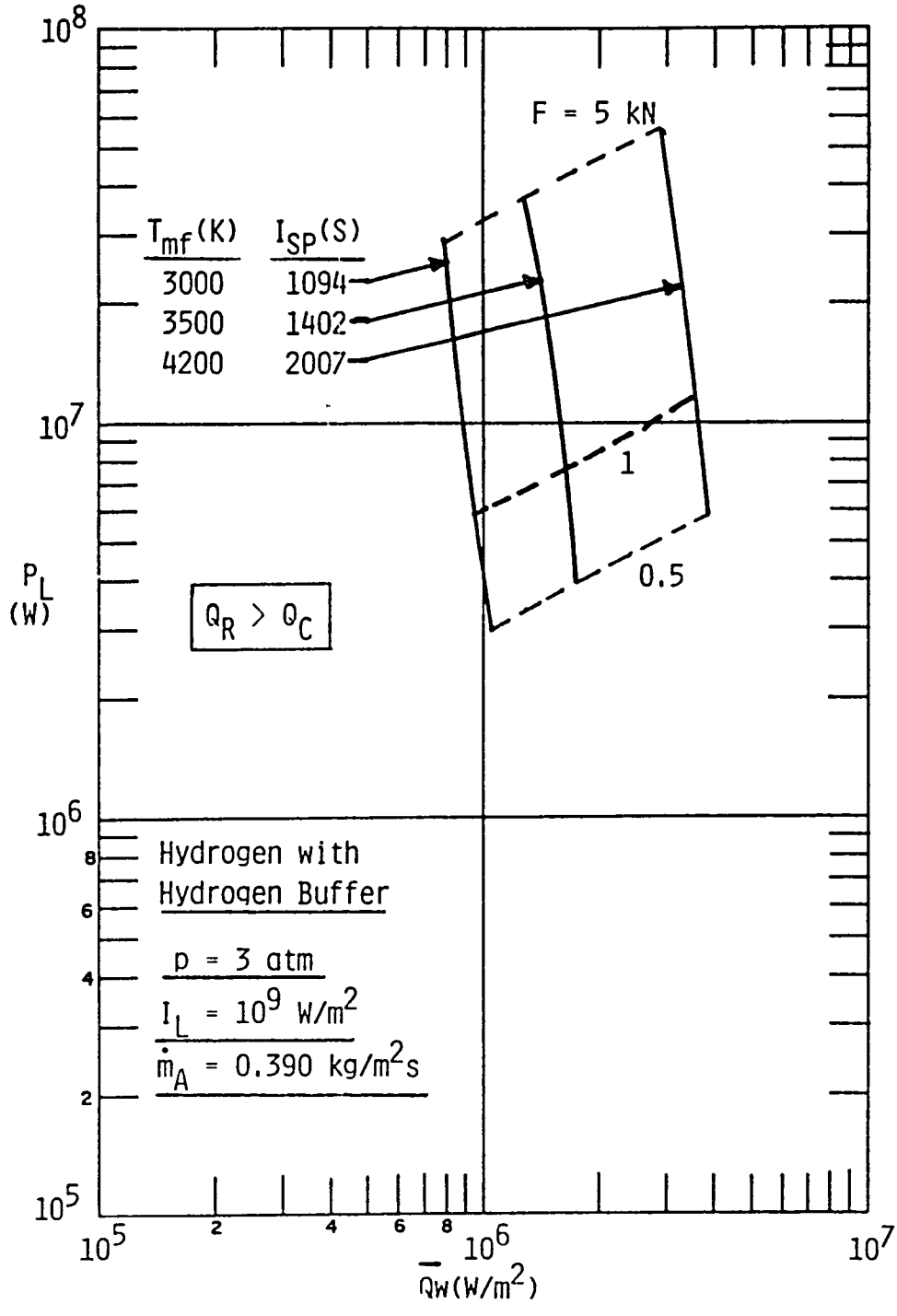

Figure 1 Laser power and average heating rate map for H_2/H_2 LSC wave heated thruster at 3 atm.

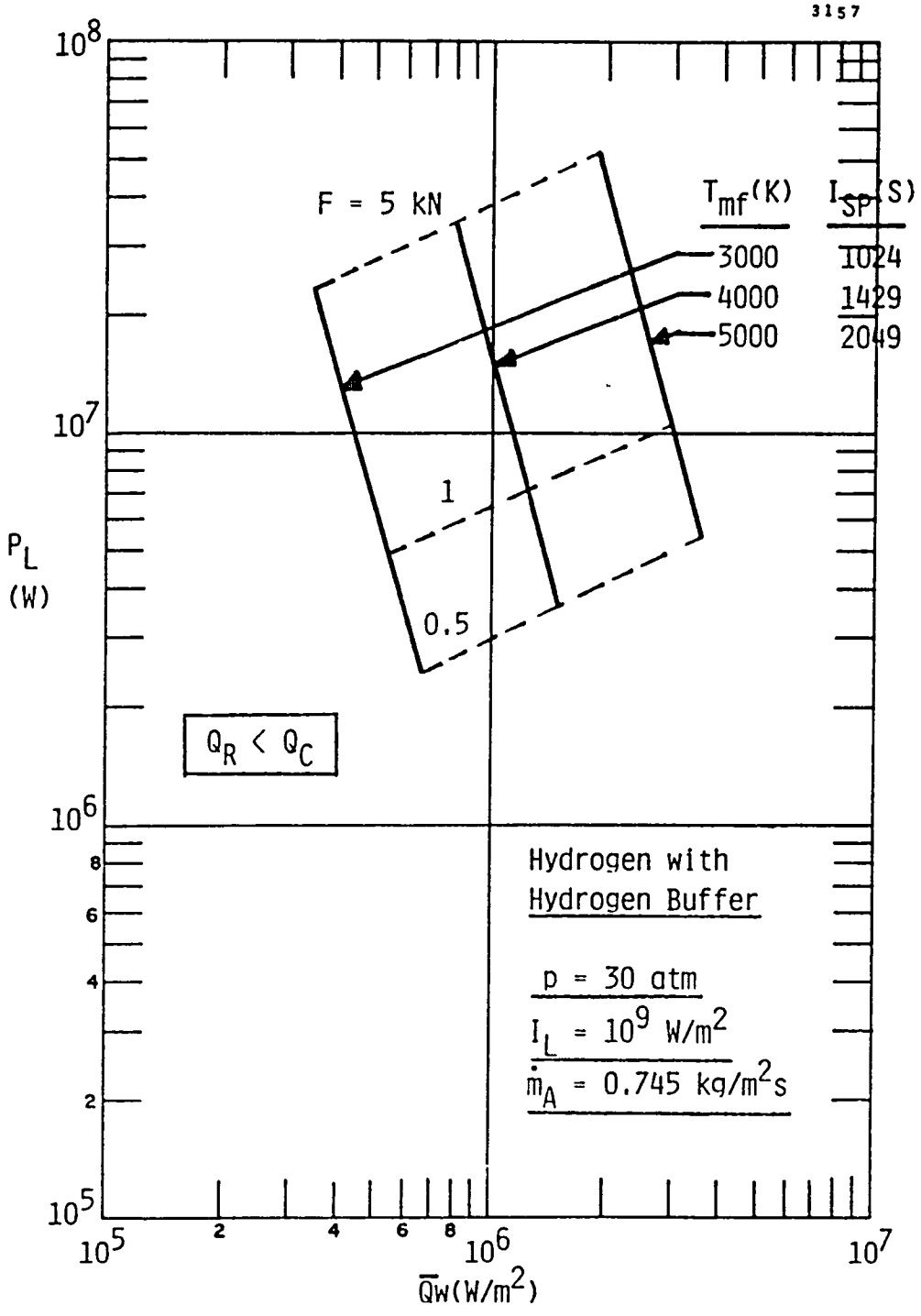

Figure 2 Laser power and average heating rate map for H_2/H_2 LSC wave heated thruster at 30 atm.

flow per unit area, so instead the radius of the thrust chamber is chosen. Figure 3 is for 3 atm, R = 0.1 m, for F = 0.1 to 5 kN and I_{sp} = 1042, 1390 and 2040 s. This map falls in a similar power and heating range to Figs. 1 and 2, varying from 0.8 to 50 MW power and 0.7 to 8 MW/m^2 heating rate. At the same thrust and specific impulse, this case has in fact somewhat higher heating rates at the higher thrusts than shown in Fig. 1. The heating here is mostly dominated by convection, except at very low values of thrust.

Raising the pressure level to 30 atm gives the map in Fig. 4, which is shifted almost a decade to the right compared to the previous maps, being centered on 10 MW/m^2 instead of 1 MW/m^2. However, these higher heating rates should be viewed with some caution. At 30 atm the length of these thrusters is very small, varying from 2.6 cm at 3500 K to 0.6 cm at 6000 K. These small lengths are caused by the large absorption coefficients at 30 atm, since the length is taken as the inverse of the absorption coefficient. They in turn, lead to average high convective heating, which is inversely proportional to the square root of the length. Longer thrust chambers might have smaller average heating, although the radiative component of the heating will also change. The laser power levels of these thrusters are very much the same as those at 3 atm in Fig. 3. The heating is a small fraction of the laser power, so considerable changes in heating do not alter the power level much.

These calculations are meant to illustrate the kind of results which can be obtained rapidly with the simplified thrust chamber models. They are by no means a parametric study. They do show what values of laser power are needed, and what average heating rates have to be handled for thrusters which might be of operational size. The powers are not much larger than the exhaust gas power, and the heating rates seem within a range which are dealt with in present rocket practice.

Another use for the simplified models is in the design of small-scale experiments. As an example of this sort of calculation, we have considered thrusters which can be designed with a 30 kW laser beam. Again, calculations have been made for both heating modes at 3 and 30 atm pressure.

Table 1 shows the results for the LSC wave heated mode at 3 atm, with laser intensity of 3 x 10^9 W/m^2, and I_{sp} = 1094, 1833 and 2454 s. The thrust

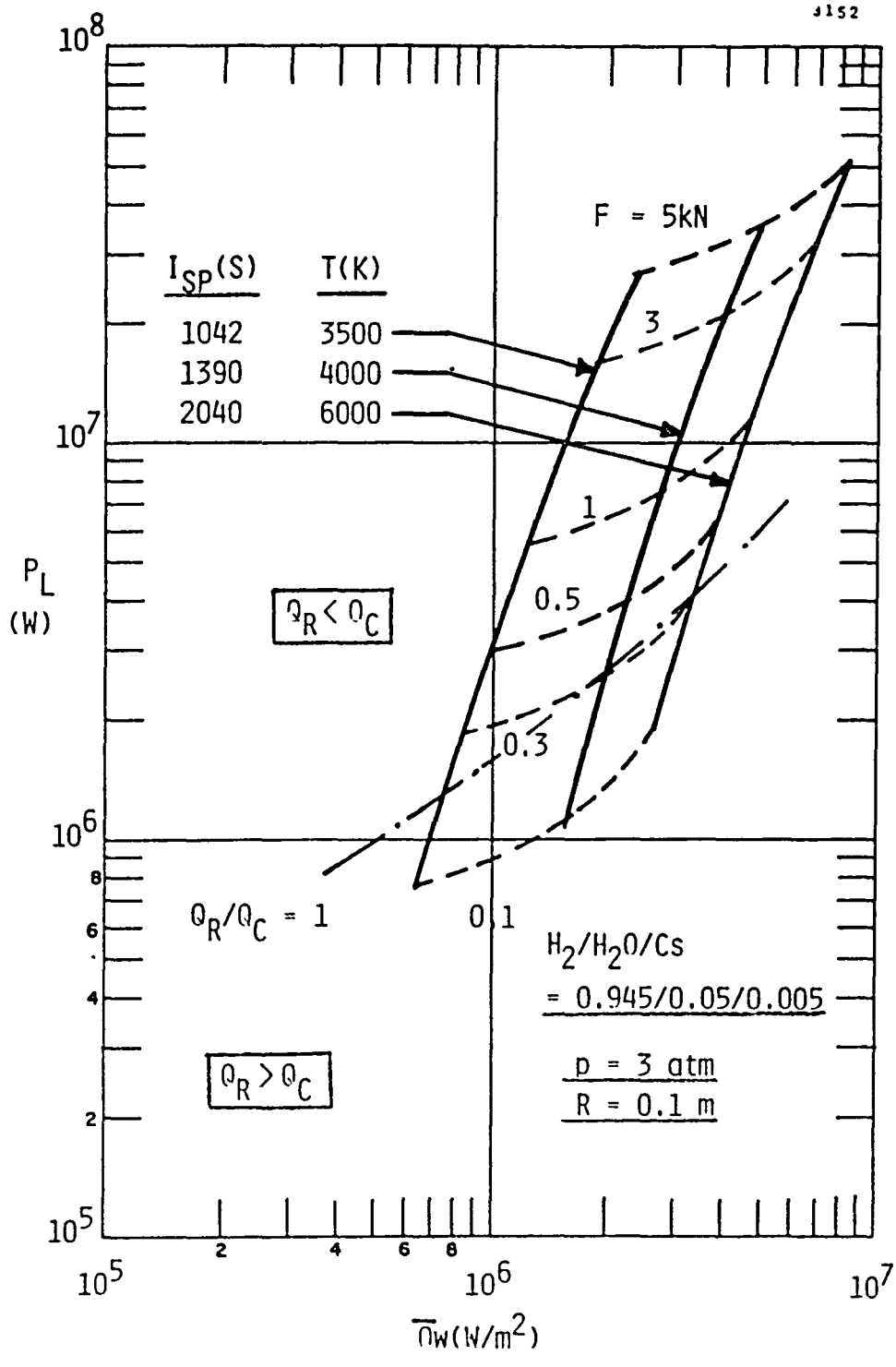

Figure 3 Laser power and average heating rate map for $H_2/H_2O/Cs$ continuously heated thruster at 3 atm.

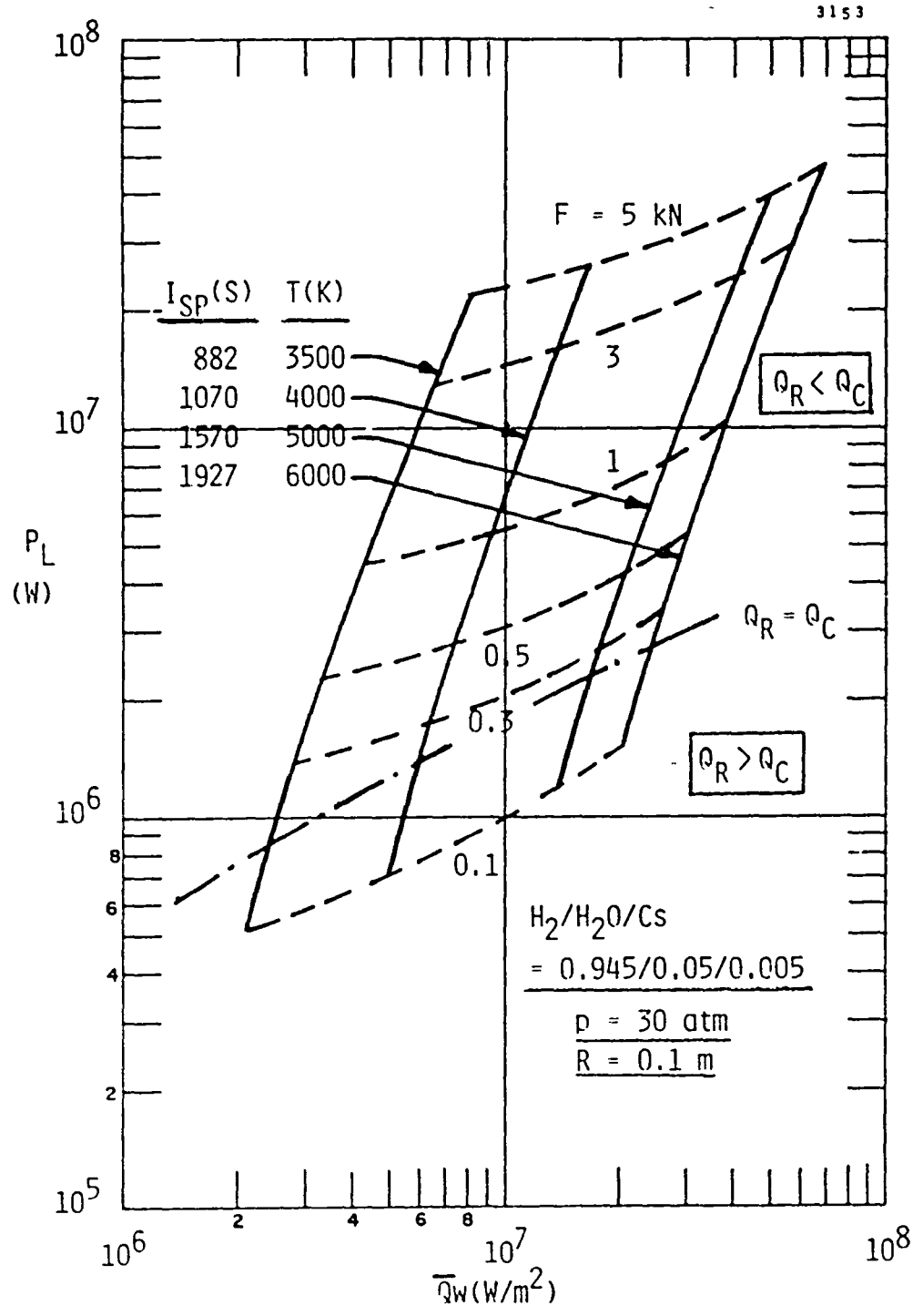

Figure 4 Laser power and average heating rate map for $H_2/H_2O/Cs$ continuously heated thruster at 30 atm.

TABLE 1

LOW LASER POWER, LSCW-HEATED, BUFFERED HYDROGEN

$p = 3$ atm, $I_L \sim 3 \times 10^9$ W/m^2, $\dot{m}_A = 0.381$ kg/m^2-s

T_{mf}(K)	I_{sp}(s)	F(N)	P_{I_L}(W)	$\bar{Q}_w$(W/m^2)	R_m(m)	R_h(m)	P_W/P_G	Q_R/Q_C
3000	1094	3.8	30.1×10^3	2.45×10^6	1.71×10^{-2}	1.73×10^{-3}	0.62	1.49
4000	1833	2.0	30.3×10^3	7.62×10^6	9.64×10^{-3}	1.83×10^{-3}	0.73	1.07
5000	2454	1.4	30.1×10^3	1.38×10^7	6.97×10^{-3}	1.83×10^{-3}	0.82	0.95

levels are a few newtons, and the average wall heating rates are 2.45 to 13.8 MW/m^2 (245 to 1380 W/cm^2). Also shown in Table 1 are the thruster radius R_m, the laser spot size R_h, the ratio of power going into the wall to that in the gas at the thrust chamber exit P_w/P_G and the ratio of radiative to convective wall heating Q_R/Q_C. It can be seen that these small size thrusters are not as efficient in putting power into the gas as are the large ones previously considered, and they receive about equal amounts of radiative and convective wall heating. But the size and heating rates are in the range of possible experimental hardware.

A similar calculation for 30 atm is shown in Table 2, for the same 30 kW, but with the lower intensity LSC wave that is permitted at 30 atm, namely $10^9 W/m^2$. The over-all radius is about the same, but the spot size is larger because the intensity is lower. The power efficiency P_W/P_G is also better, and the wall heating is convection dominated, because the shorter lengths associated with the higher absorption coefficients at 30 atm result in a smaller radiating volume.

The small-scale continuous heating mode is represented by the results shown in Figs. 5 and 6. They are for the same gas mixture as before, $H_2/H_2O/Cs$ = 0.945/0.05/0.005, and for a thruster radius of 2 cm. Figure 5 presents the 3 atm case down to F = 1N. The 30 kW power level will produce about 2N at 1042 s or 1N at 1389 s. The corresponding average wall heating rates are 0.3 and 0.5 MW/m^2, which are quite low, although the thrust chambers are between 37 and 55 cm long at these low temperatures. At 30 atm, Fig. 6 shows that 30 kW will produce 5N at 882 s for 1.7 MW/m^2, or 2N at 1570 s for 9 MW/m^2. At this pressure, the thrust chambers are 2.6 and 0.6 cm long, respectively. The results indicate the possibility of performing small-scale, continuous heating thruster experiments within reasonable engineering constraints.

This small group of examples shows the usefulness of the simplified thruster models as engineering tools for defining both full-size and small-scale thruster parameters. Furthermore, the calculations show promise that laser heated thrusters with measurable thrust can be tested on a small scale, and that large-scale thrusters can be made with useful values of thrust and specific impulses over 1000 s.

TABLE 2

LOW LASER POWER, LSCW-HEATED BUFFERED HYDROGEN

$p = 30$ atm, $I_L \sim 10^9$ W/m^2, $\dot{m}_A = 0.503$ kg/m^2-s

T_{mf}(K)	I_{sp}(s)	Th(N)	P_L(W)	$\bar{Q}_w$(W/m^2)	R_m(m)	R_h(m)	P_W/P_G	Q_R/Q_C
3000	1024	4.8	30.1×10^3	2.18×10^6	1.73×10^{-2}	3.09×10^{-3}	0.38	0.76
4000	1429	3.0	29.3×10^3	5.35×10^6	1.16×10^{-2}	3.04×10^{-3}	0.46	0.61
5000	2049	2.0	30.6×10^3	1.35×10^7	7.94×10^{-3}	3.1×10^{-3}	0.56	0.49

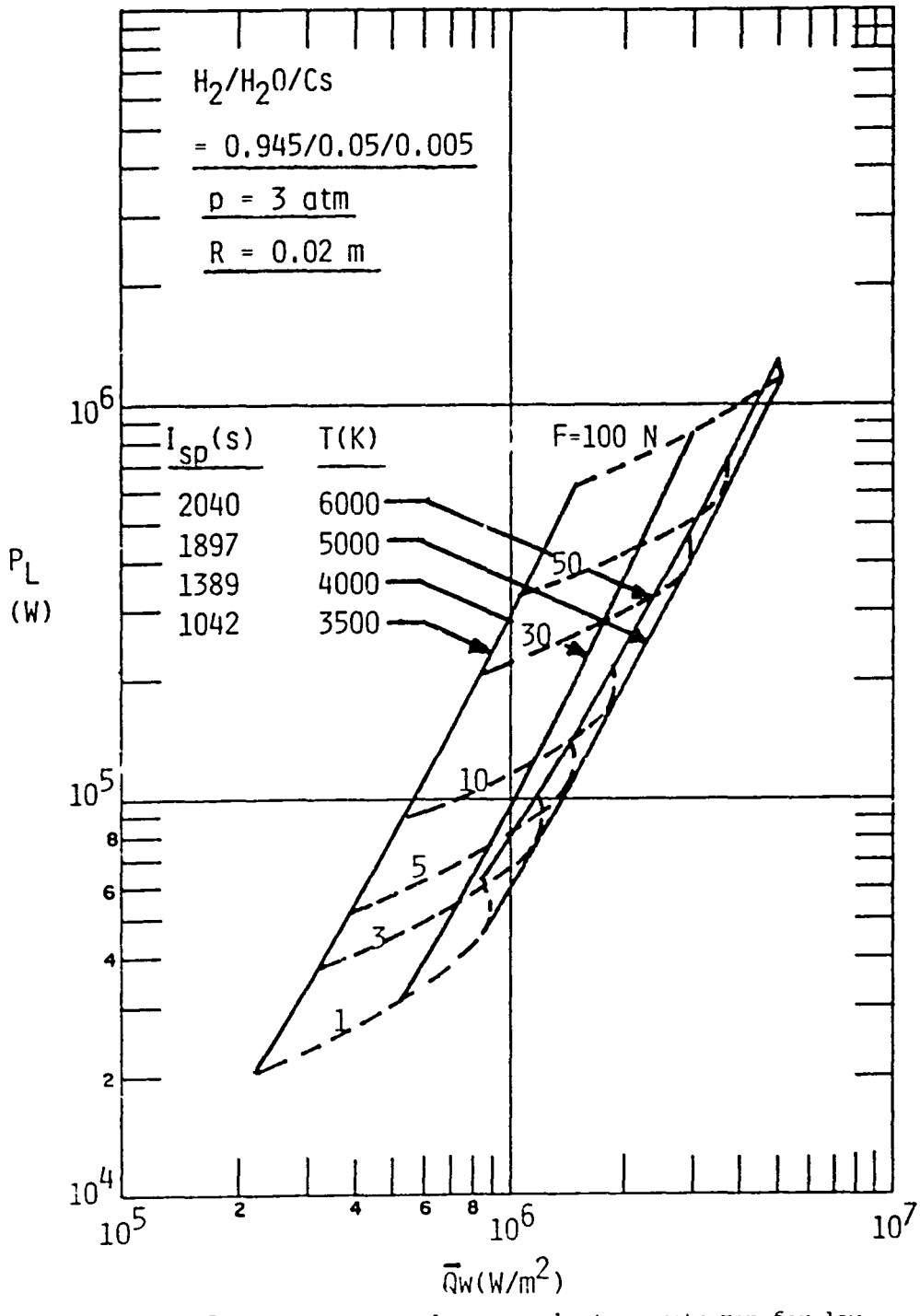

Figure 5 Laser power and average heating rate map for low power $H_2/H_2O/Cs$ continuously heated thruster at 3 atm.

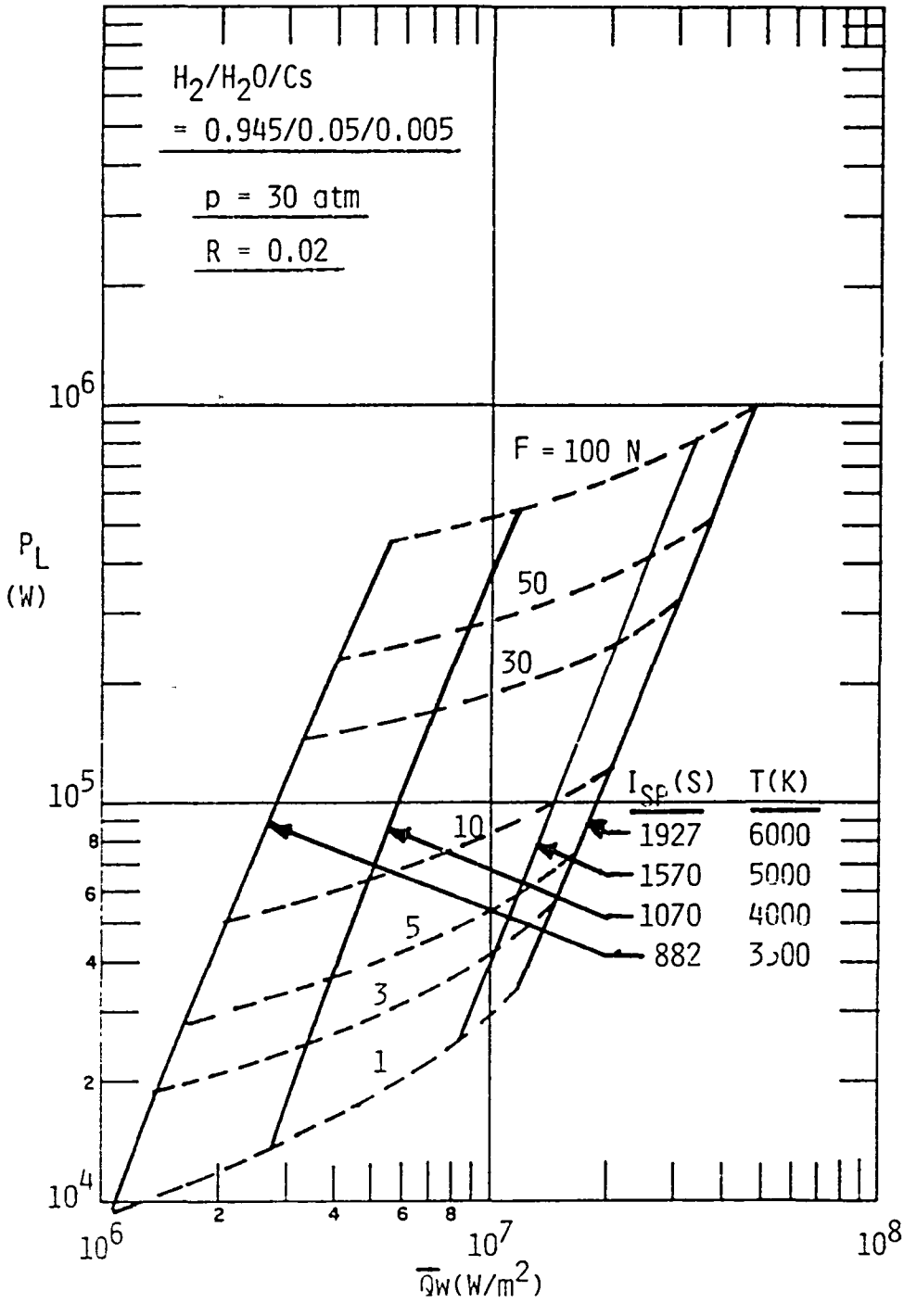

Figure 6 Laser power and average heating rate map for low power $H_2/H_2O/Cs$ continuously heated thruster at 30 atm.

III. THRUST CHAMBER DESIGN PROGRAMS

One of the objectives of the present study was to develop computer programs which could be used for the design of laser heated thrust chambers. Because of the presence of the LSC wave, the program for the LSC wave heating mode differs from that for the continuous heating mode, so that two programs are needed. In addition, a program for calculating LSC wave structure is needed, since the output of that program is used as the input for the thrust chamber design program in the LSC wave heating mode.

The thrust chamber design programs solve the axisymmetric flow of a gas in chemical equilibrium, which is undergoing laser heating, radiation energy loss and radial transport, and conductive radial transport. The equations of motion are written using the boundary layer approximation that the axial component of conductive energy and momentum transport can be ignored compared to the radial component. The equations use the stream function as the independent variable in place of the radius. Only the initial radius of the thrust chamber is given at x=0. The shape of the chamber, $R_w(x)$, is determined as a result of the calculation, and is mainly influenced by the axial pressure gradient, which is input as a function of axial distance.

In addition to the chamber radius $R_w(x)$, the programs calculate the local heating rates at the walls, the velocity, temperature and laser intensity profiles, and the total energy transferred to the walls up to any axial station.

The equations for the continuous heating program (called LHTE) are presented in Appendices E and F. The equations for the LSC wave heating program (called CLHTE) are the same as those for LHTE, but the initial conditions at x=0 are different. These initial conditions are obtained from a solution of the LSC wave which stands at the entrance of the thrust chamber.

The program which solves for the LSC wave structure in hydrogen, or a mixture of cesium and hydrogen, is called LSCWCS. The equations which describe it are presented in Appendix G. They are one-dimensional flow equations for a constant area flow of a laser heated gas in chemical equilibrium, with radiation loss and axial transport, and conductive axial transport. They include laser beam convergence effects and estimates for radial energy loss.

The method of coupling the output of the LSC wave program LSCWCS to the thrust chamber code CLHTE is described in Appendix H. The gas emanating from the LSC wave at some chosen axial station in the wave (currently the maximum temperature point) is used as the initial state for the central core of the thrust chamber. An annular region around this core is taken to be a buffer region of gas which is not heated by the laser. The initial temperature of this buffer gas is higher than the inlet temperature of the gas entering the LSC wave, because the radial energy losses from the LSC wave are used to heat up the buffer gas as it flows past the LSC wave. This slightly heated buffer gas is the initial state for the outer annulus of the thrust chamber, at the same axial station as the LSC wave heated gas. As the two gas streams flow through the thrust chamber they mix to some temperature intermediate between the buffer gas inlet temperature and the high temperature of the laser heated gas.

A few sample calculations have been made with these codes, and some results will be presented. First consider the LSC wave heating mode, using hydrogen and a hydrogen buffer, for 3 atm, with a laser intensity of 10^5 W/cm^2. The LSCWCS code yields a gas at about 17,400 K, and a residual laser intensity of about 2×10^4 W/cm^2, so 80% of the laser energy is absorbed in the LSC wave up to the peak temperature station. The laser spot radius is 3.99 cm, and the initial chamber radius is 8.2 cm, so the buffer gas is contained between 3.99 and 8.2 cm. The initial buffer gas temperature is calculated to be 433 K, representing a 133 K temperature rise from the inlet temperature of 300 K, caused by heating from the edges of the LSC wave.

The CLHTE program was run for 12.26 cm in the axial direction. Radial profiles of the laser intensity are presented in Fig. 7 at the three axial stations x = 0, 0.305 and 12.264 cm. The initial profile shows the initial intensity coming through the LSC wave up to a radius of 4 cm, and no laser in the buffer gas region. At 0.305 cm, the intensity has dropped to about 5700 W/cm^2 in the core, as further absorption takes place. (The more gradual transition to zero intensity at this station is an artifact of the numerical solution.) By 12.264 cm, the laser intensity has vanished, all the energy having been absorbed.

The corresponding temperature profiles are given in Fig. 8. The initial profile shows the discontinuous profile from 17,400 K in the core to 433 K in the buffer region. At 0.305 cm, a slight further heating of the core has occurred, from the residual laser intensity at the back of the LSC wave, and the core temperature has risen to 19,000 K, with very little diffusion of heat to the buffer gas as yet. By 12.264 cm cooling and diffusion have begun to show their effects, and the temperature profile has begun to smooth out, with its maximum down to 15,500 K.

The axial velocity profiles are shown in Fig. 9. They show little change between 0 and 3 cm, both giving nearly discontinuous profiles from the 30,000 cm/s emanating from the LSC wave to the 235 cm/s at which the slightly heated buffer gas flows. (The inlet gas is flowing at 162 cm/s.) By 12.264 cm the velocity profile has accelerated in the center and diffused outward, with a maximum velocity of 36,000 cm/s.

A plot of the wall radius vs axial distance is shown in Fig. 10. Recall that this is calculated from the input pressure gradient distribution, which was taken as constant for this case at $dp/dx = -2.3 \times 10^{-5}$ atm/cm, resulting in a negligible change in pressure up to 12.264 cm. The wall profile shows a decrease from 8.2 cm at the inlet to 5.2 cm at 12 cm, an area decrease from 211 to 85 cm^2, or a factor of 2.5. The profile looks quite smooth, except for a slight bump near 0.8 cm.

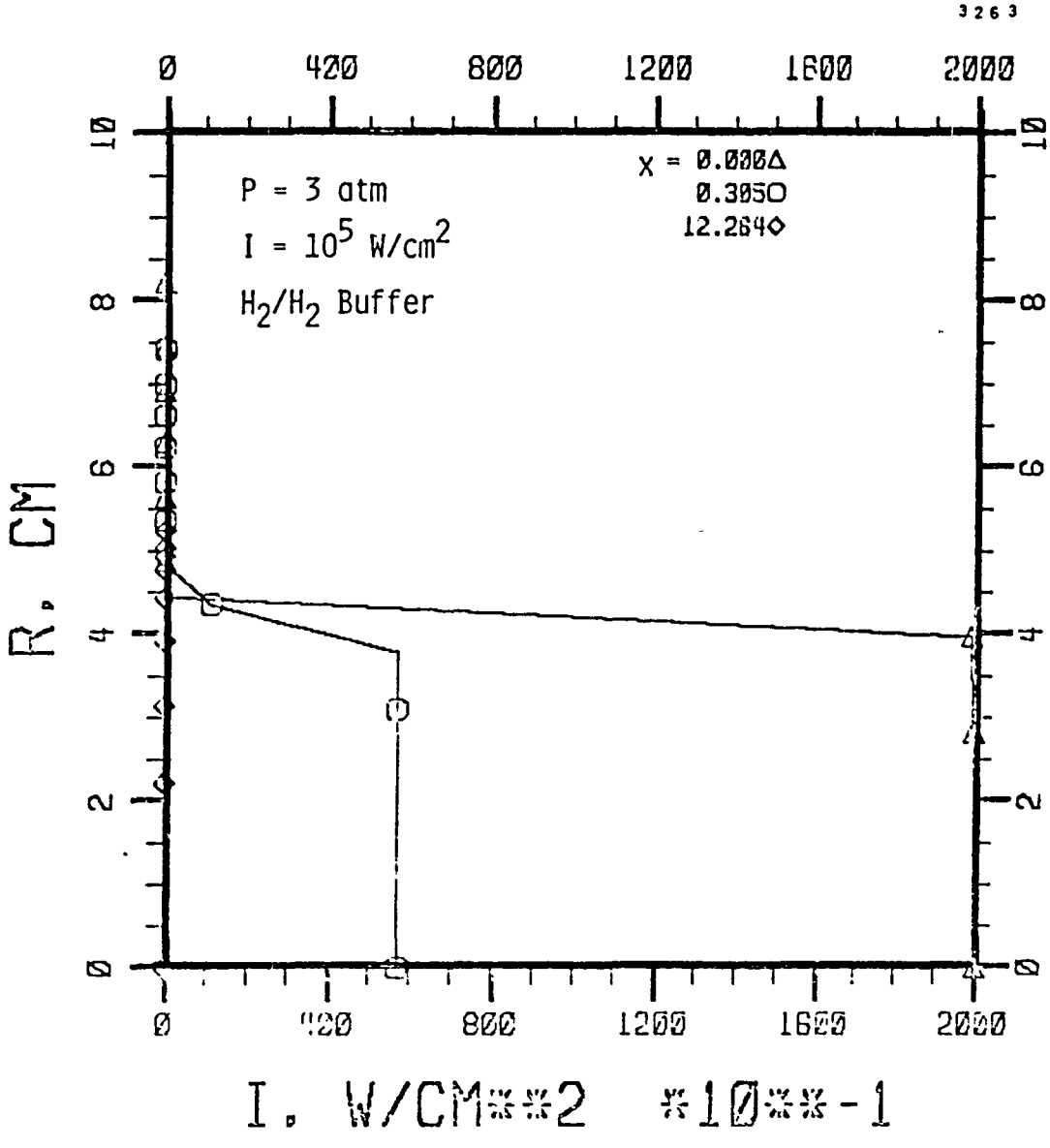

Figure 7 Radial profiles of laser intensity for LSC wave heated thruster from program CLHTE.

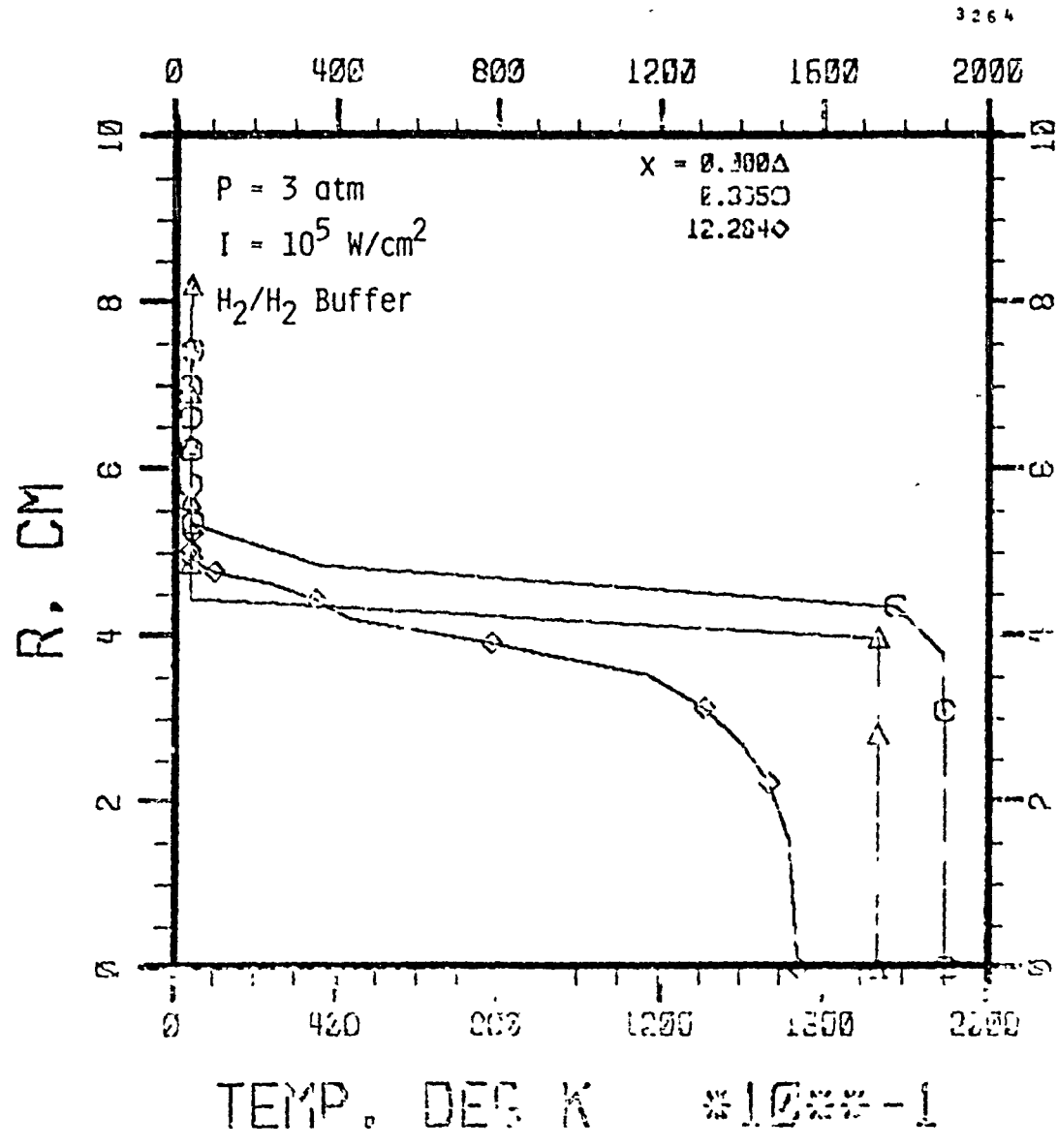

Figure 8 Radial profiles of temperature for LSC wave heated thruster from program CLMTE.

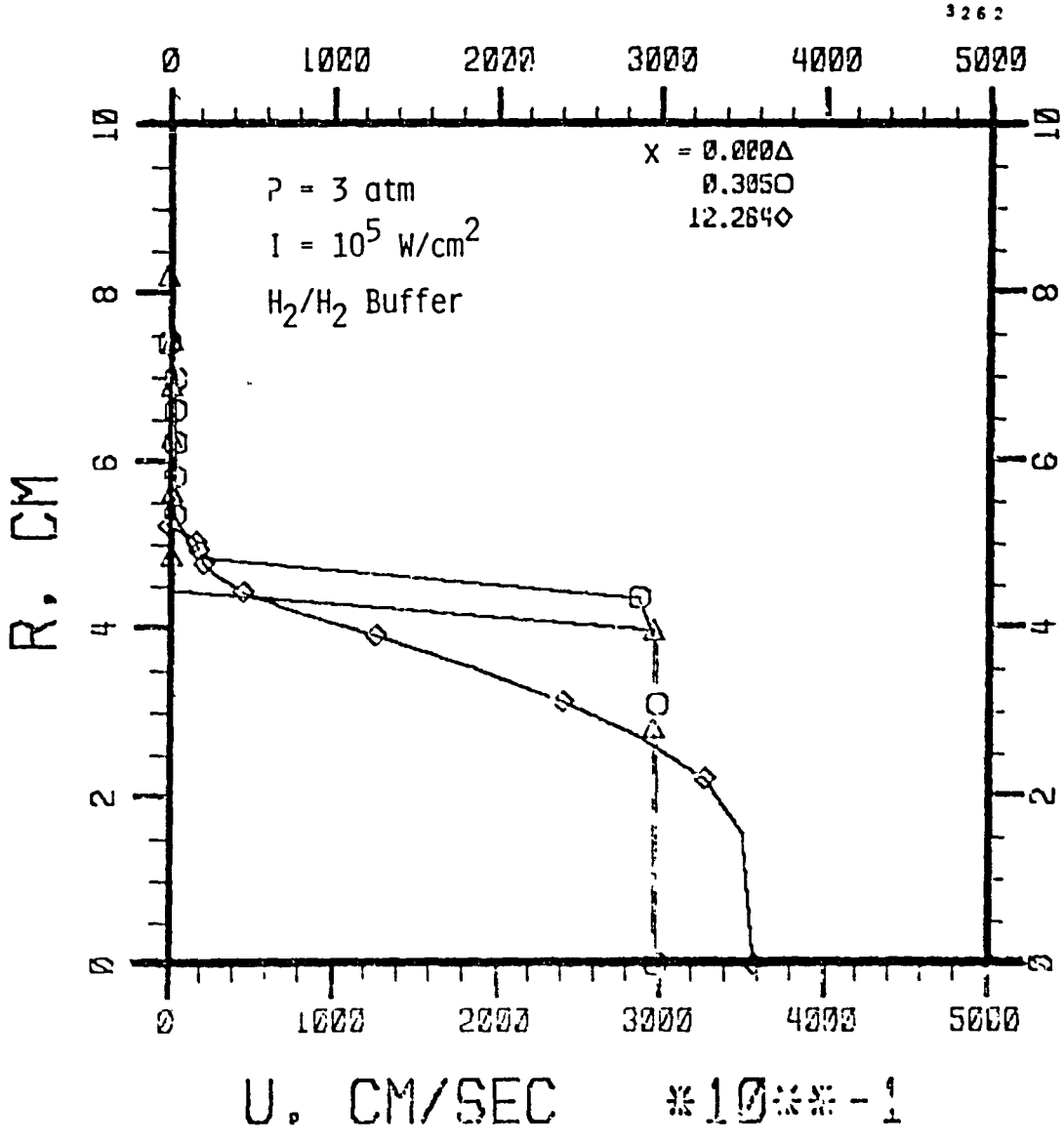

Figure 9 Radial profiles of axial velocity for ISC wave heated thruster from program CLHTE.

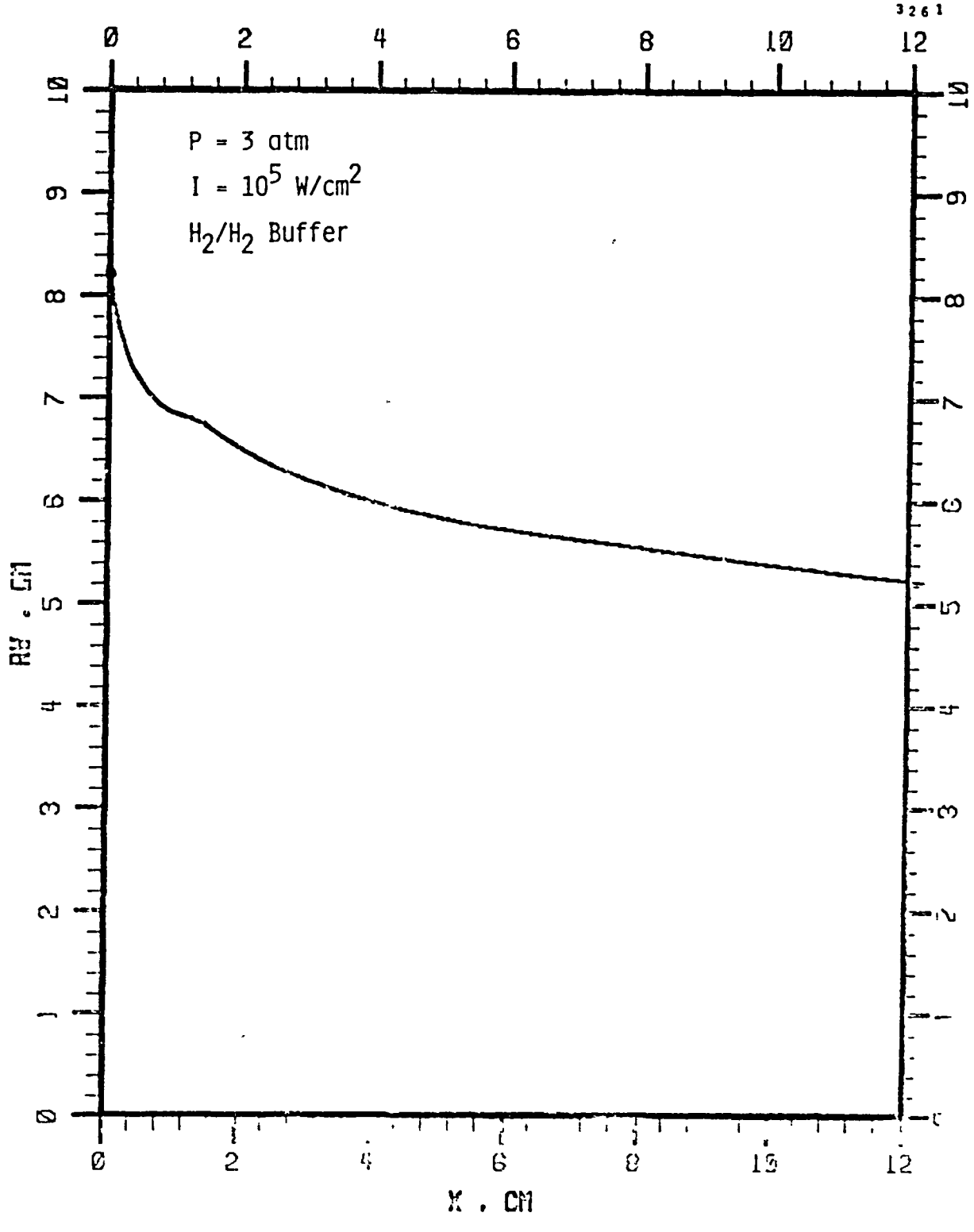

Figure 10 Wall radius distribution for LSC wave heated thruster from program CLHTE.

The power in the gas as a function of axial distance is shown in Fig. 11. It starts at the value emanating from the LSC wave of 3.46 MW, rises slightly to 4.3 MW at x = 0.6 cm while the rest of the laser energy is being absorbed, and then decays slowly as it loses energy to the walls. It reaches 2.59 MW at 12.264 cm. The laser power input to the LSC wave in a spot of radius 3.99 cm with an intensity of 10^5 W/cm^2 was 5 MW, so about 90% came through the LSC wave in the gas or in the residual laser beam, and about half is still in the gas at the last station. However, for this sample case, the gas is not yet accelerated to the throat, since the sound speed at 3 atm, 15,500 K for hydrogen is about 1.4×10^6 cm/s, while the maximum gas speed is only 3.6×10^4 cm/s. To make this case more efficient, it would be necessary to accelerate the gas much faster, which would require a larger input pressure gradient.

Finally, the distribution of wall heating rate is shown in Fig. 12. The peak value is about 6×10^3 W/cm^2 at 1 cm, with a slow decay to 2×10^3 W/cm^2 at the last station. This corresponds to about 1.98 MW put into the walls. The energy balance has then 4.57 MW in the gas or walls at the last station, while the power emanating from the LSC wave was 4.46 MW. The slight discrepancy of 2.5% represents the numerical inaccuracy in doing the various axial and radial integrals to find the integrated power contributions.

The results of an example using the continuous heating program LHTE are shown in Figs. 13-18. This case is for a mixture of $H_2/H_2O/Cs$ = 0.945/0.05 0.005 at 30 atm entering at 1000 K, with a laser power of 1 MW incident on a thrust chamber whose initial radius is 12.39 cm. The shape of the incoming beam is related to the J_1 Bessel function, as described in Eqs. (5-12) and (5-13) of Ref. 4, with a peak intensity at the center line of 3100 W/cm^2. This calculation has been run to 20 cm. The figures have profiles at 0, 8.971, 10.231 and 16.482 cm.

Figure 13 gives the laser profiles. The initial shape is shown at x = 0, and the subsequent profiles show the laser energy being absorbed well in the center of the chamber, but not as well near the walls, where the temperature is cooler because the walls are held at a fixed temperature of 1000 K. Finally, at 16.482 cm the laser energy is almost completely absorbed, even near the wall.

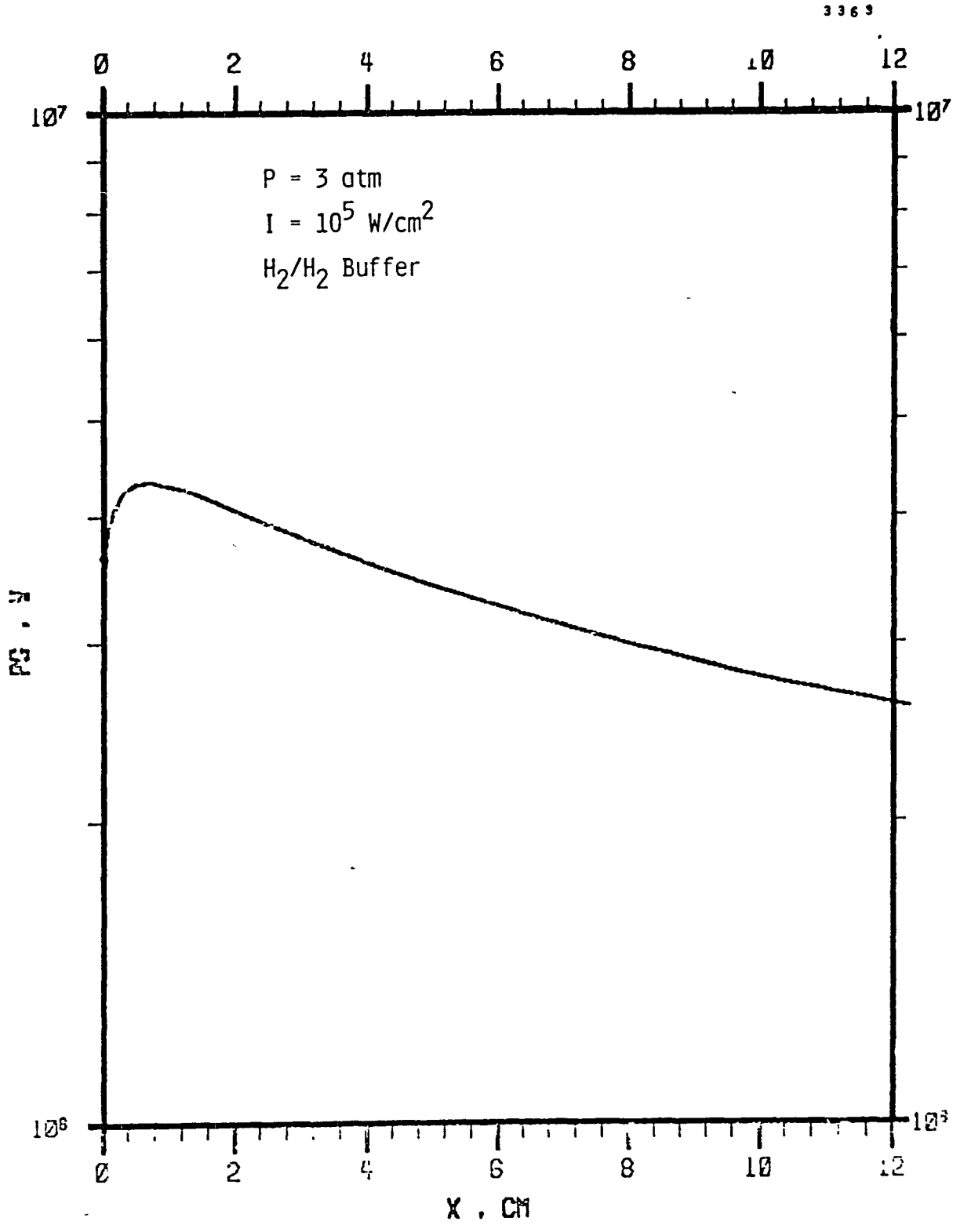

Figure 11 Distribution of power flowing in the gas for LSC wave heated thruster from program CLHTE.

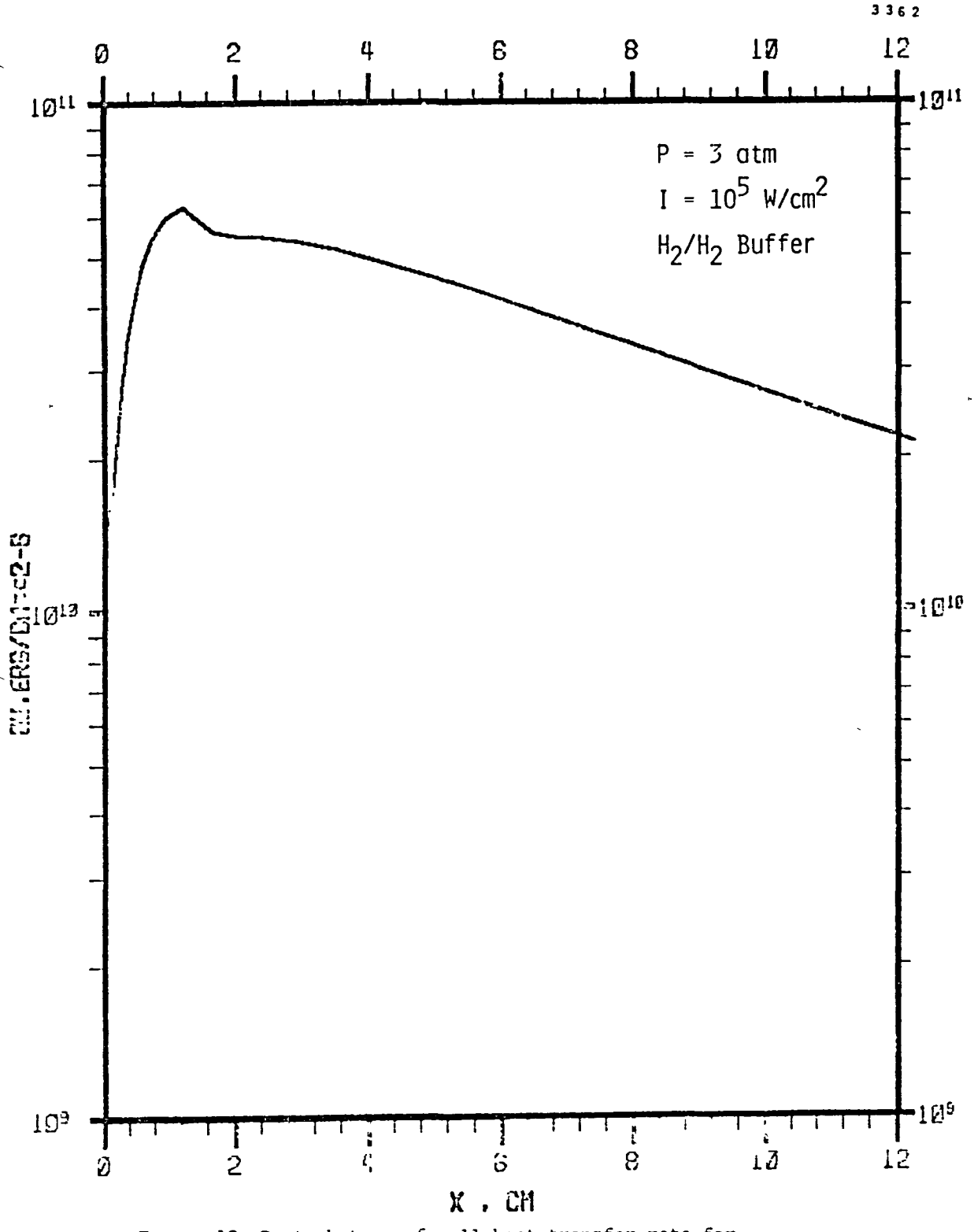

Figure 12 Distribution of wall heat transfer rate for LSC wave thruster from program CLHTE.

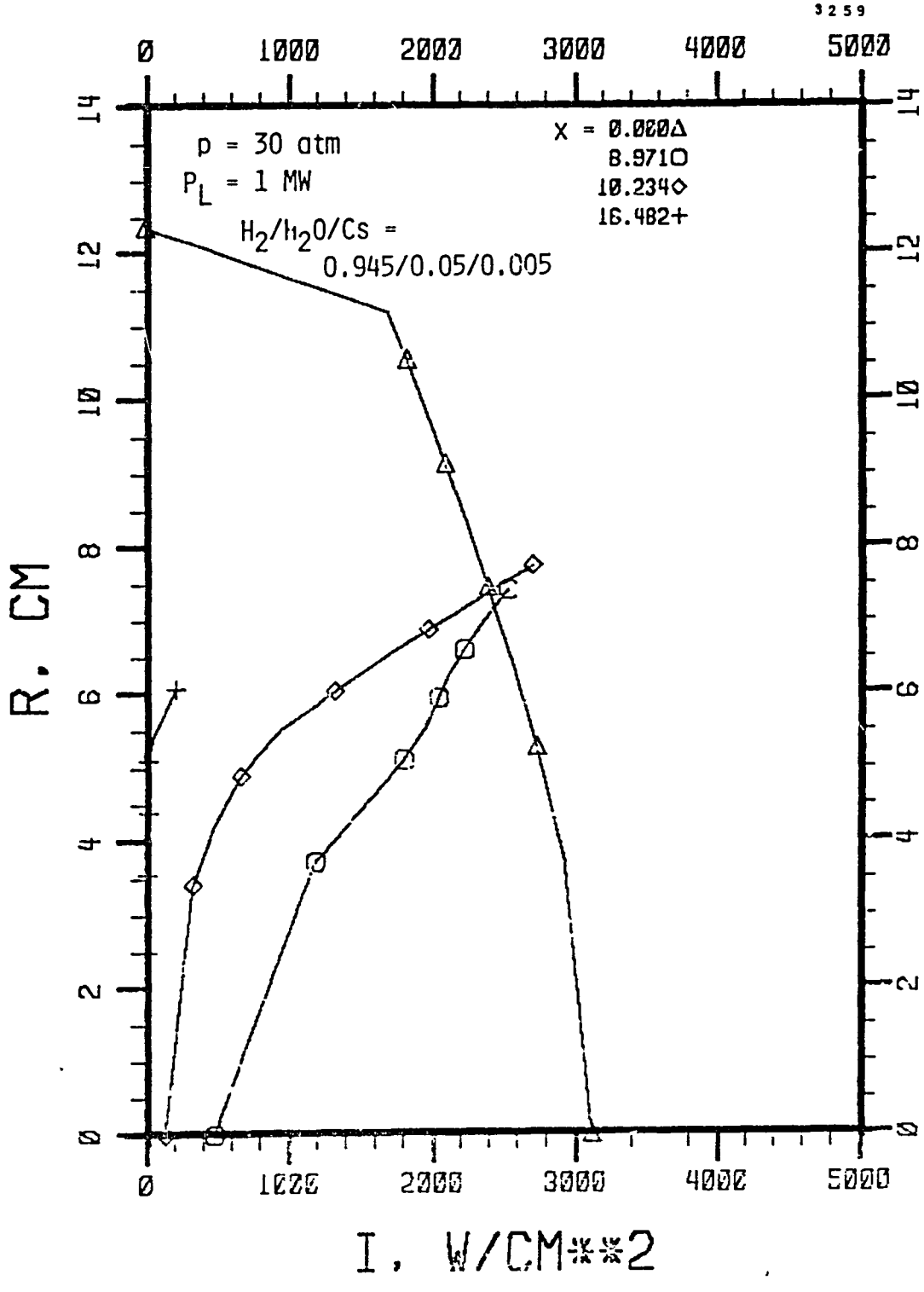

Figure 13 Radial profiles of laser intensity for continuously heated thruster from program LHTE.

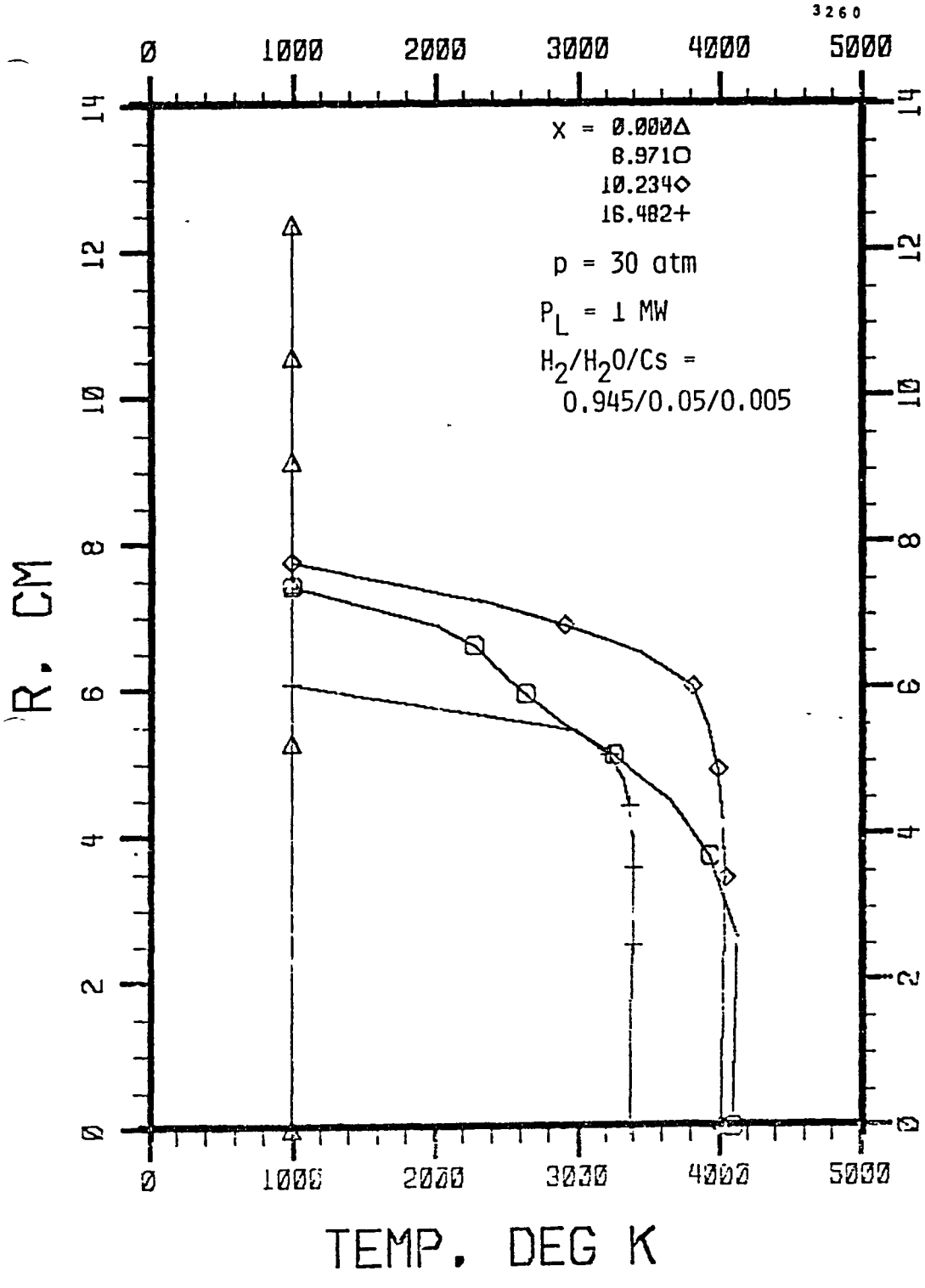

Figure 14 Radial profiles of temperature for continuously heated thruster from program LHTE.

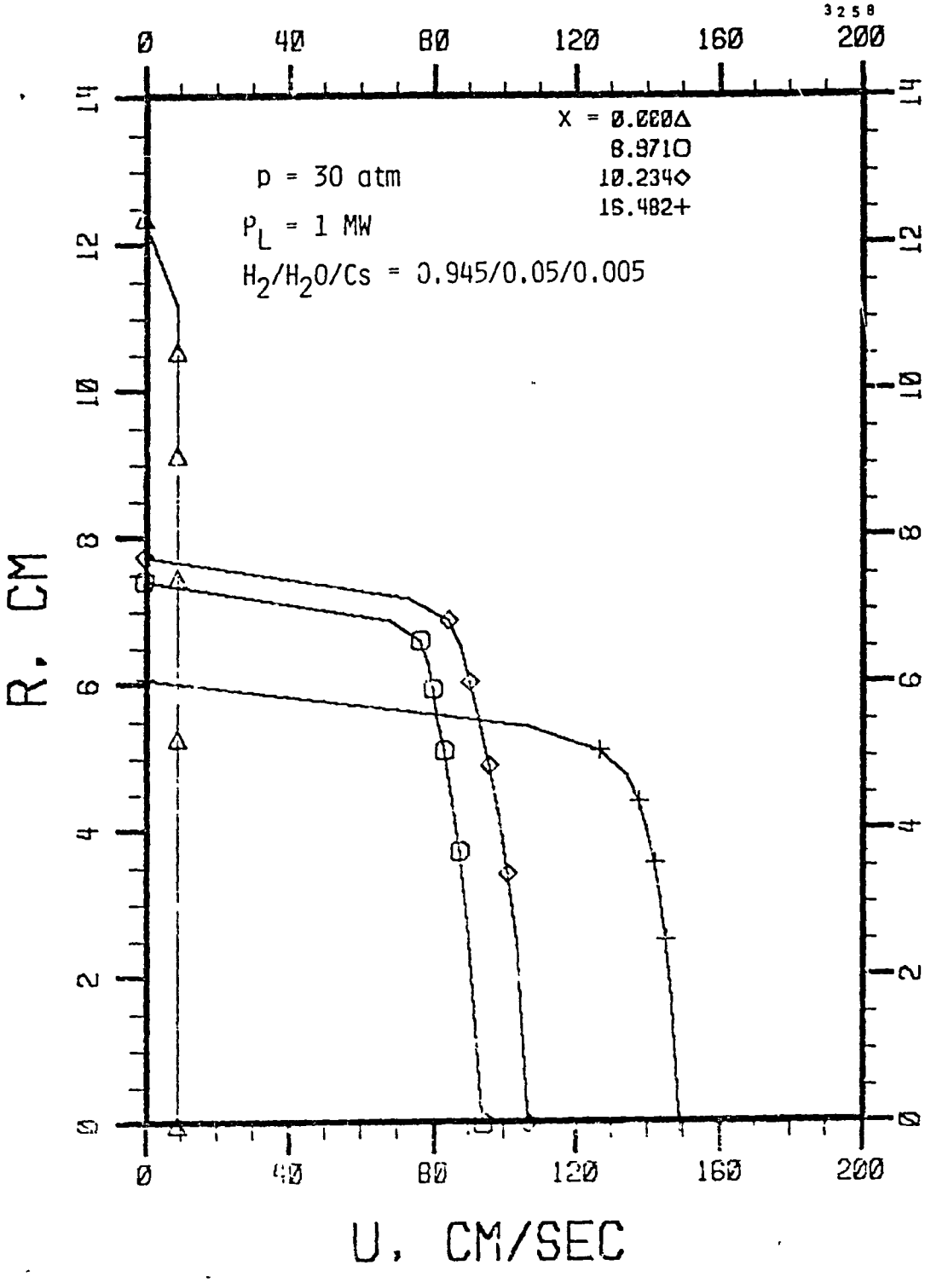

Figure 15 Radial profiles of axial velocity for continuously heated thruster from program LHTE.

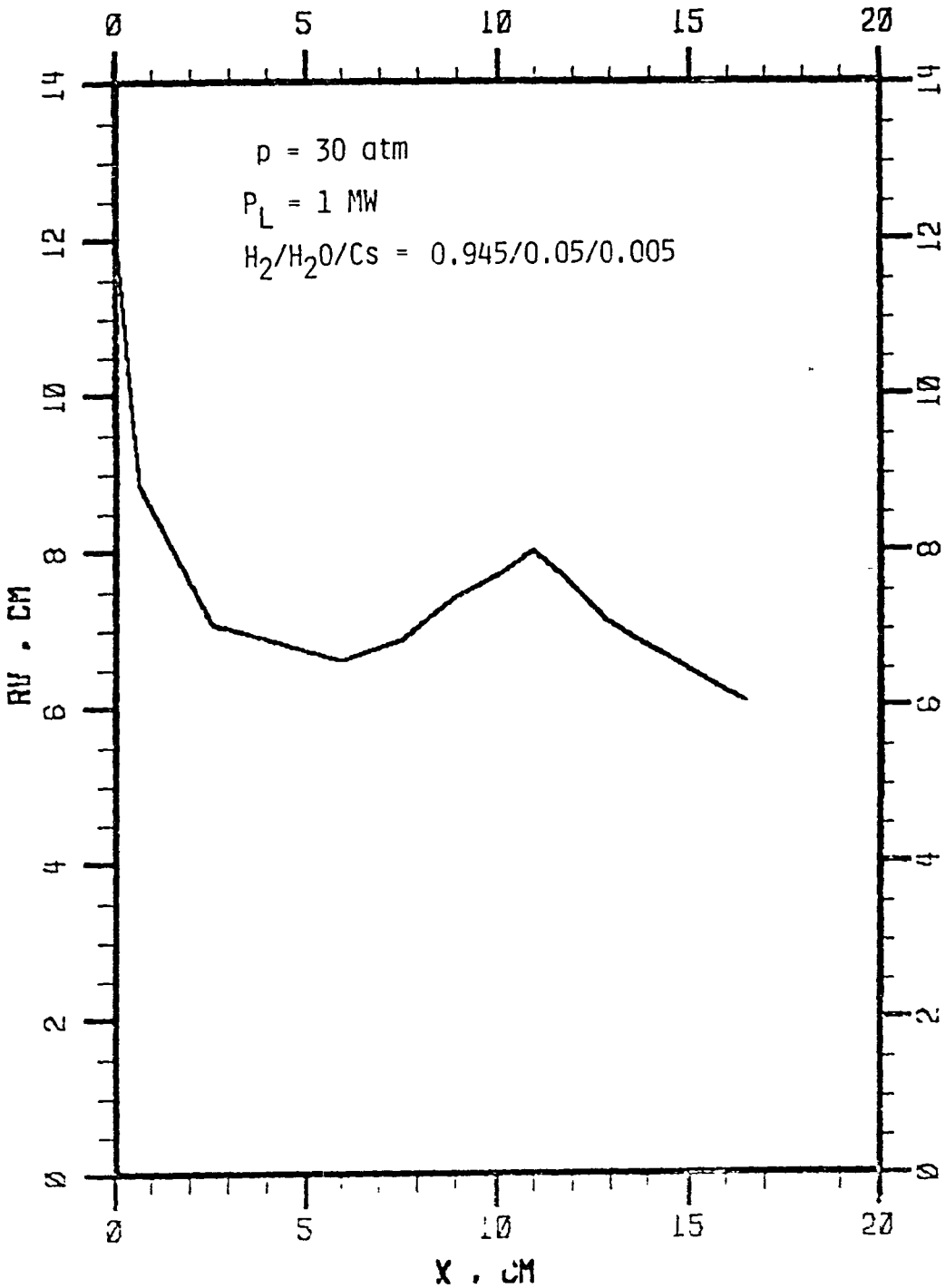

Figure 16 Wall radius distribution for continuously heated thruster from program LHTE.

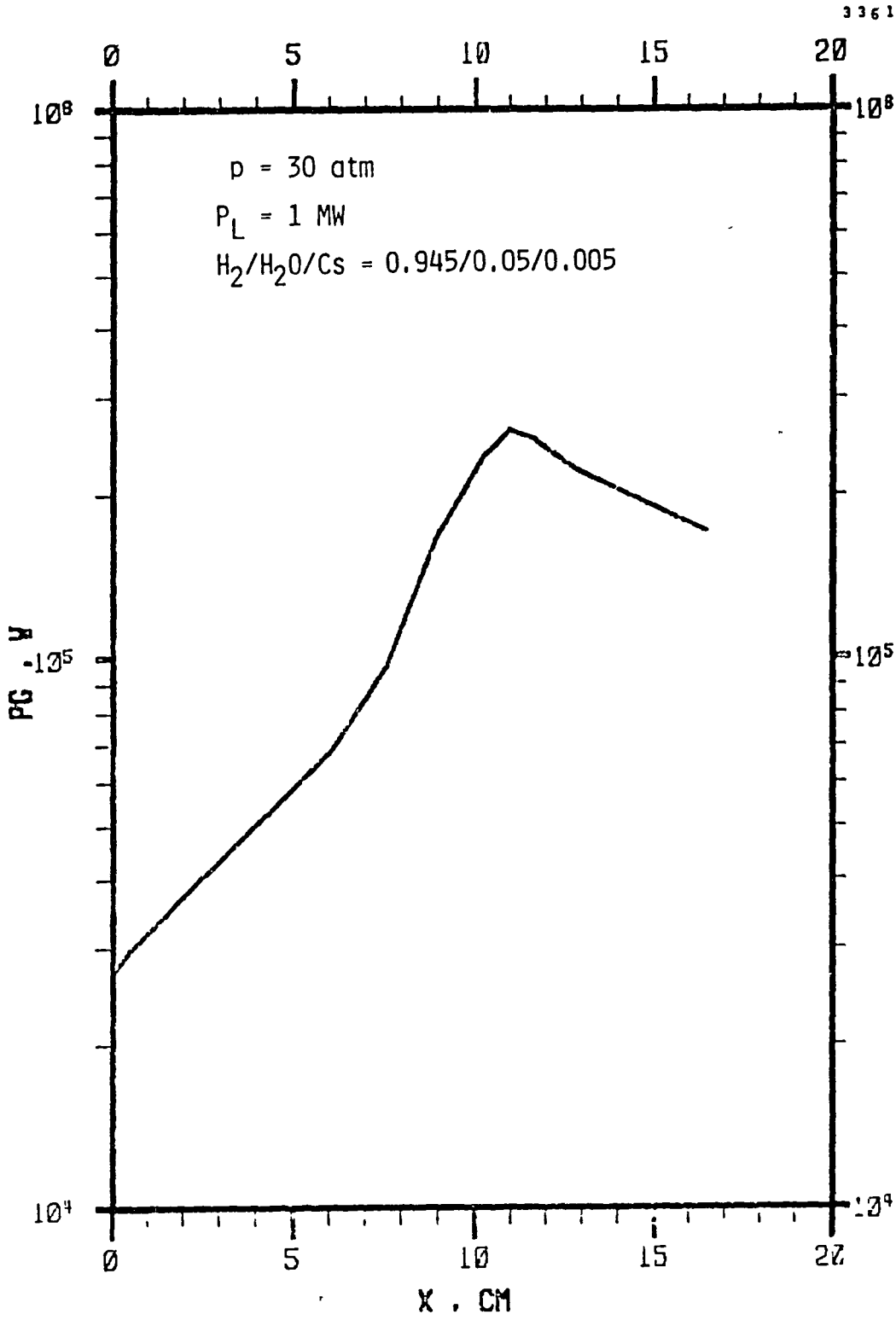

Figure 17 Distribution of power flowing in the gas for continuously heated thruster from program LHTE.

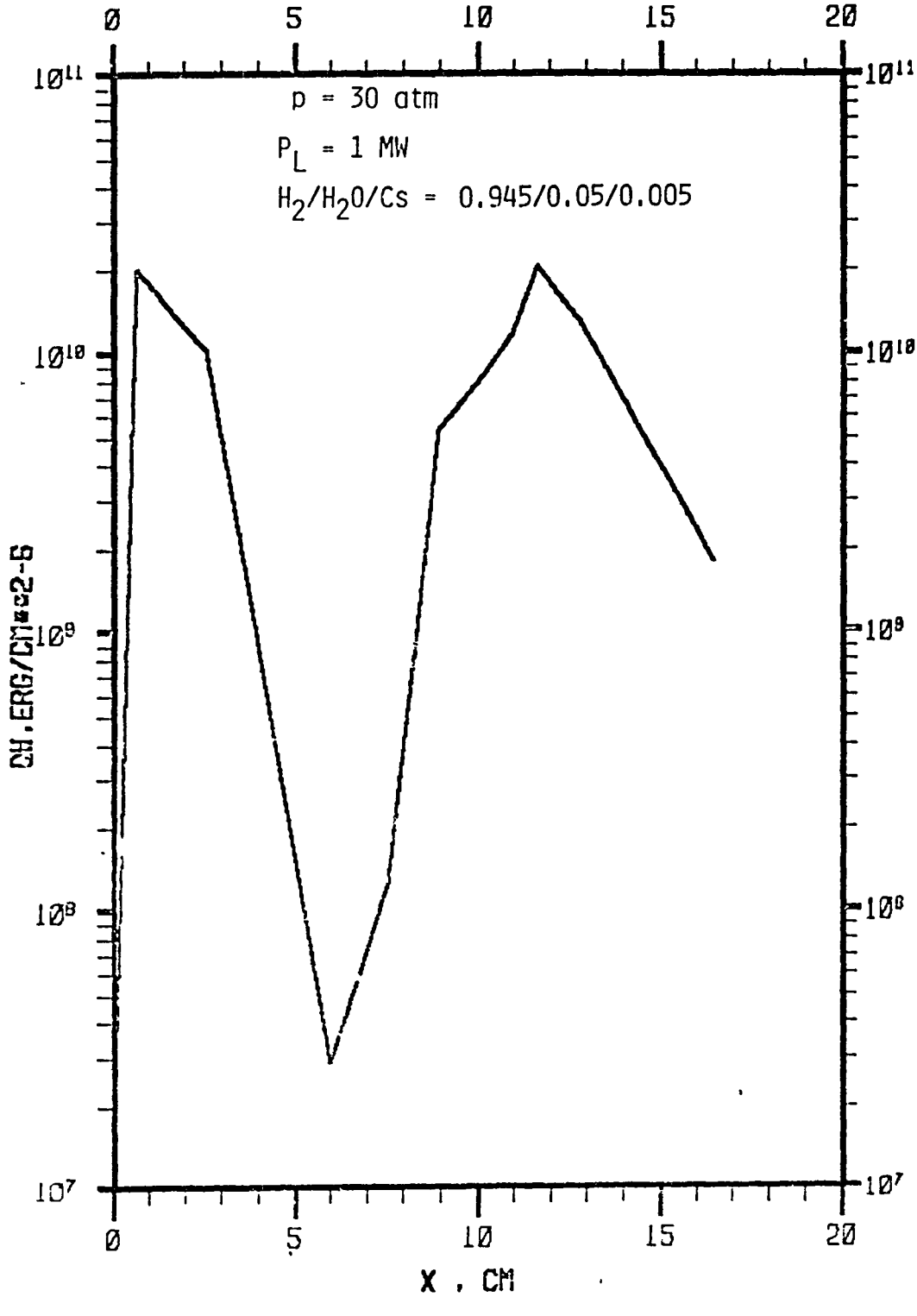

Figure 18 Distribution of wall heat transfer rate for continuously heated thruster from program LHTE.

The temperature profiles are presented in Fig. 14, and show an increase from the 1000 K inlet to 4000 K, and then a reduction to 3400 K as the energy transfer to the wall continues to take energy from the gas after the laser energy is fully absorbed.

The velocity profiles of Fig. 15 show a steady increase from the inlet velocity of 9.3 cm/s to a value of 150 cm/s at 16.482 cm. Of course, this factor of 15 acceleration still represents only a small velocity, and the reason can be sought in the wall radius distribution given in Fig. 16. It decreases rapidly from the initial value of 12.39 cm to 7 cm at x = 2.5 cm, and then rises to a peak after a further shallow minimum. Following the peak it decreases again. This shape is a result of the pressure gradient distribution input, which is $dp/dx = -2.745 \times 10^{-7}$ atm/cm, a constant. It is clearly not a realistic thrust chamber shape. The program must be exercised with different input functions dp/dx to learn how to make reasonable nozzle shapes.

The distribution of power in the gas is shown in Fig. 17. It rises as the laser energy is absorbed, and then decays as losses to the wall continue. It is 0.172 MW at 16.482 cm. The wall heat rate distribution is given in Fig. 18. It rises rapidly at the beginning because the rapid decrease in wall radius causes unabsorbed laser energy to hit the wall, which is by far the largest contribution to the wall heating there. The slow decrease after x = 0.7 cm is caused by the change in wall angle shown in Fig. 16, which means a smaller fraction of the laser intensity is normal to the wall. The rapid decrease starting at 3 cm again reflects a smaller wall slope seen in Fig. 16. When the wall radius begins to increase again, there is no longer laser heating of the wall since the beam is now blocked. However, the wall heating from the gas is beginning to rise as the gas heats up. This accounts for the increase in heating up to about 11 cm, where the wall radius peaks. From there on there is a slow further rise, and then a decay as the gas cools.

At 16.482 cm, there is 0.172 MW in the gas, 0.004 MW left in the laser beam, and 0.984 MW has been put into the wall. The total is 1.17 MW, compared to the input energy of 0.993 MW in the laser beam and 0.27 MW in the incoming gas flow, for a total of 1.02 MW incoming. This 15% discrepancy in energy balance is again caused mostly by inaccuracies in evaluating the integrals. However, it should be noted that the program does not contemplate walls which increase in radius, and the calculation of the laser energy being put into the wall is no longer correct when the wall radius begins to increase.

These two examples show the kind of results which can be obtained with the LHTE and CLHTE programs. However, the programs have not yet been exercised extensively enough to provide the experience necessary to make them useful tools for thrust chamber design. The relation between the input pressure gradient distribution and the output wall radius distribution must be explored, for example. When a body of computational results has been obtained and analyzed, these programs should provide the information necessary to continue the development of laser-heated thrusters.

A useful way to run these programs would be in conjunction with the simplified models discussed in the previous chapter. Those models could be used to define particular thrusters which seem interesting, and then the more elaborate programs described in this chapter could be used to provide the detailed information on those thrusters.

It should be pointed out that some of the modeling included in the three programs LSCWCS, LHTE and CLHTE needs improvement. One such area is the radiation modeling for H_2/Cs mixtures in LSCWCS and CLHTE. The present radiation model in the LSC wave program does not include cesium radiation, which may be an important radiator. In the thrust chamber program which couples to LSCWCS, namely CLHTE, the radiation model only goes up to about 6000 K. The effect of high temperature radiation from hydrogen and cesium needs to be included. Another set of parameters needing improvement is the viscosity and thermal conductivity in both LHTE and CLHTE. At present, the viscosity is that of hydrogen at 30 atm, and the thermal conductivity

is obtained by use of a constant Prandtl number. The representation of these transport properties should be improved and generalized to other pressures. Also, the mixing process at the interface between the LSC wave heated gas and the buffer gas in CLHTE should be considered more carefully, because of the very large velocity difference. Refinement of the stream function grid size should be attempted, to see if a non-uniform grid is needed, with closer spacing near the wall, to better define the wall boundary layer. The present pressure gradient subroutine provides only a constant value for that parameter. Other forms of this function should be tried, to learn how to produce desirable channel wall shapes.

IV. EXPERIMENTAL MEASUREMENTS OF ABSORPTION COEFFICIENT OF 10.6 μm RADIATION BY WATER VAPOR

In the continuous absorption mode, the propellant gas must be seeded with molecules which will absorb the laser energy starting at the gas inlet temperature. A possible low temperature absorber for 10.6 μm radiation is water vapor, which does not dissociate until about 4000 K. It was considered as an absorber in the Interim Report (Ref. 4), and a literature survey was made, resulting in a graph of the absorption coefficient (in cm^{-1} per amagat, where an amagat is 2.69×10^{19} particles per cm^3), versus 1000/T. This graph, from Fig. 2-5 of Ref. 4 is reproduced here as Fig. 19. Because of the temperature scale, room temperature is on the right near 3, and temperatures above 1000 K are on the left, between 1 and 0.

The dashed line on the left is caused by vibration-rotation line absorption and is calculated using a band model, with band parameters based on experimental data. The solid lines on the right are caused by continuum absorption, and have a pressure dependence, in addition to that from the particle density.

The few measurements of water vapor absorption in the literature up to late 1979 are also shown in Fig. 19. There is a group at low temperature between 400 and 500 K, and a group between 1535 and 2200 K. The latter points are calculated from measured spectral emissivities, and fall nearly on the dashed curve.

Based on this information we have drawn an estimated upper limit curve for line absorption, shown by the dot-dash line in Fig. 19. This is added to the continuum absorption at low temperature to obtain the absorption coefficient used in our modeling.

Recently, Fowler, Newman and Smith have presented a new calculation, and experimental measurements, for the water vapor absorption coefficient (Ref. 5). The results are shown as a plot of ku (cm^{-1}) vs T in Fig. 20, reproduced from Fig. 42 of Ref. 5. The dotted curve is a calculation for a specific equilibrium mixture of hydrogen and water, namely H_2/H_2O = 10/1 at

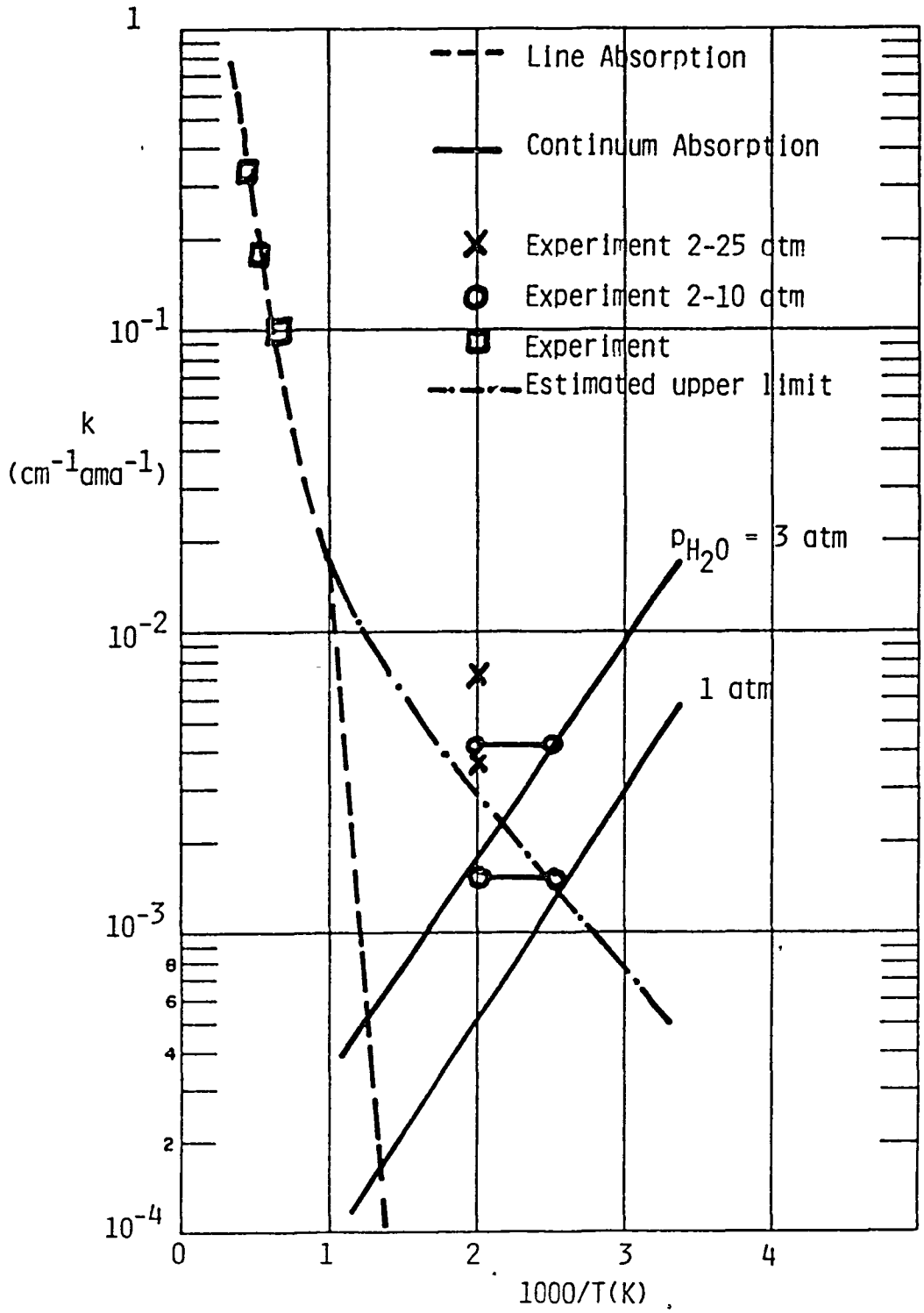

Figure 19 Absorption coefficient of 10.6 μm radiation in water vapor.

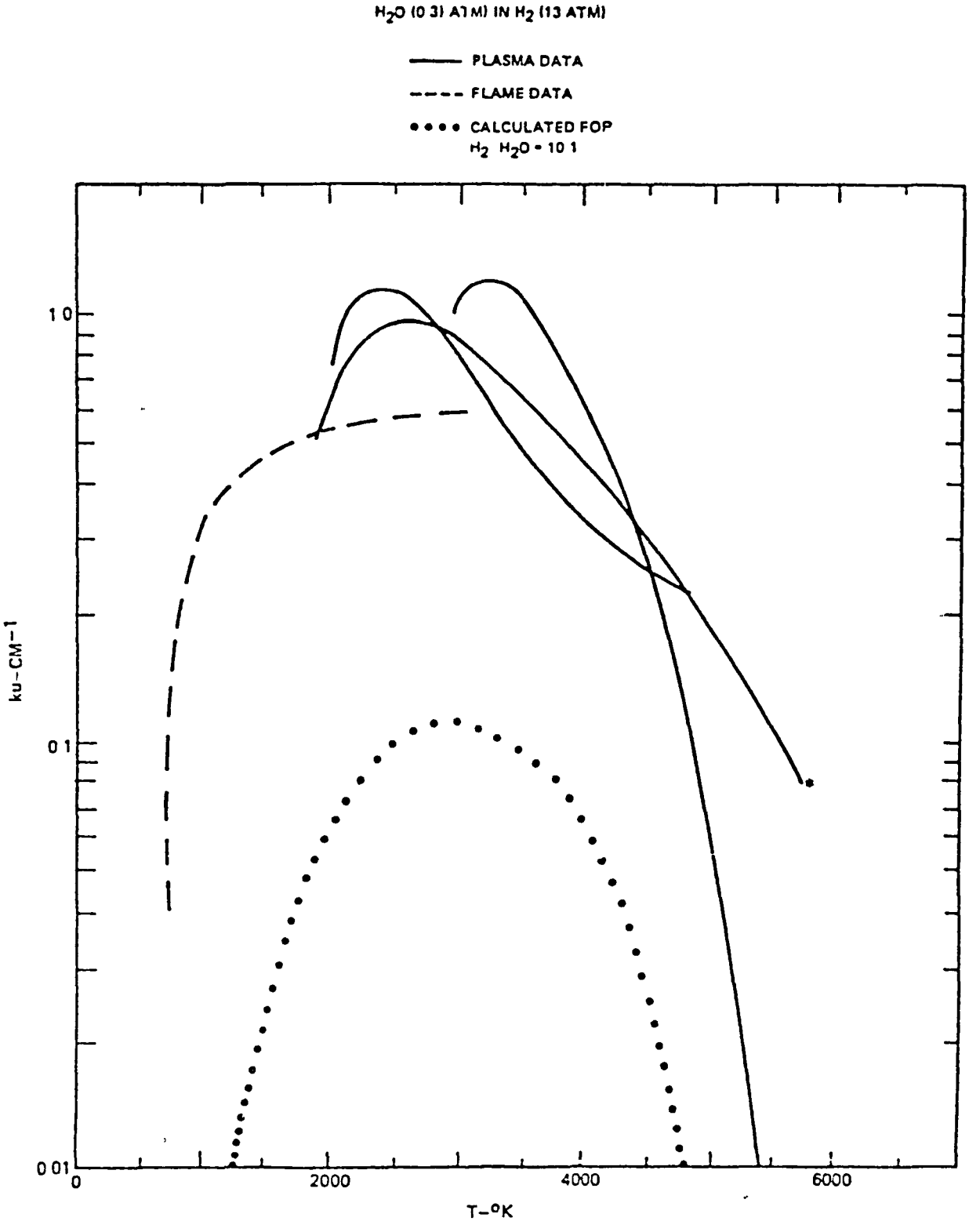

Figure 20 - Calculated and measured absorption coefficient of 10.6 μm radiation in water vapor from Fig. 42 of a report by Fowler, Newman and Smith of United Technologies Research Center (Ref. 5).

11 atm. The values correspond very closely with what would be obtained for the water vapor in that mixture by using the dashed line in our Fig. 19.

The experiments were performed in a laser heated mixture of 0.3 atm water vapor in 13 atm of hydrogen, using a probe laser to measure the absorption coefficient. Their results are given by the solid and dashed curves in Fig. 20. It can be seen that the measured values presented in Ref. 5 are at least an order of magnitude higher than those which they (or we) calculate between 1000 and 5000 K.

This survey of the literature on 10.6 μm absorption by water vapor shows two notable features. One is the minimum in the absorption near 500 K, which indicates undesirably small absorption coefficients at temperatures near the likely inlet gas temperature for a thruster. The second is the scarcity of measurements of the absorption, and the scatter near 500 K. The only measurement made by actual absorption of a laser line was that of Fig. 20 (Ref. 5), and it shows remarkably high values.

In view of the scarcity of good experimental results, and of the possible importance of water vapor as a molecular absorber, PSI has undertaken to measure the absorption coefficient in a shock tube. This has the advantage of providing a sample of hot water vapor which can be easily prepared, and whose properties can be defined with considerable precision (and considerable confidence). The absorption was measured using a probe CO_2 laser emitting radiation at the P20 line. Measurements were made both in the gas behind the incident shock and in the gas behind the reflected shock.

The measurements reported here are of a preliminary nature, representing the first data obtained from the experiment. The details of the experimental work are presented in Appendix I.

The results are shown in Fig. 21, where the absorption coefficient in cm^{-1} atm^{-1} is plotted against T, rather than 1000/T, to spread out the region of interest. There are 10 points presented, representing the incident and reflected measurements on five shots in mixtures of argon and water vapor. The arrows on the four left-most points indicate that the lower limit of the error bars is not known; indeed, the three left-most measurements yielded upper bounds only. The solid curve is a reproduction of the dashed curve of Fig. 19, the values currently being used by PSI in modeling. The

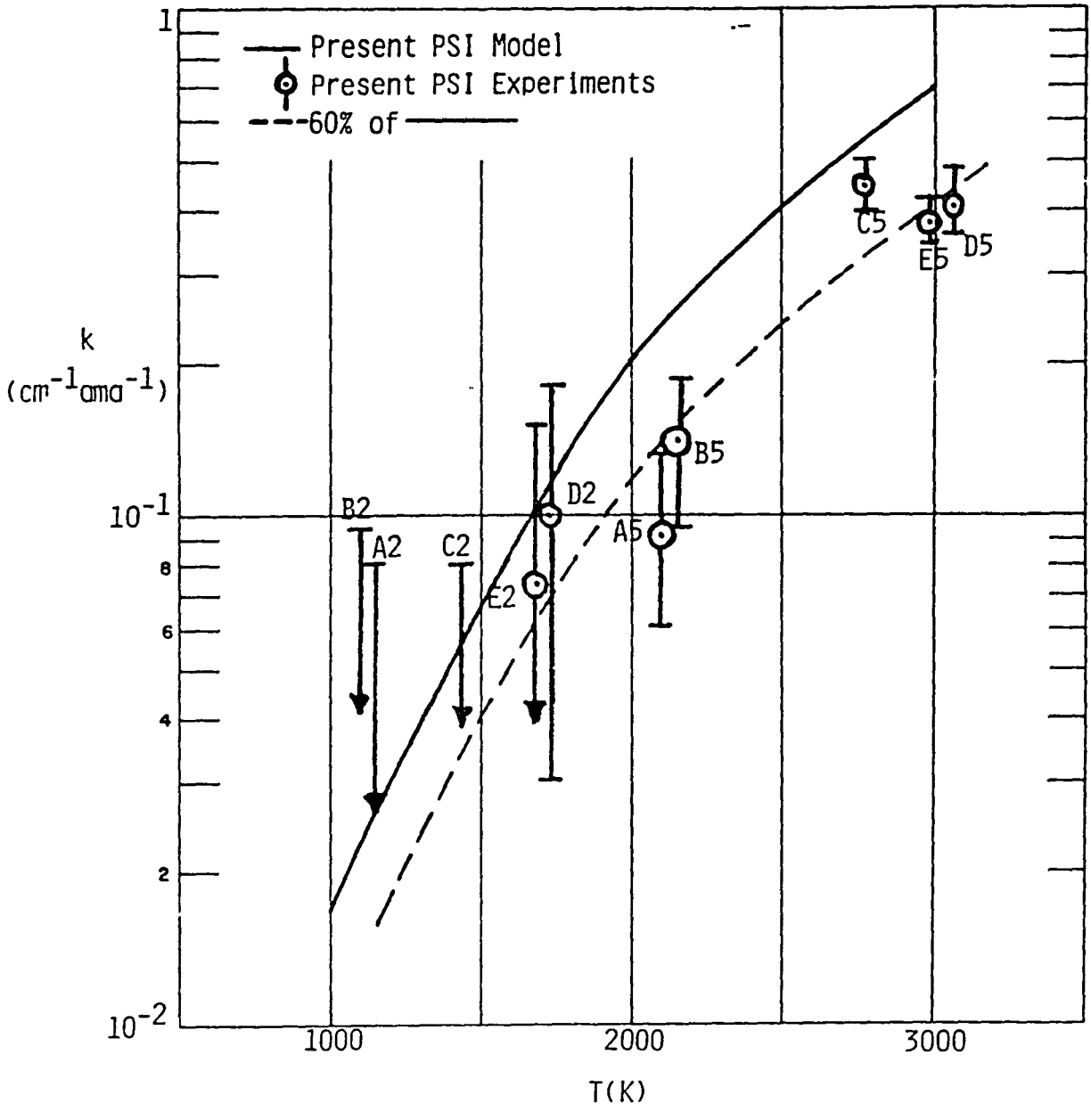

Figure 21 Measurements of the absorption coefficient of 10.6 μm (taken at the P(20) line) in water vapor from the present experiments.

dashed curve of Fig. 21 is drawn at 60% of the solid curve. It falls approximately through the mean of the data.

Although the preliminary nature of these measurements must be emphasized, as discussed more fully in Appendix I, indications are that the experimental results fall close to the calculations taken from the literature in the range 1100 to 3100 K. There is no evidence of the large absorption coefficients reported in Ref. 5, as shown in Fig. 20.

No change has been made in the values of water vapor absorption coefficient used in our modeling as a result of these experiments for several reasons. First, the results became available only at the end of the present effort. Second, the relatively small difference between the experimental results and the values being used, combined with the preliminary nature of the experiments, did not seem to warrant any changes as yet.

The experiments are being continued under other sponsorship, and when the work is completed, a more informed decision can be made as to the need for changing the absorption coefficients currently used in our computer models.

V. CONCLUSIONS

The research study, whose results are presented in the Interim Report (Ref. 4) and in the present report, had as its goal the development of computer programs useful for the design of thrust chambers for CW laser-heated thrusters. To accomplish that goal we have proceeded in three steps.

First, we have described the physical properties of some gases which are candidate propellants and seed gases. The properties include laser energy absorption properties, broad-band radiation and absorption properties, and thermodynamic and transport properties. In connection with the absorption of 10.6 μm radiation by water vapor, we have performed a preliminary shock tube experiment to measure the absorption coefficient.

Second, we have developed simplified models of thruster chambers for both the continuous mode and the LSC wave mode of laser heating. These models can be used for approximate but rapid parametric studies of laser-heated thrusters.

Third, we have developed detailed axisymmetric flow codes useful for thrust chamber design for both modes of laser heating just mentioned. These codes contain heating by absorption of laser energy, radial energy transport by conduction, and radiation energy transport and absorption. They have been delivered to NASA/Marshall Spaceflight Center and installed on a computer there.

The detailed conclusions which follow from the work accomplished are listed below. The first eight conclusions are repeated here from the Interim Report (Ref. 4) so that a complete list is collected in one place for easy reference. They refer to work reported in the Interim Report. Conclusions 9 through 12 refer to work reported in the present report.

1. For 10.6 μm radiation, a mixture of 1 part cesium to 99 parts atomic hydrogen substantially increases the absorption coefficient at low temperatures. The value of 0.1 cm is reached at 2000 K at 100 atm, 3000 K at 10 atm, and 12000 K at 1 atm.

2. For 10.6 μm radiation, water vapor has a minimum absorption coefficient at about 500 K, and appears to be quite low below 1000 K. However, the values in the vicinity of 500 K are not well-known, and the theoretical predictions have not been checked up to 1500 K by experiments. Experimental measurements between room temperature and 1500 K are needed.

3. For 5.3 μm radiation, water vapor is a good absorber from 300 to 3000 K. NO is a good low temperature absorber, and will not dissociate even though it is not an equilibrium state. CO is a good absorber above 2000 K, and remains chemically stable up to at least 6000 K.

4. For 10.6 μm radiation, a mixture of up to 5% water vapor in hydrogen does not provide good low temperature absorption.

5. For 5.3 μm radiation, both NO and water vapor up to 5% in hydrogen provide adequate absorption at low temperatures, though NO is the better absorber.

6. The continuously overlapping line model of molecular radiation provides results in good agreement with other calculations and with experiments.

7. Cesium is a strong radiator, and its radiation will be an important contributor for thrusters of operational size (10 cm radius). It is less important for laboratory size thrusters (1 cm radius), but still strong in certain bands.

8. The thermal conductivity of cesium-seeded hydrogen is nearly the same as for pure hydrogen. The viscosity, however, increases considerably because of the high molecular weight of cesium.

9. Some limited parametric studies have been made with the simplified models of thrust chambers. They show that the average wall heating rates are within a range that can be dealt with by current rocket practice, and that the laser powers needed are not

much larger than the power in the exhaust gas. At a low power level (30 kW CW 10.6 μm laser) they indicate that small-scale thrusters with measurable thrust can be tested.

10. The thrust chamber design programs produce results which are physically reasonable. However, they have only been used for a few sample calculations, and further experience with them is needed to explore their usefulness.

11. Several areas of the modeling in the thrust chamber design programs need improvement. The radiation modeling for high temperature hydrogen-cesium mixtures does not include cesium radiation at present, and cesium may be an important radiator even in small amounts of a percent or so. The representation of the transport properties of the seeded hydrogen mixtures needs to be improved. The mixing process between the LSC wave heated gas and the buffer gas should be modeled more accurately. Grid-refinement studies should be made to see if a non-uniform grid in the radial direction is needed. The effect of the input pressure distribution on the resulting channel wall shape should be studied.

12. The preliminary experiments on the absorption coefficient of water vapor for 10.6 μm radiation indicate values which are about 60% of the values used in the computer programs, in the temperature range from 1100 to 2100 K. This is considered at present to be good confirmation of the values used, which were obtained from the literature. The experiments are being continued at PSI under other sponsorship. As yet, no change in the modeling has been made based on the experimental results. When the ongoing experiments are completed, the results should be reviewed to see if the values in the computer programs need changing.

REFERENCES

1. Caledonia, G.E., Wu, P.K.S., and Pirri, A.N., "Radiant Energy Absorption Studies for Laser Propulsion," NASA CR-134809 (PSI TR-20) Woburn, MA, March 1975.

2. Kemp, N.H., Root, R.G., Wu, P.K.S., Caledonia, G.E., and Pirri, A.N., "Laser-Heated Rocket Studies," NASA CR-135127 (PSI TR-53), Woburn, MA, May 1976.

3. Kemp, N.H. and Root, R.G., "Analytical Studies of Laser Supported Combustion Waves in Hydrogen," NASA CR-135349 (PSI TR-97), Woburn, MA, August 1977.

4. Kemp, N.H. and Lewis, P.G., "Laser-Heated Thruster Interim Report," Contract NAS8-33097 (PSI TR-205), Woburn, MA, February 1980.

5. Fowler, M.C., Newman, L.A., and Smith, D.C., "Beamed Energy Coupling Studies," Final Technical Report for Contract No. F04611-77-C-0039, United Technologies Research Center, AFRPL TR-79-51, September 1979.

APPENDIX A

MODEL FOR CONTINUOUS HEATING MODE MAPS

It is important to find a simple model of the rocket performance and wall heating characteristics of a laser-heated thruster. Such a model will enable us to quickly survey the range of operating parameters and define in an approximate way the combination of parameters which may lead to useful thrusters.

Among the parameters of interest are the thrust F, the specific impulse, I_{sp}, the size, the pressure level, and the average wall heat flux.

In this appendix we will consider the continuous heating mode, in which the laser is absorbed continuously over the length of the heating zone. We model the heating zone as a cylinder of length L_h and radius R_h, through which a gas at uniform temperature T_h and pressure p is flowing at speed u. This cylinder represents the heating zone in a laser-heated thruster, as shown in Fig. A-1. We take the temperature to be the value after the laser has been absorbed which means the wall heating will be over-estimated, so the results will be on the conservative side. We take the gas to be in thermochemical equilibrium, so the pressure and temperature define its density ρ and enthalpy h, once the gas mixture is defined.

The mass flow rate is

$$\dot{m} = \rho u \pi R_h^2 \tag{A-1}$$

the total enthalpy is

$$H = h + u^2/2 \tag{A-2}$$

and the flowing gas is

$$P_G = \dot{m}H \tag{A-3}$$

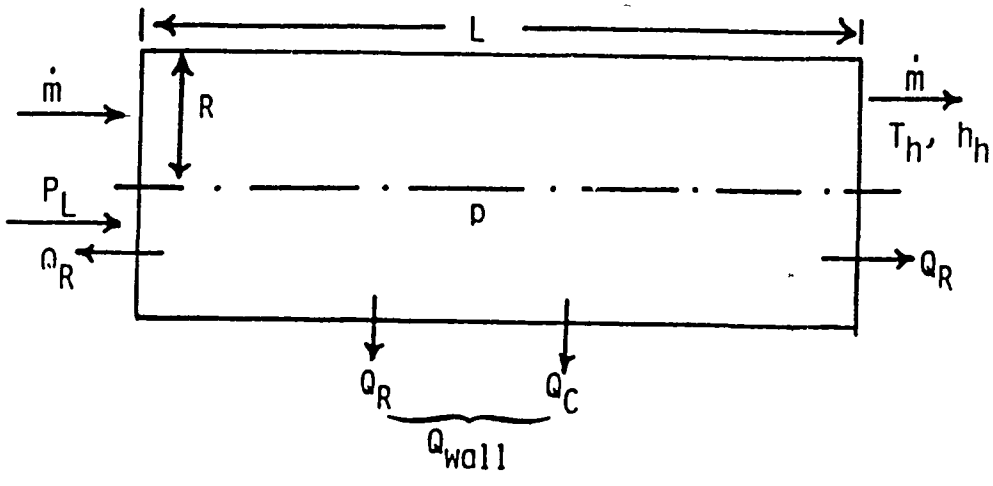

- Conserve mass & energy
- Momentum conservation → p constant
- $gI_{sp} = \left[2h_h + u_h^2\right]^{1/2}$
- $L = 1/k_L$
- $P_L = Q_{RTOT} + Q_C + \dot{m}(h_h + u_h^2/2)$
- $\bar{Q}_W = (Q_R + Q_C)/2\pi RL$

Figure A-1 Simplified Continuous Heating Model

The thrust that can be extracted from this gas, if it is expanded to zero enthalpy is

$$F = \dot{m}\, u_{ex} \tag{A-4}$$

where the exhaust velocity at zero enthalpy is

$$u_{ex} = (2H)^{1/2} \tag{A-5}$$

The corresponding specific impulse is

$$I_{sp} = u_{ex}/g \tag{A-6}$$

The hot gas will emit radiation at a rate $Q_{R_{tot}}$, part of which is to the side walls, say Q_R. It will also transfer heat to the side walls of the cylinder at a rate Q_C, so the total heat rate to the side walls is

$$Q_{wall} = Q_R + Q_C \tag{A-7}$$

and the average wall heat flux is

$$\bar{Q}_w = (Q_R + Q_C)/(2\pi R_h L_h) \tag{A-8}$$

To maintain a steady state, power must be supplied by the laser, to provide the gas power P_G, the total radiated power $Q_{R_{tot}}$ and the convective power Q_C. Therefore, the laser power P_L is

$$P_L = P_G + Q_{R_{tot}} + Q_C \tag{A-9}$$

The gas power depends only on the thrust and specific impulse, as can be seen from Eqs. (A-3), (A-5) and (A-4):

$$P_G = g\, I_{sp}\, F/2 \tag{A-10}$$

If I_{sp} and F are given, P_G is not dependent on the size of the thruster.

The energy losses, on the other hand, are dependent on size. The convective heating can be estimated from laminar boundary layer theory, since these are fairly low-speed flows with moderate Reynolds numbers. The formulation of compressible boundary layer theory is in terms of the gas-stream density ρ and viscosity μ, and the density, viscosity, thermal conductivity, and specific heat at the wall, ρ_w, μ_w, λ_w and c_{pw}. The variables used are ξ and η, which are related to the distances along and normal to the wall, x and y, by

$$\xi = \int_0^x \rho \mu u \, dx, \qquad \eta = \rho u \int_0^y [\rho(x,y)/\rho] dy/(2\xi)^{1/2}$$

where ρ (x,y) is the local density in the boundary layer.

In these terms the local convective heat flux to the wall is

$$q_w = \frac{\lambda_w \rho_w \, uH}{c_{pw}(2\xi)^{1/2}} \left(\frac{\partial g}{\partial \eta}\right)_w$$

where $g = H(x,y)/H$, the local to stream total enthalpy ratio. The gradient $(\partial g/\partial \eta)_w$ must be obtained by integration of the boundary layer equations. For the present case of constant properties in the axial (x) direction, the expression for ξ can be integrated so q_w becomes

$$q_w = \left[\frac{\rho_w \mu_w}{\rho \mu \, Pr} \left(\frac{\partial g}{\partial \eta}\right)_w\right] Hu \left(\frac{\rho\mu}{2ux}\right)^{1/2} \qquad \text{(A-11)}$$

where $Pr = c_p \mu/\lambda$, the Prandtl number.

The quantity in square brackets comes from boundary layer theory, and does not depend on x in the present uniform flow. If we let

$$G' = \frac{\rho_w \mu_w}{\rho \mu \, Pr} \left(\frac{\partial g}{\partial \eta}\right)_w \qquad \text{(A-12)}$$

we can then integrate Eq. (A-11) over the cylindrical surface of radius R_h and length L_h to get

$$Q_C = \int_0^{L_h} 2\pi R_h q_w \, dx = 2\sqrt{2\pi}\, G' H\sqrt{\mu \dot{m} L_h} \qquad \text{(A-13)}$$

This shows that Q_C is proportional to $\sqrt{u}$, since $\dot{m}$ is proportional to u and H is nearly independent of u in these subsonic, hot flows. Thus, Q_C vanishes, i.e., $\dot{m} = 0$. Q_C is also proportional to $H \approx h$, and increases as the flow temperature is increased.

A suitable value of G' can only be found by referring to boundary layer calculations. We are interested here in a gas composed mostly of hydrogen, and hydrogen boundary layer calculations have been reported in Ref. A-1. Based on these calculations, a good average value of G' is 0.7, which means that Eq. (A-13) yields

$$Q_C = 3.5\, H\sqrt{\mu \dot{m} L_h} \qquad \text{(A-14)}$$

This is the expression we have used in the map calculations performed during the present study.

The radiation emitted by the gas depend both on the geometry of the gas sample, and on its radiative properties. The radiative properties depend on the gas composition, pressure, and temperature, and are expressed in terms of an absorption coefficient k_ν, which depends on the frequency of the radiation, ν. We have studied k_ν for gases of interest. For temperatures up to 6000K, information on k_ν is provided in Chapter III of Ref. A-2. For hydrogen at higher temperatures, the work reported there has been extended, and is reported in Appendix C of the present report.

The geometrical dependence of the radiation required here is associated with a uniform gas cylinder of radius R_h and length L_h. We need the total radiation emitted, $Q_{R_{tot}}$, and that portion emitted out the cylindrical surface. Appendix D is devoted to an approximate calculation of these quantities in terms of k_ν. The results are expressed using k_ν, R_h, L_h and the black body function

$$B_\nu = \frac{2\pi h_P \nu^2 \; 3}{\exp(h_P \; c_1/kT)-1} \qquad \text{(A-15)}$$

where h_p, k and c are the Planck constant, the Boltzmann constant, and the speed of sound. Rather than use the frequency ν, we use the wave number $\omega = \nu/c$. The result for total radiation is

$$Q_{R_{tot}} = 2\pi R_h L_h \left(1 + \frac{R_h}{L_h}\right) \int_0^\infty B_\omega \left\{1 - \exp\left(\frac{-2k_\omega R_h}{1 + R_h/L_h}\right)\right\} d\omega$$

$$= 2\pi R_h L_h \left(1 + \frac{R_h}{L_h}\right) \varepsilon \left(L = \frac{2 R_h}{1 + R_h/L_h}\right) \sigma T^4 \qquad \text{(A-16)}$$

For radiation to the side walls, the expression depends on the cylinder aspect ratio.

$L_h/R_h \geq 1$:

$$Q_R = Q_{R_{tot}} \Big/ (1 + R_h/L_h) \qquad \text{(A-17a)}$$

$L_h/R_h < 1$:

$$Q_R = 2\pi R_h L_h \int_0^\infty B_\omega \left\{1 - \exp(-k_\omega \ell)\right\} d\omega \qquad \text{(A-17b)}$$

$$= 2\pi R_h L_h \varepsilon(\ell) \sigma T^4$$

$$\ell = \frac{16}{3\pi} \frac{R_h^2}{L_h} \left[\frac{G}{(K_2)^{3/2}} - 1\right], \quad K_2 = \left[1 + \left(\frac{L_h}{2R_h}\right)^2\right]^{-1}$$

$$G = 0.75(1-K_2) \left[1 - \tfrac{1}{2}(1-K_2)\right] \ln\left[16/(1-K_2)\right]$$

$$+ 1 - 2.25(1-K_2) + 0.25(1-K_2)$$

The integrations are performed over the ω range for which B_ω is significant. For $T \leq 6000K$, the range used is $\omega = 1000$ to $10^5 cm^{-1}$.

We can now describe how this model is used for an approximate calculation of a laser-heated thruster in the continuously heated mode:

1) Specify the gas mixture, pressure and temperature of interest.

2) Calculate the gas enthalpy, density and chemical composition from a thermochemical equilibrium program. (The I_{sp} to be found below will be approximately $\sqrt{2h}$.)

3) Choose the length L_h of the cylinder. In the calculations made here we have chosen $L_h = 1/k_L$, where k_L is the absorption coefficient of the gas mixture at the pressure and temperature chosen, for the laser wave-length of interest. This is certainly a characteristic length of the absorption zone, but it is the shortest such length, since the temperature chosen is that of the fully heated gas, and k_L increases with T. A possible refinement to the calculation is to choose some combination of the absorption coefficients of the inlet gas and the high temperature gas. The values of k_L are found by using the expressions given in Chapter III of Ref. A-2.

4) Choose a desired radius R_h and thrust F.

5) Find the gas flow speed from Eqs. (A-1), (A-2), (A-4) and (A-5). These provide a quadratic in u^2 whose solution is

$$u^2 = -h + \left[h^2 + (F/\rho \pi R_h^2)^2\right]^{1/2} \qquad \text{(A-18)}$$

6) Find H, $\dot{m}$, P_G, I_{sp} from Eqs. (A-2), (A-1), (A-3) and (A-6).

7) Find the heating terms Q_C, $Q_{R_{tot}}$, Q_R from Eqs. (A-14), (A-16) and (A-17). In Eq. (A-14), the gas viscosity is approximated as that of hydrogen, which is given in Table A-1, as calculated by the method described in Chapter IV of Ref. A-2. As pointed out there, small fractures of heavy seeds like cesium can increase the viscosity of the mixture by as much as a factor of 2 over pure hydrogen. However, the convective heat transfer term is already approximate because of the choice of G', and it only depends on the square root of μ, so for this simple model, it was not felt worth while to consider the dependence of μ on gas composition.

8) Find the wall heat load Q_{wall} and average wall heat flux $\bar{Q}_w$ from Eqs. (A-7) and (A-8).

9) Find the laser power P_L from Eq. (A-9).

TABLE A-1

VISCOSITY OF EQUILIBRIUM HYDROGEN

(in 10^{-5} kg/m-s)

$T(10^3 K)$	Pressure (atm)				
	1	3	10	30	100
1	1.98	1.98	1.98	1.98	1.98
2	3.13	3.13	3.13	3.13	3.13
3	4.48	4.42	4.39	4.37	4.36
4	5.27	5.58	5.68	5.64	5.55
5	5.54	5.78	6.25	6.77	7.13
6	6.54	6.59	6.74	7.06	7.62
7	7.33	7.35	7.40	7.55	7.94
8	8.32	8.34	8.38	8.45	8.66
9	9.10	9.18	9.23	9.30	9.42
10	9.72	9.95	10.1	10.2	10.3
11	9.97	10.5	10.9	11.1	11.2
12	9.54	10.6	11.3	11.7	12.0
13	8.49	10.2	11.5	12.2	12.7
14	6.95	9.30	11.3	12.5	13.3
15	5.25	7.93	10.5	12.3	13.6
16	3.76	6.49	9.66	12.1	14.0
17	2.56	4.91	8.21	11.1	13.6
18	1.80	3.63	6.74	9.96	13.0
19	1.32	2.70	5.44	8.75	12.3
20	1.04	2.06	4.34	7.54	11.4
21	0.881	1.64	3.48	6.41	10.4
22	0.824	1.42	2.85	5.44	9.43
23	0.776	1.26	2.40	4.67	8.52
24	0.756	1.15	2.08	4.05	7.69
25	0.754	1.10	1.98	3.58	6.97

This procedure has been implemented in a small computer program which uses the equilibrium state and k_L as input. Calculations have been made for a number of cases. The results are presented in the main body of this report.

REFERENCES FOR APPENDIX A

A-1 Wu, P.K., "Similarity Solutions of the Boundary-Layer Equations for Laser Heated Flows," AIAA Journal, Vol. 11, Nov. 1976, pp. 1659-1661.

A-2 Kemp, N.H. and Lewis, P.F., "Laser-Heated Thruster Interim Report," Contract NAS8-33097 (PSI TR-205), Woburn, MA, February 1980.

APPENDIX B

MODEL FOR LSC WAVE HEATING MODE-MAPS

This Appendix describes a simple model of a laser-heated thruster which uses an LSC wave mechanism to absorb most of the energy of the laser. Since that mechanism produces a high temperature gas (~20,000K in pure hydrogen), it is hard to contain by walls, and produces a great deal of radiation. To make it useful as a thruster, we consider surrounding the heated gas by a co-flowing buffer gas of the same mixture, but unheated by the laser. This buffer gas will be heated by the laser-heated gas by both convection and radiation. The two gas streams will mix and ultimately produce a single stream at some temperature between that of the hot gas exiting the LSC wave and that of the incoming buffer gas. The buffer gas will also serve to produce the convective and radiative heating to the walls.

A schematic diagram of such a heater is shown in Fig. B-1. The over-all size is radius R_m and length $L_h + L_m$. Flow at state $(\ )_1$ enters the heater. In the center, over a radius R_h, a laser beam of power P_L enters, inducing an LSC wave in the cylinder of length L_h. This hot cylinder radiates energy Q_{Rh}, some of which escapes out the side to the walls, and some of which is absorbed in the cooler buffer gas in the annulus R_m-R_h. There is also convective heating from the hot gas to the buffer gas along the edge of the hot cylinder. Starting at L_h, the gases mix, and at the exit of the heating region they emerge as one stream with properties $(\ )_{mf}$. In the mixing region, the gases lose heat to the side walls by convection, Q_{Cm}, and radiation, Q_{Rm}. Heat is also radiated out the ends of the mixing region, ΔQ_{Rm}. No radiation out the ends of the LSC wave cylinder is considered, as it is all absorbed in the oncoming gas and the mixed gas.

This model permits a straightforward calculation of the flow parameters and losses to be made by using conservation of mass, momentum and energy. Actually, momentum conservation is replaced by the condition of

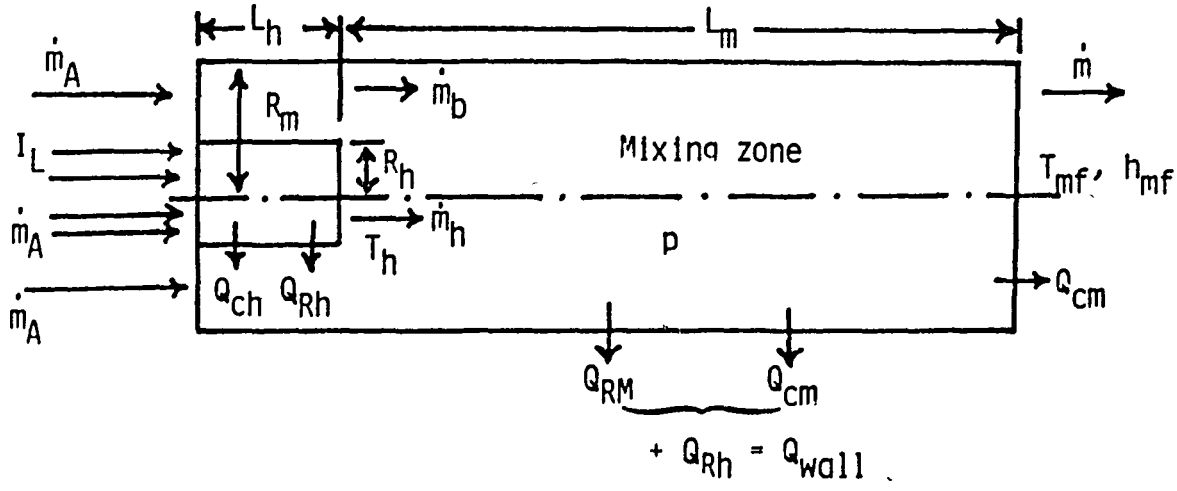

- Conserve mass & energy
- Momentum conservation → p constant
- $aI_{sp} = \left[2h_{mf} + u_{mf}^2\right]^{1/2}$
- $L_m = 2\ R_m$, $L_h = 1/k_{vuv}$
- $P_L = Q_{Rmtot} + Q_{Rh} + Q_{cm} + \dot{m}(h_{mf} + u_{mf}^2/2)$
- $\bar{Q}_w = (Q_{Rh} + Q_{Rm} + Q_{cm})/2\pi R_m L_m$
- I_L related to p and $\dot{m}_A$

Figure B-1 Simplified LSC Wave Heating Model

constant pressure throughout, leaving the mass and energy equations to provide us with the relations necessary for the calculation.

Let us denote the gas conditions at the end of the LSC wave region (hot region) by $(\ )_h$ and those at the end of the buffer region by $(\ )_b$. Then over-all mass conservation requires that

$$\dot{m} = \dot{m}_b + \dot{m}_h = \rho_1 u_1 S_m = \rho_1 u_1 \pi R_m^2 = \rho_{mf} u_{mf} S_m \tag{B-1}$$

where S_m is the cross-sectional area of the cylinder. The stagnation enthalpy at the end of cylinder is

$$H_{mf} = h_{mf} + u_{mf}^2/2 \tag{B-2}$$

and the power in the gas is, with P_1 the input gas power,

$$P_G = \dot{m} H_{mf} - P_1, \quad P_1 = \dot{m} H_1 \tag{B-3}$$

The thrust resulting from expanding this flow to zero enthalpy is

$$F = \dot{m} u_{ex} \tag{B-4}$$

where the exhaust velocity is

$$u_{ex} = (2H_{mf})^{1/2} \tag{B-5}$$

and the corresponding specific impulse is

$$I_{sp} = u_{ex}/g \tag{B-6}$$

These relations are the same as those in Eqs. (A-1)-(A-6) for the thruster performance, once the gas is heated and mixed to the $(\ )_{mf}$ state.

The radiation associated with the mixing region flow is composed of the total emission $Q_{Rm_{tot}}$, the radiation to the cylinder side wall

$Q_{Rm} = Q_{Rm_{tot}} - \Delta Q_{Rm}$. These are calculated from the pressure, temperature T_{mf}, and cylinder geometry R_m, L_m by the formulas given in Appendix A, Eqs. (A-16) and (A-17), using the appropriate gas composition.

The convective heating is found from Eq. (A-14) of Appendix A, using H_{mf}, L_m, and the viscosity u_{mf} at T_{mf}, according to

$$Q_{Cm} = 3.5\ H_{mf} \sqrt{\mu_{mf}\ \dot{m}\ L_m} \tag{B-7}$$

To obtain information about the conditions at this exit of the hot region we write an energy balance between the station L_h and the end of the cylinder. The energy flow emerging from the hot region is $\dot{m}_h H_h$. That emerging from the buffer region is $\dot{m}_h H_1 + Q_{Ch} + Q^*_{Rh} - Q_{Cb}$. Here Q_{Ch} is the convection loss from the hot region, which we take to be deposited in the buffer gas. It is given by the formula analogous to Eq. (B-7) as

$$Q_{Ch} = 3.5\ H_h \sqrt{\mu_h\ \dot{m}_h\ L_h} \tag{B-8}$$

Q_{Cb} is the energy lost to the wall by convection from the buffer gas, which we will ignore as small, since the buffer gas is much cooler than the hot region gas. Finally, Q^*_{Rh} is that portion of the radiation from the hot region which is absorbed in the cold region. It is found by subtracting from the radiation emitted by the hot region, Q_{Rh}, that portion which can escape through the buffer gas to the walls, Q_{Rh}.

For hydrogen, these quantities are found as follows. Q_{Rh} comes from using Eqs. (A-17), with the integration on ω carried as far as necessary to obtain significant contributions; in all calculations we have integrated to $\omega = 2 \times 10^5\ cm^{-1}$, with k_ω taken from the high temperature hydrogen radiation properties described in Appendix C. The part which can escape through the buffer gas is calculated the same way, but only integrated up to $= 9 \times 10^4\ cm^{-1}$, since the higher energy part of the radiation is absorbed in the cooler buffer gas.

The sum of the energy flows emerging from the buffer and hot regions either emerges from the end of the mixing region as $\dot{m} H_{mf}$, or goes to

the walls as radiation from the mixing region, $Q_{Rm_{tot}}$, or convection Q_{Cm}.

The energy balance from station L_h to station $L_h + L_m$ is then

$$\dot{m}_h H_h + \dot{m}_b H_1 + Q_{Ch} + Q^*_{Rh} = \dot{m} H_{mf} + Q_{Rm_{tot}} + Q_{Cm} \tag{B-9}$$

This can be considered a quadratic equation for $\dot{m}_h^{1/2}$, since $\dot{m}_b = \dot{m} - \dot{m}_h$, and Q_{Ch} depends on $\dot{m}_h^{1/2}$, Eq. (B-8). Its solution is

$$\dot{m}_h^{1/2} = \frac{-3.5\, H_h \sqrt{L_h \mu_h}}{2(H_h - H_1)} + \left\{ \left[\frac{3.5\, H_h}{2(H_h - H_1)} \right]^2 L_h \mu_h + \frac{\dot{m}(H_{mf} - H_1) + Q_{Rm_{tot}} + Q_{Cm} - Q^*_{Rh}}{H_h - H_1} \right\}^{1/2} \tag{B-10}$$

We can now set up a procedure for calculating the performance of an LSC wave heated thruster with a buffer gas. The parameters to be specified are partly determined by convenience of calculation and partly by the properties of LSC waves. It is known (Ref. B-1, for example) that there is a relation between laser intensity and mass flow rate per unit area for LSC waves. This relation should be maintained for the calculations with this simplified model. Therefore, we choose the input mass flow per unit area $\dot{m}_A = \rho_1 u_1$ as a parameter specified in the calculation. In order to make the thermochemical calculations as simple as possible, we specify p and T to determine the state of the gas, wherever we need it. With these constraints, the calculation proceeds as follows:

1) Specify the gas mixture, pressure p, thrust F, inlet temperature T_1, mass flow per unit area $\dot{m}_A$, and final mixed temperature T_{mf}.

2) Calculate the enthalpy h_{mf}, density ρ_{mf}, and chemical composition from a thermochemical equilibrium program.

3) Calculate $u_{mf} = \dot{m}_A/\rho_{mf}$, H_{mf} from Eq. (B-2), $\dot{m}$ from Eqs. (B-4) and (B-5), R_m from Eq. (B-1), I_{sp} from Eqs. (B-5) and (B-6).

4) Calculate h_1 and ρ_1 from p, T_1 using perfect gas properties; then $u_1 = \dot{m}_A/\rho_1$, and $H_1 = h_1 + u_1^2/2$, and the input power $P_L = \dot{m} H_1$.

5) Choose L_m, the length of the mixing region. This choice can be based on a length of mixing, or some other suitable interim. For the calculations made in this study we have chosen $L_m = 2\ R_m$.

6) Calculate the heating terms Q_{Cm}, $Q_{Rm_{tot}}$ and Q_{Rm} from Eqs. (B-7), (A-16) and (A-17). In Eq. (B-7), the viscosity μ_{mf} is approximated by the value for hydrogen from Table A-1.

7) Calculate the power in the gas at the end of the mixing region by Eq. (B-3).

8) Choose the temperature T_h at the end of the LSC wave (hot region) and calculate the corresponding gas composition from a thermochemical equilibrium program, including enthalpy h_h and density ρ_h.

9) Find the velocity $u_h = \dot{m}_A/\rho_h$ and total enthalpy $H_h = h_h + u_h^2/2$.

10) Choose the length of the hot region, L_h. This should be a length characteristic of the thickness of the LSC wave. It is not the absorption length at T_h, since this is usually very small. In LSC waves, the thickness is determined by the distance over which the cold incoming gas is heated up to a temperature at which it can absorb the laser energy. This heating is caused by conduction and radiation forward from the hot absorbing part of the wave. In hydrogen, the length over which this heating occurs is characterized by the absorption length for vacuum ultra-violet radiation emitted by the hot hydrogen. According to Appendix D of Ref. B-1, this length is, in cgs units,

$$\kappa_{vuv} = 6.34 \times 10^{-18}\ (2\ n_H/Q_{eH}) \qquad \text{(B-11)}$$

where n_H is the hydrogen number density, and Q_{eH} is the electronic partition function for hydrogen atoms For the pure hydrogen calculations done in the present study, we have taken $L_h = 1/k_{vuv}$.

11) Guess a radius R_h of the hot region. Then calculate the radiation from the hot region, as described above, by using Eqs. (A-17) integrated over the whole significant wavenumber regime (0 to 200,000 cm^{-1} in the cases calculated here). This gives the total sideways emission

Q_{Rh}. Then use the same equations to find that part of the sideways emission, Q'_{Rh}, which can escape through the buffer gas to the walls, by integrating over the appropriate portion of the wavenumber spectrum (0 to 90,000 cm^{-1} in the cases calculated here). Subtraction then yields $Q^*_{Rh} = Q_{Rh} - Q'_{Rh}$, the power absorbed by the buffer gas.

12) Calculate the mass flow rate $\dot{m}_h$ through the hot region from Eq. (B-10), which then gives the radius of the hot region from $\pi R_h^2 = \dot{m}_h/\dot{m}_A = \rho_h u_h$. If this radius is not the same as the one guessed in Step 11 above, iterate between Steps 11 and 12 until the radius calculated from Eq. (B-10) is the same as the one used to find the radiation in Step 11.

13) Calculate the laser power as the power in the gas at the end of the mixing zone, plus the power put into the walls:

$$P_L = P_G + Q_{Rm_{tot}} + Q_{Cm} + Q'_{Rh} \tag{B-12}$$

The laser intensity is then $I_L = P_L/\pi R_h^2$.

14) The total wall heat load is

$$Q_{wall} = Q_{Cm} + Q_{Rm} + Q'_{Rh} \tag{B-13}$$

and the average wall heat flux is

$$\bar{Q}_w = Q_{wall}/2\pi R_m(L_h + L_m) \tag{B-14}$$

15) To satisfy the constraint that the input value of $\dot{m}_A$ is appropriate for a given laser intensity I_L, we may iterate on any other of the input parameters such as T_{mf}, F, or T_h. Only one need be changed, as only one output parameter, I_L, is being sought. We have found it convenient to iterate on T_h, since the thrust F often has a desired value, and T_{mf} almost completely determines I_{sp}, which also often has a desired value.

The procedure through step 14 has been implemented in a small computer program for pure hydrogen propellant. It takes as input the equilibrium properties of hydrogen at the two states p, T_{mf} and p, T_h. The iteration on I_L, or any other parameter, is done manually using multiple runs of this computer program.

A number of calculations of typical cases have been performed with this program, and the results are discussed in the main body of this report.

REFERENCE FOR APPENDIX B

B-1 Kemp, N.H. and Root, R.G., "Analytical Studies of Laser Supported Combustion Waves in Hydrogen," NASA CR-135349 (PSI TR-97), Woburn, MA, August 1977.

APPENDIX C

HYDROGEN RADIATION AT HIGH TEMPRATURE

Radiation from hydrogen species is discussed in Chapter III of Ref. C-1. However, the expressions given there are limited to a temperature regime up to 10,000 K. For the case of LSC waves, especially in pure hydrogen, temperatures up to 20,000 K, or somewhat higher, are of interest. Such waves are modeled in the hot regime of the simple model described in Appendix B, as well as in the detailed structure of hydrogen LSC waves described in Ref. C-2. Therefore, we need to extend the radiative properties of hydrogen to these higher temperatures.

There are two effects which enter as higher hydrogen temperatures are considered. First, the significant part of the frequency spectrum extends to higher values, which is to say, to higher wavenumbers, because of the shape of the black body spectrum. As temperature increases, the peak of the blackbody curve shifts to higher frequency, and its fall-off also shifts to higher frequency. For a temperature of 10,000 K, the black body curve has fallen to about 10^{-3} of its peak value when the wavenumber is 10^5. The same degree of fall-off at 20,000 K requires a wavenumber of 2×10^5. Integrations over wavenumber, which were carried out to wavenumber $\omega = 10^5$ in Ref. C-1, were extended to $\omega = 2 \times 10^5$ for high temperature hydrogen.

The second effect of high temperature is the inclusion of hydrogen line radiation, to be added to the continuum radiation considered at low temperature. Most lines can be treated as extensions of the continuum radiation for a simple model. However, the Lyman alpha (Ly_α) and Balmer alpha (H_α) lines may be strong enough to be treated separately.

The model we have adopted for the absorption coefficient of high temperature hydrogen is described below. It consists of modifying the free-bound hydrogen absorption coefficient given in Ref. C-1 to allow for wavenumbers up to 2×10^5, of adding terms to model the lines as an extension of the continuum, and of adding the Ly_α and H_α lines.

We start with the expression for the free-bound absorption coefficient of hydrogen atoms given in Eq. (3-20) of Ref. C-1.

$$k_H = \sigma_H \, n_H \left(1 - e^{-h_p c\omega/kT}\right) \tag{C-1}$$

Here σ_H is the cross-section, n_H the atom number density, h_p the Planck constant, c the speed of light, ω the wavenumber and k the Boltzmann constant. The cross-section is expressed in the equation above Eq. (3-20) in Ref. C-1 in cgs units, as

$$\sigma_H = \frac{2 \times 7.9 \times 10^{-18}}{Q_{e\ell H}} \sum_{N > \sqrt{Ry/\omega}}^{N_{max}} \left(\frac{Ry}{N\omega}\right)^3 \exp\left[-\frac{h_p c \, Ry}{kT}\left(1 - \frac{1}{N^2}\right)\right] \tag{C-2}$$

where Ry = 109737 cm^{-1} and the electronic partition function of the hydrogen atom is

$$Q_{e\ell H} = 2 \sum_{N=1}^{N_{max}} N^2 \exp\left[-\frac{h_p c \, Ry}{kT}\left(1 - \frac{1}{N^2}\right)\right] \tag{C-3}$$

N_{max} is the largest principal quantum number of an electronic state of hydrogen to be used in the sums. At low temperatures, the choice of this cut-off quantum number does not matter much, since the larger N terms make little contribution to the sums. However, as T increases, this ceases to be true and a realistic cut-off must be chosen. While in the low temperature work of Ref. C-1 we chose $N_{max} = 40$, we have chosen $N_{max} = 10$ in the present high temperature case. A more sophisticated cut-off procedure was not considered worthwhile for the present rather simple model.

The first modification to Eq. (C-2) is for the N = 1 term, which never arose when $\omega < 10^5 <$ Ry, since then the lower limit was always $N \geq 2$.

But if we extend the range of ω to 2×10^5, the N = 1 term will appear for the higher wavenumbers. This term is given in Ref. C-3, Eq. (5-17), as the last term on the right. In the present units $13.6/\omega = Ry/\omega$, and the ground state number density $n_{AG} = 2n_H/Q_{elH}$. Thus the N = 1 term in the sum in Eq. (C-2) is $6.34 \times 10^{-18} (Ry/\omega)^{8/3}$.

To add the lines as an extension of the continuum we write Eq. (C-2) as

$$\sigma_H = \frac{2}{Q_{elH}} \sum_{N=1}^{10} A_N \qquad \text{(C-4a)}$$

The A_N are chosen at each ω as follows. Define

$$\omega_1 = Ry(1 - 1/9) = 8\ Ry/9$$

$$\omega_2 = Ry(1/4 - 1/16) = 3\ Ry/16 \qquad \text{(C-4b)}$$

$$N>2: \quad \omega_N = Ry\ [N^{-2} - (N + 1)^{-2}]$$

Then the A_N are:

$$N = 1: \quad A_1 = 0 \quad \text{if } \omega \leq \omega_1$$
$$= 6.34 \times 10^{-18} (Ry/\omega)^{8/3} \quad \text{if } \omega > \omega_1 \qquad \text{(C-4c)}$$

$$N \quad 1: \quad A_N = 0 \quad \text{if } \omega \leq \omega_N$$
$$= 7.9 \times 10^{-18} \left(\frac{Ry}{N\omega}\right)^3 \exp\left[-\frac{h_p c\ Ry}{kT}\left(1 - \frac{1}{N^2}\right)\right] \quad \omega > \omega_N \qquad \text{(C-4d)}$$

To complete the model, we need a treatment of the Ly_α and H_α lines. These lines arise from the transitions n = 1 to n' = 2 and n = 2 to n' = 3, respectively. The line centers are at $\omega_{nn'}$, given by

$$\omega_{12} = Ry(1 - 1/4) = 3Ry/4, \quad \omega_{23} = Ry(1/4 - 1/9) = 5Ry/36$$

which, we may note, are values missing from the sequence in Eq. (C-4b), which have the n = 1, n' = 3 and n = 2, n' = 4 transitions. The corresponding $f_{nn'}$ numbers are

$$f_{12} = 0.4162, \qquad f_{23} = 0.641$$

We first find the absorption coefficient integrated over the line width as

$$\int k_\omega d\omega = \left(\frac{\pi e^2}{m_E c^2}\right) f_{nn'} n_{AG} \left[1 - \exp\left(-\frac{h_p c\, \omega_{nn'}}{kT}\right)\right] \left\{ \begin{array}{l} 1 \\ 4 \exp\left(-\dfrac{h_p c\ Ry}{kT}\ \dfrac{3}{4}\right) \end{array} \right.$$

where the upper and lower factors in { } are for Ly_α and H_α, respectively. Here e is the electronic charge, m_E the electron mass and n_{AG} is the number density of atoms in the ground state. The latter is the lower state for the Ly_α line. The lower state for the H_α line is the n = 2 state, which requires for its number density the added factor $2^2 \exp [- h_p c\ Ry/kT(1 - 2^{-2})]$ which explains the factor in { } for H_α. In terms of the hydrogen atom number density n_H we have $n_{AG} = 2n_A/Q_{el H}$, where $Q_{el H}$ is the electronic partition function for H, already given in Eq. (C-3). Using this expression for n_{AG} and evaluating the constant, we find in cgs units

$$\int k_\omega d\omega = \frac{2 \times 8.85 \times 10^{-13} f_{nn'} n_H}{Q_{el H}} \left[1 - \exp\left(-\frac{h_p c\, \omega_{nn'}}{kT}\right)\right] \left\{ \begin{array}{l} 1 \\ 4 \exp\left(-\dfrac{3}{4}\dfrac{h_p c\ Ry}{kT}\right) \end{array} \right. \quad \text{(C-5)}$$

We now evaluate the continuum absorption coefficient at the line center, say $k_{cont}(\omega_{nn'})$, by the formulas given for hydrogen in Chapter III of Ref. C-1. Let the gas sample length we are interested in be L. If $k_{cont}(\omega_{nn'})L > 1$, the continuum contribution to emissivity is already near the black body limit and the addition of the line contribution to the absorption coefficient does not increase the emissivity significantly; therefore the line contribution can be neglected.

If $k_{cont}(\omega_{nn'})L < 1$, we then proceed to find the line contribution. One possible value of emissivity for the line is

$$\varepsilon^{(1)} = B(\omega_{nn'}) \; L \int k_\omega d\omega / \sigma T^4 \qquad \text{(C-6)}$$

where σ is the Stefan-Boltzmann constant, $B(\omega)$ is the black body function

$$B(\omega) = \frac{2\pi h_p c^2 \; \omega^3}{\exp(h_p c \; \omega/kT) - 1}$$

and the integral of the absorption coefficient is given in Eq. (C-5). This value is appropriate if the line is transparent, i.e., if the emissivity at the line center is not limited by reabsorption. The transparent approximation is used whenever $[k_\omega(\omega_{nn'}) + k_{cont}(\omega_{nn'})]L < 1$.

If the line center is reabsorbed, the line emissivity can be approximated by using the transparent emissivity in the spectral region where $[k_{cont}(\omega_{nn'}) + k_\omega]L < 1$, and the black body limit in the spectral region about the line center where $[k_{cont}(\omega_{nn'}) + k_\omega]L > 1$. This second possible emissivity is obtained using a line width

$$\Delta\omega_B = 2\alpha_T \; \omega_{nn'}^2 \; F_o$$

where (in cgs and statcoulombs)

$$F_o = (4\pi n_E/3)^{2/3} e = 1.248 \times 10^{-9} \; n_E^{2/3}$$

and α_T is found from

$$\alpha_T = \left\{ \frac{2 \; C_{nn'} \int k_\omega d\omega}{\omega_{nn'}^2 \; F_o \left[L^{-1} - k_{cont}(\omega_{nn'}) \right]} \right\}^{2/5}$$

The constants $C_{nn'}$ for the two lines are

$$C_{12} = 3.4 \times 10^{-18}, \qquad C_{23} = 1.3 \times 10^{-15}$$

in consistent units. Then the second emissivity is

$$\varepsilon^{(2)} = \frac{B(\omega_{nn'})\,\Delta\omega_B}{\sigma\, T^4} + \frac{8}{3}\,\frac{C_{nn'}\,\varepsilon^{(1)}}{(\alpha_T)^{3/2}} \qquad \text{(C-7)}$$

where the first term represents the contribution of the black-line center and the second term is the contribution from the transparent line wings.

The emissivity contribution of each line (Ly_α, n = 1, n' = 2 and H_α, n = 2, n' = 3) is given by the smaller of $\varepsilon^{(1)}$ and $\varepsilon^{(2)}$ for the line. This is added to the continuum contribution to ε, which is

$$\varepsilon_{cont} = \int \frac{B(\omega)}{\sigma\, T^4}\,(1 - e^{-kL})\, d\omega \qquad \text{(C-8)}$$

where k is the sum of the contributions discussed in Ref. C-1, Chapter III for hydrogen species, but the free-bound absorption coefficient of hydrogen atoms given there is to be replaced by that given in this Appendix, Eqs. (C-1) - (C-4). To avoid counting the continuum twice in the spectral region where the line center is reabsorbed, we subtract from the ε for the lines the value of the integrand of (C-8) at $\omega_{nn'}$, times $\Delta\omega_B$.

The emissivities that result from this model are displayed in Table C-1 for T = 10^4, 2 x 10^4 and 3 x 10^4 K, p = 1, 10 and 100 atm, and path lengths of 1, 10 and 100 cm. The increases with pressure and path length at a fixed temperature is shown clearly. The values cover a large range, from 10^{-3} to 1.

A previous calculation of the emissivity for high temperature hydrogen has been published in Ref. C-4, for 10^4 and 2 x 10^4 K, with 1 cm at 1 and 10 atm, and 10 cm at 1 atm. The values of emissivity given there are about a factor of 2 higher than the ones we have calculated. However, our description of the line shapes is more modern than that of Ref. C-4, which probably accounts for the differences.

TABLE C-1

EMISSIVITY OF HIGH TEMPERATURE HYDROGEN

$T(10^3\ K)$	ℓ = 1 cm	ℓ = 10 cm	ℓ = 100 cm
p = 1 atm			
10	1.27×10^{-3}	5.57×10^{-3}	3.74×10^{-2}
20	8.94×10^{-3}	5.67×10^{-2}	1.84×10^{-1}
30	7.31×10^{-4}	5.63×10^{-3}	4.62×10^{-2}
p = 10 atm			
10	8.81×10^{-3}	6.03×10^{-2}	4.12×10^{-1}
20	1.71×10^{-1}	5.00×10^{-1}	9.94×10^{-1}
30	4.90×10^{-2}	2.80×10^{-1}	6.46×10^{-1}
p = 100 atm			
10	1.21×10^{-1}	6.75×10^{-1}	1.03
20	8.46×10^{-1}	9.86×10^{-1}	1.00
30	6.67×10^{-1}	9.32×10^{-1}	9.86×10^{-1}

REFERENCES FOR APPENDIX C

C-1 Kemp, N.H. and Lewis, P.F., "Laser-Heated Thruster Interim Report, Contract NAS8-33097 (PSI TR-205), Woburn, MA, February 1980.

C-2 Kemp, N.H. and Root, R.G., "Analytical Studies of Laser Supported Combustion Waves in Hydrogen," NASA CR-135349 (PSI TR-97), Woburn, MA, August 1977.

C-3 Kemp, N.H., Root, R.G., Wu, P.K.S., Caledonia, G.E., and Pirri, A.N., "Laser-Heated Rocket Studies," NASA CR-135127 (PSI TR-53), Woburn, MA, May 1976.

C-4 Lasher, L.E., Wilson, K.H. and Grief, R., "Radiation from an Isothermal Hydrogen Plasma at Temperatures up to 40000 K," J. Quant. Spec. Rad. Trans., Vol. 7, 1967, pp. 305-322.

APPENDIX D

RADIATION FROM A CYLINDER

The simple thruster models described in Appendices A and B require an approximate expression for the radiation from a cylinder of gas at uniform temperature and pressure. The purpose of this Appendix is to derive the expression used in those models.

Consider a surface enclosing a uniform body of gas. The radiative flux normal to the surface at any point of the surface is made up of the contributions of all the rays which can reach that point from within the gas. Let each such ray be identified by angular coordinates θ, ϕ, where θ is the angle the ray makes with the inward normal, and ϕ is the azimuth angle around the normal. Let $\ell(\theta,\phi)$ be the length of the ray, from the surface point to the place where it pierces the surface again on the other side of the body. The radiative flux normal to the surface, at frequency ν, (and wave number $\omega=\nu/c$) is expressed by an integral over all such rays, as

$$S_\omega = \frac{B_\omega}{\pi} \int_0^{2\pi} d\phi \int_0^{\pi/2} d\theta \, \sin\theta \, \cos\theta \left[1 - \varepsilon^{-k_\omega \ell(\theta,\phi)} \right] \tag{D-1}$$

where k_ω is the absorption coefficient at ω, B_ω is the black body spectral flux

$$B_\omega = \frac{2\pi h_p c^2 \omega^3}{\exp(h_p c\omega/kT) - 1} \tag{D-2}$$

and h_p, k are the Planck and Boltzmann constants respectively.

To find the power radiated from the whole body at wave number ω we must integrate over the whole surface

$$Q_{R\omega_{tot}} = \int_{A_{tot}} S_\omega \, dA \tag{D-3}$$

and similarly, to find the power radiated from any portion of the surface we perform the integral over that portion.

Finally, to find the total power, we must integrate over ω

$$Q_{R_{tot}} = \int_0^\infty d\omega \, Q_{r_{tot\omega}} \tag{D-4}$$

and similarly for any portion of the surface.

It is thus apparent that for a uniform body of gas, the calculation of the radiation can be thought of in two parts. One is the geometric problem of calculating the integrals (D-1) and (D-3). The other is the physics problem of defining k_ω as a function of gas composition, pressure and temperature, and integrating over ω. These two parts can be treated independently. In the present work the integral over ω is performed numerically, once k_ω is determined. The present Appendix is devoted to the geometrical problem.

The integral in Eq. (D-1) is not expressible in closed form for most bodies, but can be performed for some simple shapes. For a plain infinite slab of thickness d, the classical result is

$$\frac{S_\omega}{B_\omega} = 1 - 2E_3(k_\omega d), \quad E_3(x) = \int_1^\infty e^{-tx} \frac{dt}{t^3} \tag{D-5}$$

For a sphere of radius R we easily find

$$\frac{S_\omega}{B_\omega} = 1 + \frac{2e^{-2a}}{2a} - \frac{2(1-e^{-2a})}{4a^2}, \quad a = k_\omega R \tag{D-6}$$

For an infinite cylinder, the result has recently been given (Ref. D-1) in terms of modified Bessel functions as

$$\frac{S_\omega}{B_\omega} = \frac{4a^2}{3}\left\{2\left[aK_1(a)I_1(a) + aK_0(a)I_0(a) - 1\right] + K_1(a)I_1(a)/a + K_1(a)I_0(a) - K_0(a)I_1(a)\right\} \tag{D-7}$$

All these results are, of course, independent of position on the surface, because of symmetry, so surface integration is simple.

We are here interested in a finite cylinder of radius R and length L, for which Eq. (D-1) cannot be integrated in terms of known functions. We will therefore consider an approximate expression.

The limiting forms of Eq. (D-1) for very large and very small $k_\omega \ell$ are called the black and transparent limits. The former is obtained by letting the exponential vanish, whence we find

$$S_{\omega B} = B_\omega \tag{D-8}$$

as we expect. The transparent limit is the first term of the expansion of the exponential, leading to

$$S_{\omega T} = \frac{k_\omega B_\omega}{\pi} \int_0^{2\pi} d\phi \int_0^{2\pi} d\theta \, \sin\theta \cos\theta \, \ell(\theta,\phi) = k_\omega B_\omega \ell_0 \tag{D-9}$$

The coefficient of $k_\omega B_\omega$ is called the geometrical mean beam length ℓ_0,

$$\ell_0 = \frac{1}{\pi} \int_0^{2\pi} d\phi \int_0^{2\pi} d\theta \, \sin\theta \cos\theta \, \ell(\theta,\phi) \tag{D-10}$$

A frequently used approximation for gas radiation is

$$S_\omega = B_\omega (1 - e^{-k_\omega \ell_0}) \tag{D-11}$$

This expression has the correct value in both the black and transparent limits, Eqs. (D-8) and (D-9) respectively, and is often used as an approximation over the whole range of $k_\omega \ell_0$.

Some idea of its accuracy can be obtained by applying this idea to the exact expressions for the slab, sphere and cylinder. The values of ℓ_0, obtained from $k_\omega d$ or $k_\omega R \to 0$ in Eqs. (D-5, D-6 and D-7), are 2d, 4R/3 and 2R respectively. These are then substituted into Eq. (D-11), and the results compared with exact evaluations of Eqs. (D-5, D-6 and D-7). (Tables of E_3 and the Bessel functions are available for these evaluations.) Such a calculation shows that the maximum

error for the slab is 13.5% at $k_\omega d = 0.5$, for the sphere it is 5.2% at $k_\omega R = 1.5$, and for the cylinder it is 6.4% at $k_\omega R = 0.8$. Thus the use of the approximation (D-11) is quite reasonable for these cases.

In the same spirit one can integrate Eq. (D-10) over the surface area of interest to obtain what we can call an area-averaged geometric mean beam length.

$$\bar{\ell}_0 = \frac{1}{A}\int_A \ell_0 \, dA \tag{D-12}$$

The limiting radiated powers are then the black value

$$Q_{R\omega B} = AB_\omega \tag{D-13}$$

and the transparent value

$$Q_{R\omega T} = k_\omega B_\omega A\bar{\ell}_0 \tag{D-14}$$

We can then propose an approximation for the radiated power, in analogy to Eq. (D-11), as

$$Q_{R\omega} = Q_{R\omega B}\,(1 - e^{-k_\omega \bar{\ell}_0}) \tag{D-15}$$

This again has the correct black and transparent limits, and can be thought of as a possible approximation over the whole range of $k_\omega \bar{\ell}_0$.

Checking the validity of this approximation is not so simple as for Eq. (D-11). We cannot use the slab, sphere and cylinder, since their values of ℓ_0 do not vary over the surface, so Eq. (D-15) reduces to Eq. (D-11) times A. A check is possible in a fairly simple way for the case of the base of a semi-infinite cylinder, for which it can be shown that the exact expression is

$$Q_{R\omega} = \pi R^2 B_\omega\left[1 - \frac{8}{\pi}\int_0^{\pi/2} d\theta \, \sin^2\theta \, E_3(2k_\omega R\cos\theta)\right] \tag{D-16a}$$

The expression obtained for ℓ_0 is $16R/3\pi$ so the approximation is

$$Q_{R_\omega} = \pi R^2 B_\omega \left(1 - e^{-k_\omega 16R/3\pi}\right) \qquad \text{(D-16b)}$$

A numerical integration of Eq. (D-16a) shows that Eq. (D-16b) has a maximum error of 27.5% of $k_\omega R = 1$. This gives us some confidence in using Eq. (D-15). Certainly other checks would be desirable, but we know of no other exact expressions which have been evaluated. Such evaluations would be very helpful.

It is felt that present evidence shows Eq. (D-15) to be sufficiently accurate for use in simple models such as those described in Appendices A and B. We will therefore proceed to apply Eq. (D-15) to a finite cylinder.

If one is interested in the radiated power emitted over the whole surface enclosing the volume, with area A_{tot}, it is not necessary to perform any integrations to obtain the limiting values. The black limit is, of course,

$$Q_{R\omega B_{tot}} = A_{tot} B_\omega \qquad \text{(D-17)}$$

The transparent limit is easily found, because there is no absorption, so the radiation from each volume element is emitted. In any one direction a volume element dV radiates $k_\omega B_\omega \, dV/\pi$ per steradian, or $4k_\omega B_\omega \, dV$ in all directions. Then the total transparent radiated power out of a volume V is

$$Q_{R\omega T_{tot}} = 4k_\omega B_\omega V \qquad \text{(D-18)}$$

This must agree with the integral of Eq. (D-9) over the total surface area, which means that

$$\int_{A_{tot}} \epsilon_0 \, dA = 4V = \bar{\epsilon}_{0_{tot}} A_{tot} \qquad \text{(D-19)}$$

That this is correct can be checked for the slab, sphere and cylinder, where ℓ_0 is 2d, 4R/3 and 2R, independent of location on the surface. The corresponding

areas are $2A$, $4\pi R^2$ and $2\pi RL$ and volumes are Ad; $4\pi R^3/3$ and $\pi R^2 L$, where A is the area of one face of the slab. Thus in all three cases $\ell_0 A_{tot} = 4V$, in accord with Eq. (D-19).

We turn now to the calculation of $\bar{\ell}_0$ for the side surface of a finite cylinder of radius R and length L, which is needed for the simple models of Appendices A and B. Consider first the mid-point of the side. Recall that θ is the angle a ray makes with the inner normal from the mid-point, and ϕ is the azimuth angle around that normal. We choose $\phi = 0$ in a cross-sectional plane. Then a ray from the mid-point of the side in any direction θ, ϕ, which hits the <u>side</u> of the cylinder has length

$$\ell_s = 2R \cos\theta/(\cos^2\theta + \sin^2\theta \cos^2\phi) \qquad \text{(D-20)}$$

A ray which hits the <u>end</u> of the cylinder, where ϕ is between 0 and π, has length

$$\ell_e = L/2 \sin\theta \sin\phi \quad . \qquad \text{(D-21)}$$

Because of symmetry we need only consider ϕ in the range of $0 \leq \phi \leq \pi/2$, and then quadruple the result. Of course, θ only varies between $0 \leq \theta \leq \pi/2$. The dividing line between where we have to use ℓ_s and where we must use ℓ_e is obtained by setting $\ell_s = \ell_e$. This is the equation of the circular perimeter of the base in θ, ϕ:

$$2R \cos\theta \sin\theta \sin\phi_d = (\cos^2\theta + \sin^2\theta \cos^2\phi_d)\, L/2. \qquad \text{(D-22)}$$

We can now express ℓ_0 from Eq. (D-10) as

$$\ell_0 = \frac{4}{\pi} \int_0^{\pi/2} d\phi \left[\int_0^{\phi_d} d\theta \sin\theta \cos\theta \, \ell_s + \int_{\phi_d}^{\pi/2} d\theta \sin\theta \cos\theta \, \ell_e \right] \qquad \text{(D-23)}$$

where $\phi_d(\theta)$ is defined by Eq. (D-22).

In these variables the integration is very difficult because of the complicated dependence of ℓ_s and ℓ_e on ϕ and θ, as well as the complicated form of $\phi_d(\theta)$. However, there is a set of angles which makes these expressions much simpler

Let $\pi/2 - \alpha$ be the angle between the ray θ, ϕ and the generator of the cylinder through the mid-point. Project the ray on the cross-sectional plane, giving a projection of length $\ell \cos \alpha$. Then introduce the angle between this projection and the inner normal from the side mid-point as β. These angles are related to θ, ϕ by

$$\cos\theta = \cos\alpha \cos\beta \ , \quad \sin\alpha = \sin\phi \sin\theta \tag{D-24}$$

and ℓ_s, ℓ_e take the simpler forms

$$\ell_s = 2R \cos\beta/\cos\alpha \ , \quad \ell_e = L/2\sin\alpha \tag{D-25}$$

The relation between θ and ϕ on the perimeter of the cylinder end, Eq. (D-22) becomes

$$\tan\alpha_d = L/4R \cos\beta \tag{D-26}$$

Finally, to transform the integral (D-23) we need the Jacobian determinant

$$J = \begin{bmatrix} \partial\theta/\partial\alpha & \partial\theta/\partial\beta \\ \partial\phi/\partial\alpha & \partial\phi/\partial\beta \end{bmatrix}$$

to express $d\theta d\phi = |J| \, d\alpha d\beta$. The algebra is lengthy but straightforward, and we find

$$\sin\theta \cos\theta \, d\theta d\phi = \cos^2\alpha \cos\beta \, d\alpha d\beta \ .$$

The limits on β are from 0 to $\pi/2$. The limits on α are from α_d to $\pi/2$ for the rays which hit the end, and 0 to α_d for the rays which hit the side, where $\alpha_d(\beta)$ is given by Eq. (D-26).

The expression for ℓ_0, Eq. (D-23), then becomes

$$\ell_0 = \frac{8R}{\pi}\int_0^{\pi/2} d\beta\ \cos\beta \int_0^{\alpha_d} d\alpha\ \frac{\cos^2\alpha\ \cos\beta}{\cos\alpha}$$

$$+ \frac{2L}{\pi}\int_0^{\pi/2} d\beta\ \cos\beta \int_{\alpha_d}^{\pi/2} d\alpha\ \frac{\cos^2\alpha}{\sin\alpha}$$

The first integral on α is easy. The second can be broken into two parts by using $\cos^2\alpha = 1 - \sin^2\alpha$, and the second part can also be integrated. The result is

$$\ell_0 = \frac{2}{\pi}\int_0^{\pi/2} d\beta\ \cos\beta\left[4R\ \cos\beta\ \sin\alpha_d - L\ \cos\alpha_d\right]$$

$$+ \frac{2L}{\pi}\int_0^{\pi/2} d\beta\ \cos\beta \int_0^{\pi/2} d\alpha/\sin\alpha$$

But the term in square brackets vanishes because of the definition of α_d from Eq. (D-26), leaving only the last double integral. This integral can be integrated by parts on β to give

$$\ell_0 = \frac{2L}{\pi}\left[\sin\beta \int_{\alpha_d}^{\pi/2} \frac{d\alpha}{\sin\alpha}\Bigg|_0^{\pi/2} + \int_0^{\pi/2} d\beta\ \frac{\sin\beta}{\sin\alpha_d}\frac{d\alpha_d}{d\beta}\right]$$

The integrated part vanishes because $\alpha_d = \pi/2$ when $\beta = \pi/2$, as Eq. (D-26) shows. Also, from Eq. (D-26), we find that

$$\frac{1}{\sin\alpha_d} = \frac{4R}{L}\left[\left(\frac{L}{4R}\right)^2 + \cos^2\beta\right]^{1/2}, \quad \frac{d\alpha_d}{d\beta} = \frac{L}{4R}\ \frac{\sin\beta}{(L/4R)^2 + \cos^2\beta}$$

Finally, then, we have

$$\ell_0 = \frac{2L}{\pi}\int_0^{\pi/2} d\beta \frac{\sin^2\beta}{\left[(L/rR)^2 + \cos^2\beta\right]^{1/2}} \qquad \text{(D-27)}$$

This can be expressed in terms of complete elliptic integrals by writing the integrand as

$$\frac{1}{b_1}\frac{1 - 1 + b_1^2\sin^2\beta}{\left[1 - b_1^2\sin^2\beta\right]^{1/2}} \quad \text{where } b_1 = \left[\left(\frac{L}{4R}\right)^2 + 1\right]^{-1/2} \qquad \text{(D-28)}$$

Thus we have

$$\ell_0 = \frac{2L}{\pi b_1}\left[\int_0^{\pi/2} d\beta \frac{1}{(1 - b_1^2\sin^2\beta)^{1/2}} - \int_0^{\pi/2} d\beta(1 - b_1^2\sin^2\beta)^{1/2}\right]$$

$$= \frac{2L}{\pi b_1}\left[K(b_1) - E(b_1)\right] \qquad \text{(D-29)}$$

where the complete elliptic integrals are defined by Eq. (D-29). They are well-studied and well tabulated functions.

We have thus expressed the geometric mean beam length at the <u>center of the side</u> of a cylinder in terms of its radius R and length L. The transparent flux follows from Eqs. (D-9), and an approximation for the flux over the whole range from black to transparent is given by Eq. (D-11).

This expression can now be used to find the ℓ_0 <u>at any point</u> on the side of the cylinder. First we recognize that if we wish to find the flux at the end of the side of the cylinder, rather than the mid-point of the side, that flux is the same as half the flux from the mid-point of a cylinder twice as long. We merely replace L by 2L and divide by 2 in Eqs. (D-27, D-28 and D-29). The result is

$$\ell_0 = \frac{2L}{\pi}\int_0^{\pi/2} d\beta \frac{\sin^2\beta}{\left[(L/2R)^2 + \cos^2\beta\right]^{1/2}} = \frac{2L}{b\pi}\left[K(b) - E(b)\right]$$

$$b = \left[(L/2R)^2 + 1\right]^{-1/2} \tag{D-30}$$

Now consider any point a distance x from the mid-point of the cylinder. The flux is made up of contributions from the end of the side of two cylinders, one of length L/2 + x and the other of length L/2 - x.

$$\ell_0 = \frac{2}{\pi}\left[\left(\frac{L}{2} + x\right)\int_0^{\pi/2} d\beta \frac{\sin^2\beta}{\left[(L/2 + x)^2/4R^2 + \cos^2\beta\right]^{1/2}}\right.$$

$$\left. + \left(\frac{L}{2} - x\right)\int_0^{\pi/2} d\beta \frac{\sin^2\beta}{\left[(L/2 - x)^2/4R^2 + \cos^2\beta\right]^{1/2}}\right] \tag{D-31}$$

This can be used to express the flux at any point in terms of elliptic integrals, by writing it as

$$\ell_0 = \frac{2}{\pi}\left\{\frac{(L/2 + x)}{b_+}\left[K(b_+) - E(b_+)\right] + \frac{(L/2 - x)}{b_-}\left[K(b_-) - E(b_-)\right]\right\}$$

$$b_\pm = \left[(L/2 \pm x)^2/4R^2 + 1\right]^{-1/2} \tag{D-32}$$

The resulting transparent flux is given by Eq. (D-9), and the approximate flux at any k_ω by Eq. (D-11).

To find the power radiated out the whole side of the cylinder, whose area is $2\pi RL$, we use Eq. (D-12), where $dA = 2\pi R dx$. We thus need the integral

$$\bar{\ell}_0 = L^{-1}\int_{-L/2}^{L/2} \ell_0 dx$$

of ℓ_0 from Eq. (D-31). If we let $y = L/2 + x$ in the first integral and $y = L/2 - x$ in the second integral, they both become the same, and we find

$$\bar{\ell}_0 = \frac{4}{\pi 2}\int_0^{\pi/2} d\beta\, \sin^2\beta \int_0^{L} \frac{y\, dy}{\left[(y/2R)^2 + \cos^2\beta\right]^{1/2}}$$

If we now let $z = (y/2R)^2$, $dz = y\, dy/2R^2$, then

$$\bar{\ell}_0 = \frac{8R^2}{\pi L}\int_0^{\pi/2} d\beta\, \sin^2\beta \int_0^{L^2/4R^2} \frac{dz}{\left[z + \cos^2\beta\right]^{1/2}}$$

The z integral is simple, and we find

$$\bar{\ell}_0 = \frac{16R^2}{\pi L}\int_0^{\pi/2} d\beta\, \sin^2\beta \left[\left(L^2/4R^2 + \cos^2\beta\right)^{1/2} - \cos\beta\right]$$

The second term integrates to 1/3. The first can also be expressed as complete elliptic integrals, by replacing $\cos^2\beta$ by $1 - \sin^2\beta$ and introducing the parameter b already defined in Eq. (D-30). The integral is

$$\int_0^{\pi/2} d\beta\, b^{-1} \sin^2\beta\left[1 - b^2\sin^2\beta\right]^{1/2} = G(b)/3$$

$$G(b) = (1 - b^2)\, K(b) - (1 - 2b^2)\, E(b) \qquad \text{(D-33)}$$

The final form for the area-averaged geometric mean beam length for the side of the cylinder is then

$$\bar{\ell}_0 = \frac{16R^2}{3\pi L}\left[\frac{G(b)}{b^3} - 1\right], \quad b = \left[\left(\frac{L}{2R}\right)^2 + 1\right]^{-1/2} \qquad \text{(D-34)}$$

Again, the transparent radiated power from the side is found from Eq. (D-14) as

$$Q_{R\omega B} = 2\pi RLk_\omega B_\omega \bar{\ell}_0 \qquad \text{(D-35)}$$

while the black radiated power is from Eq. (D-13),

$$Q_{R\omega B} = 2\pi RLB_\omega \tag{D-36}$$

The approximate expression, Eq. (D-15), becomes

$$Q_{R\omega} = 2\pi RLB_\omega \left(1 - e^{-k_\omega \bar{\ell}_0}\right) \tag{D-37}$$

For the total surface of the cylinder, we can easily find $\bar{\ell}_{0_{tot}}$ from Eq. (D-19) as

$$\bar{\ell}_{0_{tot}} = 2R/(1 + R/L) \tag{D-38}$$

since the total area is $2\pi RL + 2\pi R^2$. The corresponding transparent and black radiated powers are

$$Q_{R\omega T_{tot}} = 4\pi R^2 L k_\omega B_\omega$$

and

$$Q_{R\omega B_{tot}} = 2\pi RL(1 + R/L)B_\omega$$

while the approximate form (D-15) is, with (D-38)

$$Q_{R\omega_{tot}} = 2\pi RL(1 + R/L)B_\omega\left[1 - \exp\left(\frac{-2Rk_\omega}{1 + R/2}\right)\right] \tag{D-39}$$

The use of Eq. (D-37) is still somewhat inconvenient because of the elliptic integrals in the expression for G contained in $\bar{\ell}_0$. Since the use of Eq. (D-37) is only approximate, some further simplification is justified. We note that the ratio of the total to side black power is just the area ratio $1 + R/L$, while for the transparent power this ratio is $2R/\ell_0$. A calculation of

$$\frac{\bar{\ell}_0}{2R} = \frac{8R}{3\pi R}\left[\frac{G(b)}{b^3} - 1\right]$$

shows that for $R/L \leq 1$, this function is within 5.2% of $(1 + R/L)^{-1}$, always lying above it. So a satisfactory approximation is

$$\frac{R}{L} \leq 1: \quad \bar{\ell}_o = \frac{2R}{1 + R/L} \quad , \tag{D-40}$$

Thus for cylinders longer than their radius, the ratio of total to side transparent radiation is also approximately the area ratio. (For $\geq R/L \leq 1$ the error is less than 3.2%.) This implies that the sideways power is much larger than the base power for such cylinders.

For $R/L > 1$, we can expand the elliptic integrals for b near 1, and find the series for G in the form

$$\frac{R}{L} > 1: \quad G = 0.75(1 - K_2)\left[1 - \frac{1}{2}(1 - K_2)\right] \ln\left[16/(1 - K_2)\right]$$
$$+ 1 - 2.25(1 - K_2) + 0.25(1 - K_2)^2 \tag{D-41}$$
$$K_2 = b^2 = \left[(L/2R)^2 + 1\right]^{-1}$$

This expression is accurate to 1%. (For $2R/L > 1$ it is accurate to 1.6%.)

We conclude that the expressions to be used in the simple models of laser heated thrusters described in Appendices A and B are Eq. (D-39) for the power radiated from all surfaces of the cylinder, and Eq. (D-37) for the power radiated from the side surface, with $\bar{\ell}_0$ given by Eq. (D-40) or (D-41).

REFERENCE FOR APPENDIX D

D-1 Heaslet, M.A. and Warming, R.F., "Theoretical Predictions of Radiative Transfer in a Homogeneous Cylindrical Medium," J. Quant. Spec. Rad. Trans., Vol. 6, 1966, pp. 751-774.

APPENDIX E

FLOW EQUATIONS FOR THRUST CHAMBER DESIGN COMPUTER PROGRAM

The laser-heated thrust chamber is represented by the axisymmetric flow flow of a gas which is in chemical equilibrium, is absorbing laser radiation, and has energy transport by convection, diffusion and radiation. A set of equations for this flow was presented in Section 5.1 of Ref. E-1. An alternate, and perhaps more convenient version of the energy equation will be presented here, and contrasted with the previous formulation.

We consider the flow in an axisymmetric channel, where axial gradients are small compared to radial gradients. This enables us to make the boundary layer approximation that the viscous transport terms need only include radial gradients, not axial ones. Let us denote the axial and radial coordinates by x, r and the corresponding velocity components by u, v. The mass conservation equation is then

$$\frac{\partial \rho u}{\partial x} + \frac{1}{r}\frac{\partial r \rho v}{\partial r} = 0 \qquad \text{(E-1a)}$$

The boundary layer approximation applied to the radial momentum equation shows that the pressure is constant over a cross-section, so that $p = p(x)$. Then the axial momentum conservation equation is

$$\rho u \frac{\partial u}{\partial x} + \rho v \frac{\partial u}{\partial r} = -\frac{dp}{dx} + \frac{1}{r}\frac{\partial}{\partial r}\left(r\mu \frac{\partial u}{\partial r}\right) \qquad \text{(E-1b)}$$

The energy conservation includes the convection of enthalpy, the radiation, the flow work, the viscous dissipation and the conduction and diffusion of energy. If h denotes enthalpy, and $\underline{S}$ the radiation energy flux vector, then the conservation of energy requires

$$\rho u \frac{\partial h}{\partial x} + \rho v \frac{\partial h}{\partial r} + \nabla \cdot \underline{S} = u \frac{dp}{dx} + \mu \left(\frac{\partial u}{\partial r}\right)^2 + \frac{1}{r} \frac{\partial}{\partial r} \left\{ r \left[\lambda_{Cf} \frac{\partial T}{\partial r} + \sum \rho D_i h_i \frac{\partial C_i}{\partial r} \right] \right\} \qquad \text{(E-1c)}$$

The conduction term involves the frozen conductivity λ_{Cf}, which includes the translational and internal contributions, but not the reaction contribution. It is the sum of the terms given in Eqs. (4-55a) and (4-55b) of Ref. E-1. The diffusion term is the summation involving the enthalpy per unit mass h_i of the i-th species, the diffusion coefficient D_i for that species, and the gradient of the corresponding mass fraction C_i. This form of the diffusion term is the simplified one usually used, where the species diffusion velocity has been expressed by Fick's law as $D_i \, \partial C_i/\partial r$, to avoid the considerable complications of multicomponent diffusion.

There are two ways to express the conduction and diffusion terms in terms of enthalpy. We start with the definition of the mixture enthalpy as

$$h = \Sigma h_i C_i$$

and differentiate to get

$$dh = \Sigma h_i \, dC_i + c_{pf} dT, \quad c_{pf} = \Sigma c_{pi} C_i, \quad c_{pi} = dh_i/dT \qquad \text{(E-2)}$$

Here we have recognized that for each species, h_i depends only on T, and its derivative is the species specific heat c_{pi}, while c_{pf} is the frozen specific heat of the mixture, being just the mass-weighted sum of the specific heats of the individual components.

One way to express the conduction-diffusion heat flux term to substitute from Eq. (E-2) for dT, and combine the dC_i term with the diffusion term. The result is

$$\lambda_{Cf} \frac{\partial T}{\partial r} + \Sigma \rho D_i h_i \frac{\partial C_i}{\partial r} = \frac{\lambda_{Cf}}{c_{pf}} \left[\frac{\partial h}{\partial r} + \Sigma (Le_i - 1) h_i \frac{\partial C_i}{\partial r} \right] \qquad (E-3)$$

where the species Lewis number Le_i is defined as

$$Le_i = \rho D_i c_{pf} / \lambda_{Cf}$$

This approach is suitable for chemical non-equilibrium flow, where the C_i are computed from chemical reaction equations. It also shows the simplification which occurs when $Le_i = 1$ and the mass fraction gradients vanish. This form of the conduction-diffusion term was used in the flow equations written in Section 5.1 of Ref. E-1.

A second form of the conduction-diffusion term can be used for chemical equilibrium flow, when C_i is a function of p and T. Then we may write Eq. (E-2) as

$$dh = \left[\Sigma h_i (dC_i/dT)_p + c_{pf} \right] dT + \Sigma h_i (\partial C_i/dp)_T dp$$

The first summation on the right is the reaction specific heat and the sum of the terms in square brackets is the equilibrium specific heat

$$c_{pe} = c_{pf} + \Sigma h_i (\partial C_i/\partial T)_p \qquad (E-4)$$

Then the enthalpy derivative is

$$dh = c_{pe}\, dT + \Sigma h_i (\partial C_i/\partial p)_T\, dp \qquad (E-5)$$

We similarly use

$$dC_i = (\partial C_i/\partial T)_p\, dT + (\partial C_i/\partial p)_T\, dp$$

in the diffusion term, so the conduction-diffusion term becomes

$$\lambda_{Cf} \frac{\partial T}{\partial r} + \Sigma \rho D_i h_i \frac{\partial C_i}{\partial r} =$$

$$\left[\lambda_{Cf} + \Sigma \rho D_i h_i \left(\frac{\partial C_i}{\partial T}\right)_p\right] \frac{\partial T}{\partial r} + \Sigma \rho D_i h_i \left(\frac{\partial C_i}{\partial p}\right)_T \frac{\partial p}{\partial r} \qquad \text{(E-6)}$$

The quantity in square brackets on the right is the equilibrium thermal conductivity

$$\lambda_{Ce} = \lambda_{Cf} + \Sigma \rho D_i h_i \left(\frac{\partial C_i}{\partial T}\right)_p \qquad \text{(E-7)}$$

which adds the reaction conductivity term to the frozen conductivity. The reaction conductivity is the expression in Eq. (4-55c) of Ref. E-1, and the λ_C discussed there is the equilibrium conductivity λ_{Ce}. If we now replace the temperature gradient in Eq. (E-6) by the enthalpy gradient from Eq. (E-5), we find

$$\lambda_{Cf} \frac{\partial T}{\partial r} + \Sigma \rho D_i h_i \frac{\partial C_i}{\partial r} =$$

$$\frac{\lambda_{Ce}}{c_{pe}} \left[\frac{\partial h}{\partial r} + \Sigma (Le_{ei} - 1)\, h_i \left(\frac{\partial C_i}{\partial p}\right)_T \frac{\partial p}{\partial r}\right]$$

The second term on the right involves an equilibrium Lewis number

$$Le_{ei} = \rho D_i c_{pe} / \lambda_{Ce}$$

but it also has a radial pressure gradient term, which we have taken to be small enough to ignore. Thus, by using the equilibrium formulation of λ_C and c_p, we can write the conduction-diffusion term simply as

$$\lambda_{Cf} \frac{\partial T}{\partial r} + \Sigma \rho D_i h_i \frac{\partial C_i}{\partial r} = \lambda_{Ce} \frac{\partial T}{\partial r} = \frac{\lambda_{Ce}}{c_{pe}} \frac{\partial h}{\partial r}$$

The energy conservation equation (E-1c) now becomes

$$\rho u \frac{\partial h}{\partial x} + \rho v \frac{\partial h}{\partial r} + \nabla \cdot \underline{S} = u \frac{dp}{dx} + \mu \left(\frac{\partial u}{\partial r}\right)^2 + \frac{1}{r} \frac{\partial}{\partial r} \left(r \frac{\lambda_{Ce}}{c_{pe}} \frac{\partial h}{\partial r} \right)$$

The laser energy flux term is split off from the radiation flux vector $\underline{S}$. We take a parallel beam with only an x component, which we call I. Then the laser provides a term $\partial I/\partial x$ on the left of the energy equation. However, the absorption equation for the laser energy is expressed in terms of a laser absorption coefficient k_L as

$$\partial I/\partial x = -k_L I$$

This shows that the laser can be looked upon as providing a heating term $k_L I$ on the right side of the energy equation. (We permit I to depend on both r and x, through the laser propagates only in the x direction.) The remaining part of the radiant energy flux is due to gas radiation transport, and we will denote it by $\underline{S}^R$. Then the energy equation is

$$\rho u \frac{\partial h}{\partial x} + \rho v \frac{\partial h}{\partial r} + \nabla \cdot \underline{S}^R = u \frac{dp}{dx} + \mu \left(\frac{\partial u}{\partial r}\right)^2 + k_L I + \frac{1}{r} \frac{\partial}{\partial r} \left(r \frac{\lambda_{Ce}}{c_{pe}} \frac{\partial h}{\partial r} \right) \quad \text{(E-8)}$$

This is the equilibrium form of the energy equation. If the first approach to the convection-diffusion term had been used, Eq. (E-3), the only difference would have been replacement of the last term by

$$\frac{1}{r} \frac{\partial}{\partial r} \left\{ r \frac{\lambda_{Cf}}{C_{pf}} \left[\frac{\partial h}{\partial r} + \Sigma \left(Le_i - 1 \right) h_i \frac{\partial C_i}{\partial r} \right] \right\} \quad \text{(E-9)}$$

This form was given in Eq. (5-1d) of Ref. E-1.

If $Le_i = 1$ for all species, the equations become the same, because it is easy to see that then $\lambda_{Cf}/c_{pf} = \lambda_{Ce}/c_{pe}$. Use of the equilibrium form Eq. (E-8) avoids the calculation of $\partial C_i/\partial r$ when the assumption $Le_i = 1$ is not warranted. This simplification is achieved at the expense of having to use λ_{Ce} instead of λ_{Cf}, which means including the reaction conductivity.

The present computer program uses the equilibrium formulation Eq. (E-8), and the subsequent transformations described in this appendix will use that equation also. The alternative formulation using Eq. (E-9) is given in Chapter V of Ref. E-1.

These conservation equations are singular on the axis $r = 0$, and must be expressed in limiting form there. On the axis, symmetry requires that $v = 0$ and $\partial u/\partial r = 0$. Near the axis these two quantities are proportional to r. All the terms with the operator $v\partial/\partial r$ vanish because v vanishes while $\partial/\partial r$ is finite. The only terms which must be looked at carefully are those with a $1/r$ factor. A typical one is the viscous term in the momentum equation (E-1b):

$$\frac{1}{r}\frac{\partial}{\partial r} r\mu \frac{\partial u}{\partial r} = \mu \frac{\partial^2 u}{\partial r^2} + \frac{\mu}{r}\frac{\partial u}{\partial r} + \frac{\partial \mu}{\partial r}\frac{\partial u}{\partial r}$$

The last term is of order r^2 and vanishes on the axis. The first term is finite, and the second term is the same as the first when a Taylor series expansion of $\partial u/\partial r$ is made. Thus on the axis

$$\left(\frac{1}{r}\frac{\partial}{\partial r} r\mu \frac{\partial u}{\partial r}\right)_a = 2\left(\mu \frac{\partial^2 u}{\partial r^2}\right)_a$$

Exactly similar treatment can be accorded the second term in Eq. (E-1a) and the last term in Eq. (E-8). The resulting equations on the axis are

$$\frac{\partial \rho u}{\partial x} + 2\rho \frac{\partial v}{\partial r} = 0 \qquad \text{(E-10a)}$$

$$u \frac{\partial u}{\partial x} = - \frac{dp}{dx} + 2\mu \frac{\partial^2 u}{\partial r^2} \qquad \text{(E-10b)}$$

$$\rho u \frac{\partial h}{\partial x} + \nabla \cdot \underline{S}^R = u \frac{dp}{dx} + k_L I + 2 \frac{\lambda_{Ce}}{c_{pe}} \frac{\partial^2 h}{\partial r^2} \qquad \text{(E-10c)}$$

The numerical solution of the flow equations is accomplished by using the stream function ψ as an independent variable. We define it as

$$\psi = \int_0^r \rho u r dr, \quad \frac{\partial \psi}{\partial r} = \rho u r, \quad \frac{\partial \psi}{\partial x} = -\rho v r$$

so the mass conservation equation is satisfied automatically. The stream function has the physical significance of being the mass flow through a cross-section of radius r, except for a factor of 2π. It replaces the variable r. The other independent variable is $\xi = x$, but is given a new name to avoid confusion in the transformation process. The transformation from x,r to ξ,ψ is given in Section 5.2 of Ref. E-1. The momentum and energy conservation equations (E-1b and E-8) become

$$\frac{\partial u}{\partial \xi} = - \frac{1}{\rho u} \frac{dp}{d\xi} + \frac{\partial}{\partial \psi} \left(\rho u r^2 \mu \frac{\partial u}{\partial \psi} \right) \qquad \text{(E-11a)}$$

$$\frac{\partial h}{\partial \xi} + \frac{\nabla \cdot \underline{S}}{\rho u} = \frac{1}{\rho} \frac{dp}{d\xi} + \frac{k_L I}{\rho u} + \rho u r^2 \mu \left(\frac{\partial u}{\partial \psi} \right)^2 + \frac{\partial}{\partial \psi} \left(\frac{\rho u r^2 \lambda_{Ce}}{c_{pe}} \frac{\partial h}{\partial \psi} \right) \qquad \text{(E-11b)}$$

The corresponding equations on the axis are found from Eqs. (E-10b and E-10c). The transformation on the axis is derived in Section 5.2 of Ref. E-1 and shows that $\partial^2/\partial r^2 \rightarrow \rho u \partial/\partial \psi$. Then the momentum and energy conservation equations <u>on the axis</u> are

$$\frac{\partial u}{\partial \xi} = - \frac{1}{\rho u} \frac{dp}{d\xi} + 2\mu \frac{\partial u}{\partial \psi} \qquad \text{(E-12a)}$$

$$\frac{\partial u}{\partial \xi} + \frac{\nabla \cdot \underline{S}}{\rho u} = \frac{1}{\rho}\frac{dp}{d\xi} + \frac{k_L I}{\rho u} + 2\frac{\lambda_{Ce}}{c_{pe}}\cdot\frac{\partial h}{\partial \psi} \qquad \text{(E-12b)}$$

The only other change to the flow equations given in Chapter V of Ref. E-1 is in calculating the heat flux to the wall arising from the convective and diffusive terms. The radial heat flux is the coefficient of r in the last term of Eq. (E-1c):

$$q_C = -\lambda_{Cf}\frac{\partial T}{\partial r} - \Sigma \rho D_i h_i \frac{\partial C_i}{\partial r}$$

The minus sign is needed so that negative radial gradients produce positive radial flux. The transformation to the equilibrium form leads to the form exhibited by the last term of Eq. (E-8):

$$q_C = -\frac{\lambda_{Ce}}{c_{pe}}\frac{\partial h}{\partial r} \qquad \text{(E-13)}$$

The further transformation to ψ as the independent variable produces

$$q_C = -\rho u r \frac{\lambda_{Ce}}{c_{pe}}\frac{\partial h}{\partial \psi} \qquad \text{(E-14)}$$

as in the last term of Eq. (E-11b). It is shown in Section 5.6 of Ref. E-1 how to evaluate this on the wall streamline where u = 0 but $\partial/\partial\psi$ is infinite. We convert $\partial/\partial r$ in Eq. (E-13) to $\partial/\partial r^2$ by multiplying by 2r. Then $\partial/\partial r^2$ is evaluated in finite difference form and related to a finite difference form in ψ. The result is

$$q_C = \frac{2r_w \lambda_{Cew}}{c_{pew}}\left[h_w - h\right]\frac{\rho u}{4(\psi_w - \psi)} \qquad \text{(E-15)}$$

where the quantities with subscript w are to be evaluated on the wall streamline and those without subscripts are to be evaluated at the first streamline away from the wall.

We note that if the wall streamline is at an angle to the x-axis, only the component of the radial flux q_c which is normal to the wall supplies heat to the wall.

In summary, the computer program solves Eqs. (E-11a and E-11b), except on the axis where Eqs. (E-12a and E-12b) are used. The conduction-diffusion heat flux to the wall is evaluated using Eq. (E-15). The change from the formulation given in Chapter V of Ref. E-1 is in the energy equation and q_c where λ_{Cf}/c_{pf} is replaced by λ_{Ce}/c_{pe}, and the $\partial C_i/\partial r$ term is omitted. The equilibrium thermal conductivity λ_{Ce} is defined in Eq. (E-7), and its calculation is discussed in Section 4.4 of Ref. E-1. The equilibrium specific heat c_{pe} is defined in Eqs. (E-2 and E-4). It is actually $(\partial h/\partial T)_p$ for a mixture which stays in chemical equilibrium, as shown by Eq. (E-5).

REFERENCE FOR APPENDIX E

E-1 Kemp, N.H. and Lewis, P.F., "Laser-Heated Thruster Interim Report," Contract NAS8-33097 (PSI TR-205), Woburn, MA, February 1980.

APPENDIX F

RADIATION MODEL FOR H_2/H_2O/Cs MIXTURES

A band model was constructed in the Interim Report, Ref. F-1, for the radiation from a specific mixture of hydrogen, water and cesium. The model has been modified to give reliable predictions of the radiation from mixtures subject to the following constraints: temperature $\leq$ 6000 K; pressure between three and one hundred atmospheres; radius between three and thirty centimeters; initial cesium molar concentration from .005 to .01; and initial water molar concentrations from .05 to .10.

The radiating species which were considered were H_2O, OH, Cs (bound-free transitions), H_2 (vibrational transitions), H(bound-free transition), H^-, and the free-free contributions from E-H, E-Cs, E-H^+ and E-Cs^+. Analysis of detailed calculations of both the absorption coefficient and the radiation emission coefficient indicated that the three bands defined in Ref. F-1 were adequate to describe the radiation for the range of parameters considered. The parameters used to describe the radiation in the three bands are described below.

$$\text{Band 3: } 2 \times 10^4 \text{ cm}^{-1} < \omega < \infty$$

The major contributions in this band are the free bound radiation involving H^- and the first excited state of Cs. The expression used in Ref. F-1 is still valid, that is

$$k_3^* = 1.0\text{E-}17\ n_{Cs}^* + 2.5\text{E-}17\ n_{HM} \qquad \text{(F-1)}$$

where n_{Cs}^* is the number density of the first two excited states of cesium and n_{HM} is the number density of H^-.

$$\text{Band 2: } 8000 \text{ cm}^{-1} < \omega < 2 \times 10^4 \text{ cm}^{-1} \qquad \text{(F-2)}$$

The major contributions in this band are the free bound radiation involving H^- and the intermediate excited states of Cs. The expressions

developed in Ref. F-1 remains valid, that is

$$k_2^* = 1.75E\text{-}17\ n_{Cs}^{**} + 4.2E\text{-}17\ n_{HM}$$

where n_{Cs}^{**} is the number density of the intermediate excited states of cesium.

Band 1: $0 < \omega < 8000\ cm^{-1}$

There are several important radiators in the low temperature band. In addition to bound-free radiation associated with highly excited states of Cs, there are contributions from Bremsstrahlung when an electron collides with Cs, H, H^+, Cs^+ and H_2, and also contributions from vibrational bands of H_2, OH and H_2O. The contribution of the cesium bound-free radiation and the Bremsstrahlung radiation are well represented by the following expression for the absorption coefficient

$$k_1^* = 1.3E\text{-}17\ n_{Cs}^{***} + \sum_i n_1 n_E \sigma_{Ei}(\omega = 4500\ cm^{-1}) \qquad \text{(F-3)}$$

In the above expression n_{Cs}^{***} is the number density of the highly excited states of cesium, n_E is the electron concentration, n_i is the concentration of species i and σ_{Ei} is the inverse Bremsstrahlung cross-section for collision between electrons and species 1 evaluated at $\omega = 4500\ cm^{-1}$.

The absorption coefficient for the vibrational transitions in H_2O, OH and H_2 varies rapidly as the wave number varies; thus these transitions are not amenable to accurate representation by a constant absorption coefficient. Fortunately, for the range of radius, pressure, temperature and composition considered here, these transitions can be well represented as a transparent contribution to the radiation. They are included in the radiation modeling as a contribution to $\nabla \cdot \underline{S}^R$, namely

$$(\nabla \cdot \underline{S}^R)_{thin} = 1.85E\text{-}21 T^{2.9} n_{H2O} + \frac{1.07E\text{-}36\ T^{0.6}}{e^{6043/T} - 1}$$

$$+ \frac{2.53E\text{-}11}{e^{5136/T} - 1}\ n_{OH} \qquad \text{(F-4)}$$

where n_{H_2O}, n_{H_2}, and n_{OH} are the number densities of H_2O, H_2 and OH respectively.

The band model calculations are compared to detailed calculations of the radiation parameters in Figs. F-1 - F-6. In Fig. F-1 the spectral absorption coefficient k_ω for 1 atm of Cs at 6000 K is shown for both models. The band model values are average values of k_ω throughout limited spectral ranges; however, the average values depart from the detailed values both at very low ω and at ω greater than 30000 cm^{-1}. In Fig. F-2 the normalized spectral emission coefficient is shown in both models. It is seen that the major contribution to the emission coefficient is well approximated, and the errors in k_ω at both small and large ω do not lead to errors in the spectrally integrated emission coefficient of more than 5 percent.

The absorption coefficient for one atmosphere of H_2 at 4000 K is shown in Fig. F-3 for both the detailed model and the band model. The band values are representative of average values except for $\omega > 30{,}000$ cm^{-1} and $\omega < 3{,}000$ cm^{-1}. The major contribution to the spectral emission coefficient is again well approximated; the error in the band model approximation for the integrated emission coefficient is 10 percent.

Finally, Fig. F-5 shows the detailed calculation of the absorption coefficient for vibrational transitions in one atmosphere water vapor at 2000 K. The rapid variation of the absorption coefficient cannot be well characterized by a single constant value from $\omega = 0$ to 8000 cm^{-1}, but the integral of the spectral emission coefficient, which is shown in Fig. F-6, is given by a term in Eq. F-4. This approximation is in error only when strong reabsorption occurs, which requires that the product of the partial pressure of H_2O and the radius be approximately 30. Only for the largest sizes and highest pressures considered does the transparent approximation fail, and even then the failure is limited to low temperature regimes where radiation losses are small.

Based on similar comparisons of the band model with detailed spectral calculations, it has been concluded that the band model approximates the important radiative losses within ten percent for the range of pressure, temperature, radius, and compositions of interest.

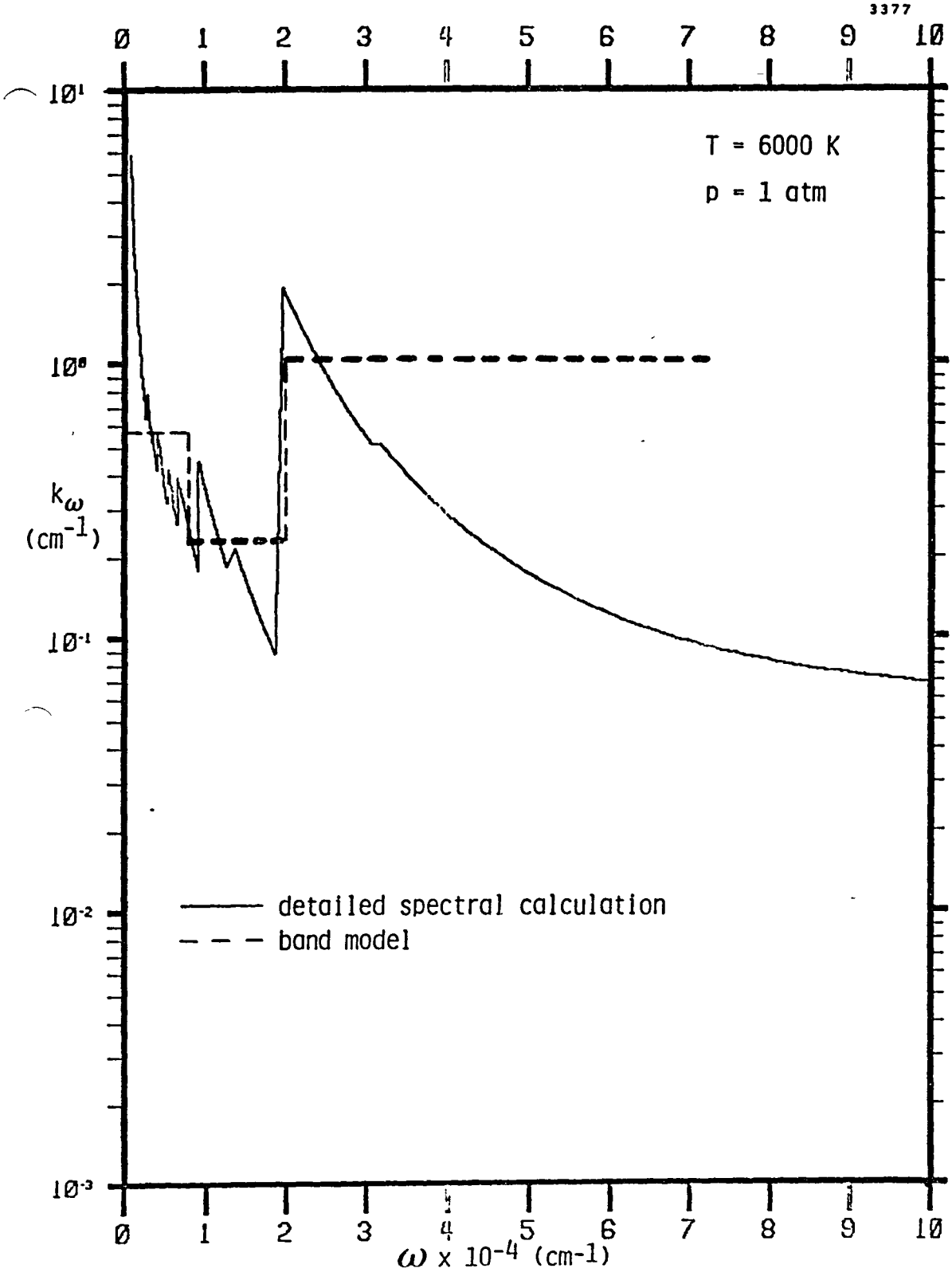

Figure F-1 Spectral absorption coefficient and band model approximation for Cesium.

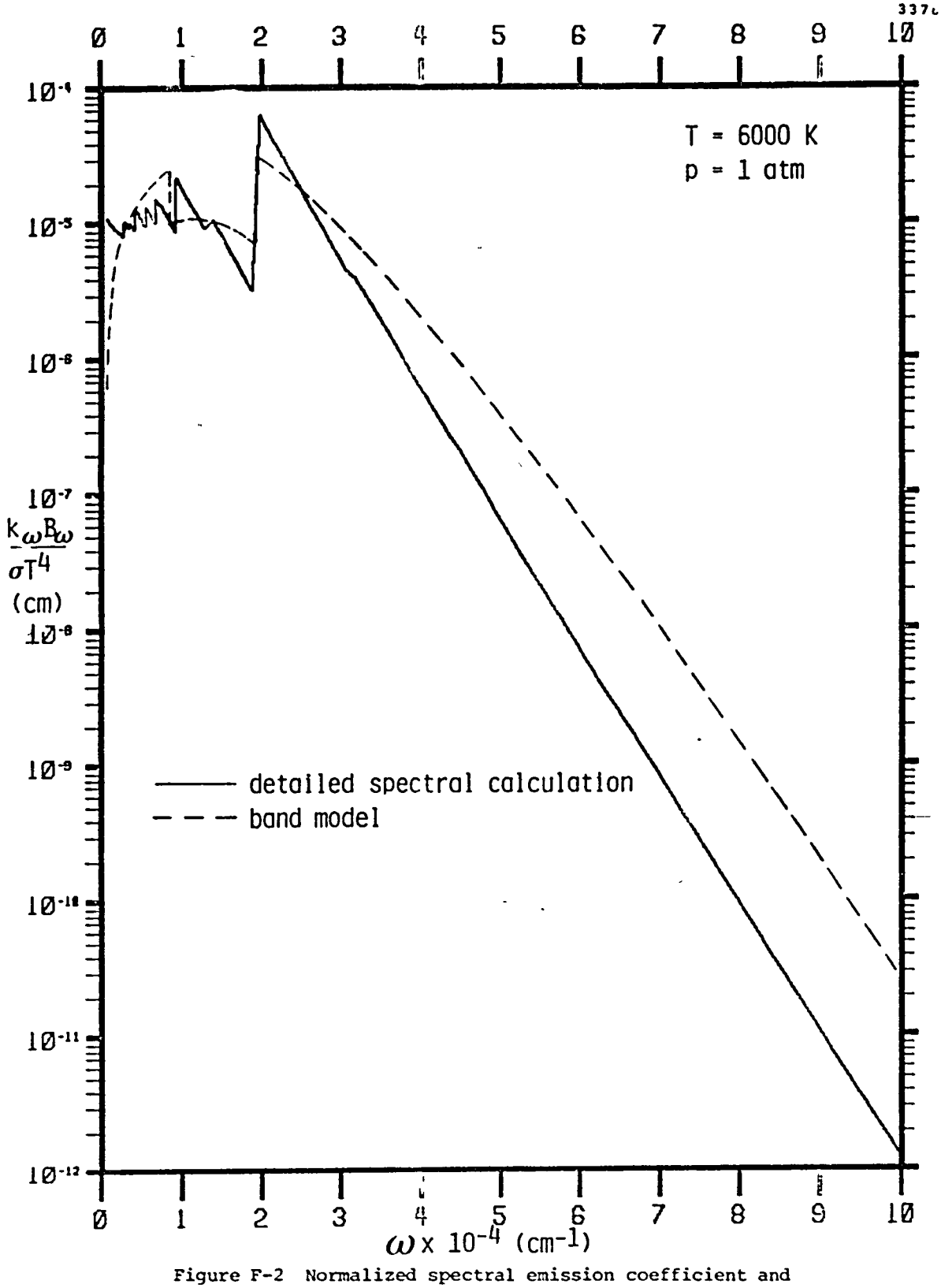

Figure F-2 Normalized spectral emission coefficient and band model approximation for cesium.

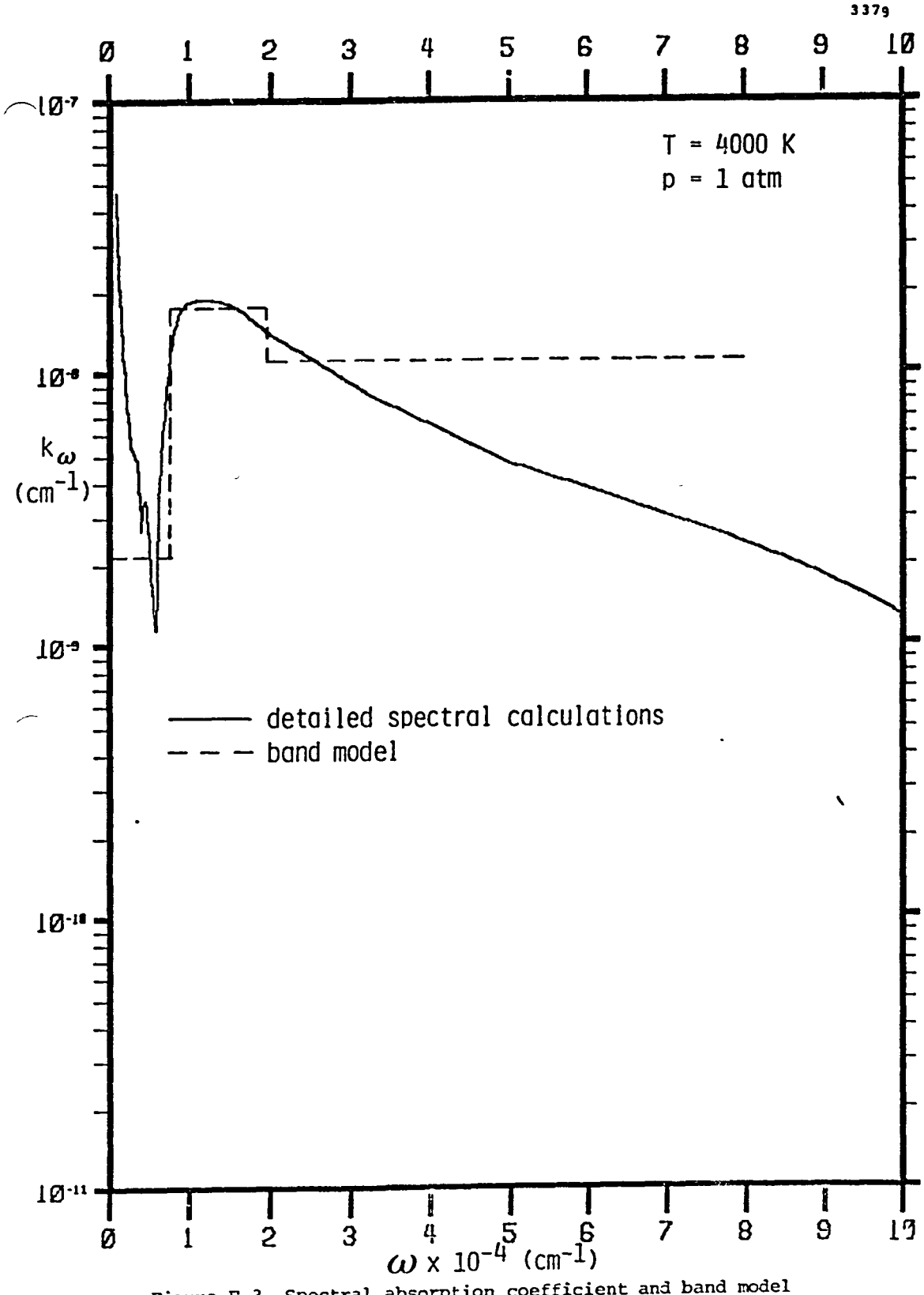

Figure F-3 Spectral absorption coefficient and band model approximation for hydrogen.

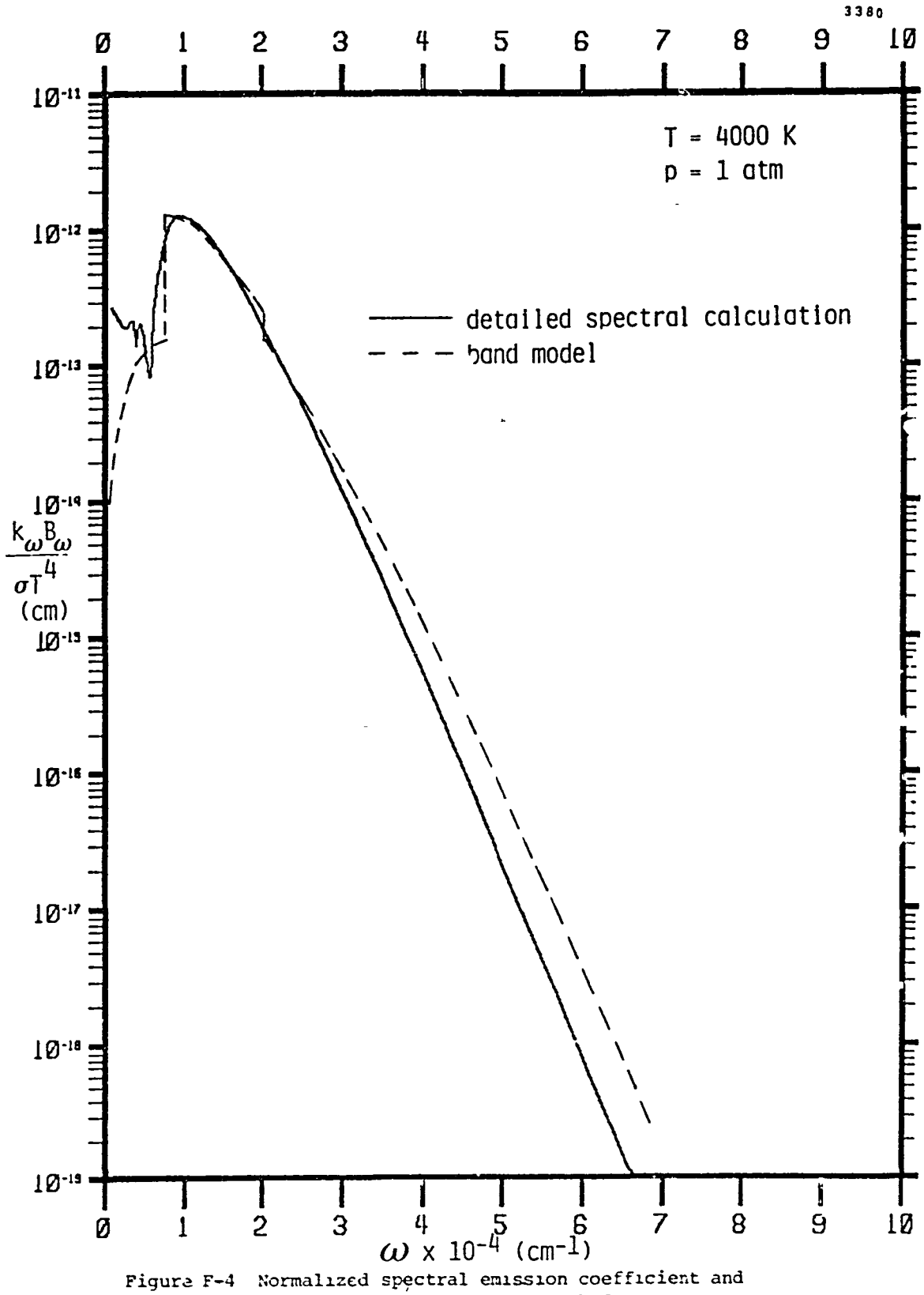

Figure F-4 Normalized spectral emission coefficient and band model approximation for hydrogen.

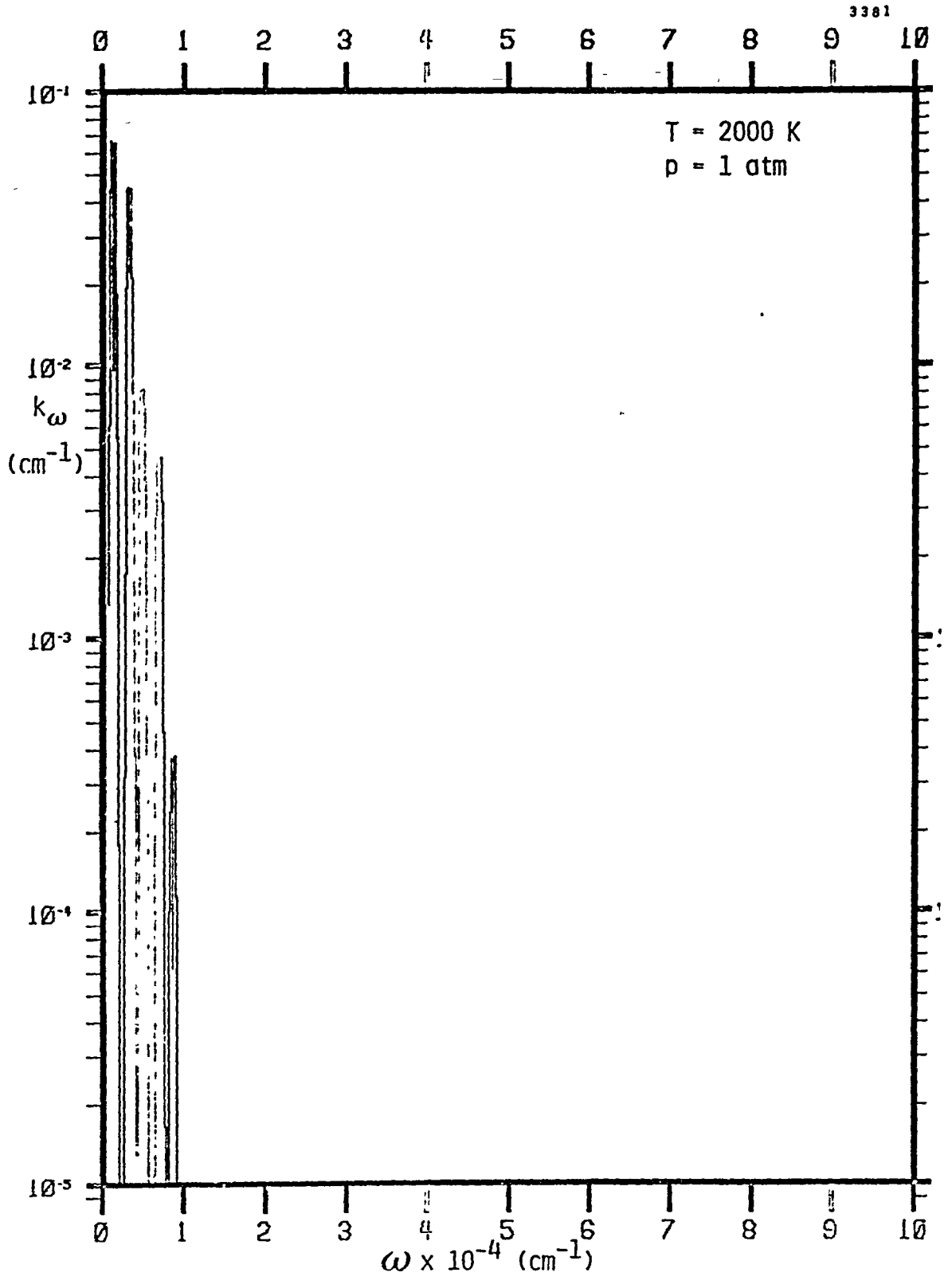

Figure F-5 Spectral absorption coefficient for water.

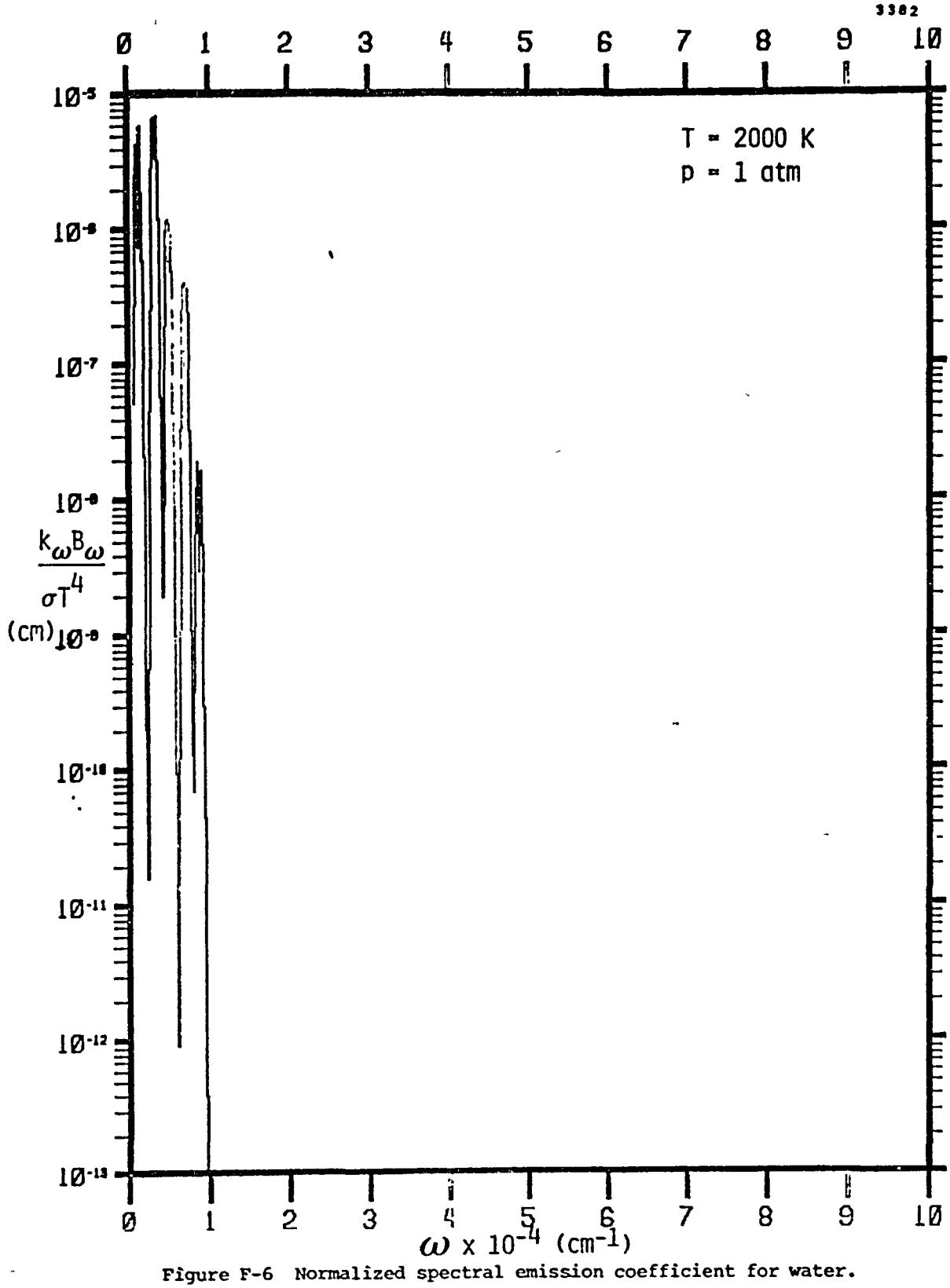

Figure F-6 Normalized spectral emission coefficient for water.

REFERENCE FOR APPENDIX F

F-1 Kemp, N.H. and Lewis, P.F., "Laser-Heated Thruster Interim Report," Contract NAS8-[illegible]37 (PSI TR-205) Woburn, MA, February 1980.

APPENDIX G

LASER SUPPORTED COMBUSTION WAVE MODEL

One method of coupling laser energy into a gas is by means of a laser supported combustion (LSC) wave. This is a mechanism which permits the absorption of laser energy in a flowing gas, to produce a high temperature flow. It is analagous to a deflagration wave in chemical combustion. The LSC wave consists of a constant pressure region in which the gas temperature rises sharply to a high value, and then decays slowly. The high temperature region is maintained by the absorption of laser energy, usually by inverse Bremsstrahlung absorption. The rapid temperature rise from the cold on-coming gas to the hot region is accomplished by the transport of energy from the hot region forward into the cold gas by both thermal conduction and radiation. The decay of the temperature at the back of the wave is caused by radiation losses dominating the absorption of laser energy, because the beam has already been almost completely absorbed.

A previous analytical study has been made of such waves in hydrogen, and the results have been reported in Ref. G-1. Presented there is a primarily one-dimensional model of the structure of such a wave, although the effect of beam convergence and some estimate of transverse energy losses were included.

In the present study, the model in Ref. G-1 was partially extended to include an equilibrium mixture of cesium and hydrogen. These extensions were incorporated into the computer program developed in the previous work, so that the structure of LSC waves in cesium-hydrogen mixtures can be calculated. This appendix gives a brief description of the model as it presently exists.

For an LSC wave, as for a deflagration wave, the momentum equation is satisfied by taking the pressure p to be constant. Conservation of mass in the one-dimensional flow requires

$$\rho u = \dot{m}_A = \text{constant} \qquad \text{(G-1)}$$

where ρ and u are the density and flow velocity. Conservation of energy is conveniently expressed by the use of the total enthalpy as

$$\dot{m}_A \frac{d}{dx}(h + u^2/2) + \frac{dI}{dx} + \nabla\cdot\underline{S}^R = \frac{d}{dx}\left(\lambda_{Ce}\frac{dT}{dx}\right) + \frac{C_{LC}}{R^2}\int_{300}^{T}\lambda_{Ce}dt \qquad \text{(G-2)}$$

Here h is the gas enthalpy, I the laser intensity, $\underline{S}^R$ the gas radiation energy flux, T the temperature, R the beam radius, and λ_{Ce} the equilibrium thermal conductivity of the gas, as defined in Appendix E. This equation expresses the balance of convection of total enthalpy, laser absorption, gas radiant energy flux, combined conduction-diffusion energy flux, and an estimate for transverse conduction losses.

The relation for the beam intensity is obtained by conserving the power in the beam. If the beam area is A_B then the power is IA_B, and conservation requires the decrease of power in the propagation direction x to equal the power absorbed with absorption coefficient k_L. Thus, we have

$$-dIA_B/dx = k_L IA_B \qquad \text{(G-3)}$$

whose solution is

$$IA_B = I_i A_{Bi}\, e^{-\tau},\ \tau = \int_0^x k_L\, dx \qquad \text{(G-4)}$$

where the subscript i refers to the location x = 0.

The energy equation (G-2) deals with the flow near the beam centerline where $dI/dx = -k_L I$. Use of Eq. (G-4) shows that

$$\frac{dI}{dx} = -k_L\, e^{-\tau}\ I_i \frac{A_{Bi}}{A_B} \qquad \text{(G-5)}$$

Thus, the laser absorption term depends not only on the absorption coefficient, but also on the beam shape $A_B(x)$.

In Ref. G-1, Section 4.2, an expression for the beam shape is obtained in terms of three physical parameters. One is the distance x_F from the beginning of the wave, $x = 0$, to the beam focal plane. The other two are the distance L from the focusing lens to the focal plane, and the size ω_L of the beam on the focusing lens. They appear only in the ratio L/ω_L, which is the f- number of the lens. The area ratio is given by

$$\frac{A_B}{A_{Bi}} = \frac{z_o^2 + (x-x_F)^2}{z_o^2 + x_F^2} \tag{G-6a}$$

where

$$z_o = \frac{\lambda_L}{\pi}\left(\frac{L}{\omega_L}\right)^2 \tag{G-6b}$$

and ω_L is the laser wavelength. Equations (G-5) and (G-6) serve to define the laser absorption term in the energy equation (G-2) in terms of the absorption coefficient k_L, the wave to focal plane distance x_F and the lens f- number L/ω_L.

The radiation term $\nabla\cdot\underline{S}^R$ must be specified in terms of the gas properties. The study for hydrogen radiation, made in Refs. G-1 and G-2, showed that there were two parts to the radiation transport. One was a volumetric loss term consisting of transparent radiation, P_T, and one a radiation transport term which can be modeled using the conduction approximation. Then the radiation term is expressed as

$$\Gamma_0\underline{S}^R = P_T - \frac{d}{dx}\left(\lambda_R \frac{dT}{dx}\right) - \frac{C_{LR}}{R^2}\int_{300}^{T} \lambda_R dT \tag{G-7}$$

A parametric expression for P_T was given in Appendix D of Ref. G for hydrogen as

$$P_T = 17.2 \times 10^{-9} \frac{C_3 T}{\theta_I} \left(\frac{T}{\theta_I} + C_2\right) \frac{n_A}{Q_{elA}} e^{-\theta_I/T} \qquad \text{(G-8)}$$

expressed in W/m^3. Here θ_I is the ionization energy for hydrogen, expressed in degrees K, n_A is the number density of hydrogen atoms in m^{-3} and Q_{elA} is the electronic partition function of these atoms

$$Q_{elA} = \sum_{j=1} 2\, j^2 \exp\left[-\theta_I (1-j^{-2})\ /T\right]$$

The constants C_3 and C_2 depend on gas pressure and laser power level, and have been worked out for 10 kW and 5MW lasers at 1,3,10 and 30 atm:

P(kW)	p(atm)	C_3	C_2
10	1,3	2	2.4
10	10,30	1.3	2.4
5000	1,3	2	0.4
5000	10,30	2.2	0.4

For the radiation conductivity λ_R, an expression was also given in Appendix D of Ref. G-1. It is expressed for hydrogen in terms of (in MKS units)

$$\lambda_{VUV} = \frac{0.775 \times 10^{30}}{T^2} \frac{Q_{elA}}{n_A} \frac{7!\, e^{-150{,}865/T}}{(11605/T)^8} \sum_{\ell=0}^{7} \frac{(150{,}865/T)}{\ell!} \qquad \text{(G-9a)}$$

$$k'_{VUV} = 12.68 \times 10^{-22}\, n_A/Q_{elA} \qquad \text{(G-9b)}$$

Then it was shown that

$$\lambda_R = \lambda_{VUV} \times \left\{\text{the smaller of 1 or } 2Rk'_{VUV}\right\} \qquad \text{(G-10a)}$$

is to be used in the derivative term of Eq. (G-7) and

$$\lambda_R = \lambda_{VUV} \qquad \text{(G-10b)}$$

is to be used in the integral term.

The constants C_{LC} in Eq. (G-2) and C_{LR} in Eq. (G-7) are coefficients which provide the strength of the transverse conduction losses. This form of transverse loss estimate was first proposed by Raizer in Ref. G-3, for ordinary conduction. He proposed the value 3 for the constant, which we have adapted for C_{LC}. For C_{LR} we have used 3 for a 5 MW laser and 0 for a 10 kW laser, where the size of the beam is quite small for the intensities of interest.

With the laser and gas properties so specified, the energy equation (G-2) can be integrated from x=0, at which we choose a temperature T_i low enough so no radiation losses can occur up to that temperature. A boundary condition there is obtained by equating the energy which has been added to the incoming gas to that which has been transported from the hot gas. This energy balance requires, with $(\ )_o$ the incoming gas state,

$$\dot{m}_A \left[h_1 - h_o + (u_1^2 - u_o^2)/2\right] = (\lambda_{Ce} + \lambda_R)_1 \, (dT/dx)_1 \qquad \text{(G-11)}$$

The equation of state for the gas is also used, relating p, ρ, T and h. Finally, the mass conservation equation (G-1) permits u to be eliminated in favor of ρ.

The integration of Eq. (G-2) requires a value for $\dot{m}_A$. This is a free parameter whose value must be chosen so that the integration produces a physically reasonable temperature profile. If $\dot{m}_A$ is too small, T will go

to zero after rising to a peak. If $\dot{m}_A$ is too large, T will climb continually without reaching a peak. For the correct solution, T rises to a peak, and then decays to a constant value. The procedure for finding the correct value of $\dot{m}_A$, by iterative integration of Eq. (G-2), is described in Ref. G-1.

The formulation as described above is also valid for a gas mixture, provided the gas properties and radiation and conduction loss coefficients are properly evaluated. For the cesium-hydrogen mixture of present interest, some of these properties have been evaluated, but not all. The equilibrium thermodynamic properties have been described in Chapter IV of Ref. G-1 and are incorporated in the present program. The equilibrium thermal conductivity was also considered in Chapter IV of Ref. G-1. There it was found that small amounts of cesium added to hydrogen ($C_S/H=0.01$) have a negligible effect on the thermal conductivity of the mixture, so that the values of λ_{Ce} appropriate for pure hydrogen may be used. They are given in Fig. 4-1 of Ref. G-1, and are incorporated in the present program both as λ_{Ce} and as $\int_{300}^{T} \lambda_{Ce} dT$.

The only part of the program which has not yet had the effect of cesium incorporated is that arising from radiation transport, both P_T and λ_R. The present version of the program still contains the formulation appropriate to pure hydrogen. It was found in Chapter III of Ref. G-1 that cesium is a good radiator, so it will be necessary to modify the radiation terms to include the presence of cesium seed. This has not yet been done. Therefore, the use of cesium in the present version (September 1980) of the LSC wave program must be viewed with great caution. The radiation transport and loss terms will probably be under-estimated by an unknown amount. These radiation terms need to be re-formulated to make them valid for inclusion of cesium.

REFERENCES FOR APPENDIX G

G-1 Kemp, N.H. and Root, R.G., "Analytical Studies of Laser Supported Combustion Waves in Hydrogen," NASA CR-135349 (PSI TR-97), Woburn, MA, August 1977.

G-2 Kemp, N.H., Root, R.G., Wu, P.K.S., Caledonia, G.E., and Pirri, A.N., "Laser-Heated Rocket Studies," NASA CR-135127 (PSI TR-53), Woburn, MA, May 1976.

G-3 Raizer, Yu, P., "Subsonic Propagation of a Light Spark and Threshold Conditions for the Maintainence of Plasma by Radiation," Soviet Physics JETP, Vol. 31, December 1970, pp. 1148-1154.

APPENDIX H

MODEL FOR LASER SUPPORTED COMBUSTION WAVE HEATING WITH BUFFER GAS COOLING

One of the possible heating modes for a laser heated thruster is use of the laser supported combustion (LSC) wave mechanism. In this mode nearly all the laser energy absorption occurs in a few centimeters in an LSC wave, and a hot gas issues from the wave, with very little energy remaining in the laser beam. This hot gas must then be accelerated to produce thrust.

In a pure hydrogen LSC wave, the temperature of the hot gas is near 20,000 K, while for a cesium-seeded gas it may be somewhat lower. In either case, the gas is too hot to be in contact with the walls. One possible cooling method is to surround the hot gas with a co-flowing unheated annulus of buffer gas, which will act as an insulator between the laser-heated gas and the wall. This method of cooling can be modeled by combining the LSC wave model described in Appendix G with the thrust chamber design model described in Appendix E.

A diagram of the model is shown in Fig. H-1. An LSC wave of radius R_h stands at the entrance to the thrust chamber. Entering the wave is a laser beam of intensity I_o and a mass flow per unit area $\dot{m}_A = \rho_o u_o$ caused by an incoming stream of gas at temperature T_o, density ρ_o, pressure p_o and speed u_o. Also entering the thrust chamber is buffer gas flow, with the same properties and speed, in the annulus from R_h to R_m. However, this gas is not heated by the laser, since the laser beam is only of radius R_h.

At some point in the structure of the LSC wave we arrive at station A-A where we stop the LSC wave calculation and start the two-dimensional thrust chamber calculations. At present, this station is taken to be at the peak temperature of the LSC wave, though other choices could be made. It is desirable to have nearly all the laser energy absorbed by station A-A, or else further increases in temperature could occur in the thrust chamber.

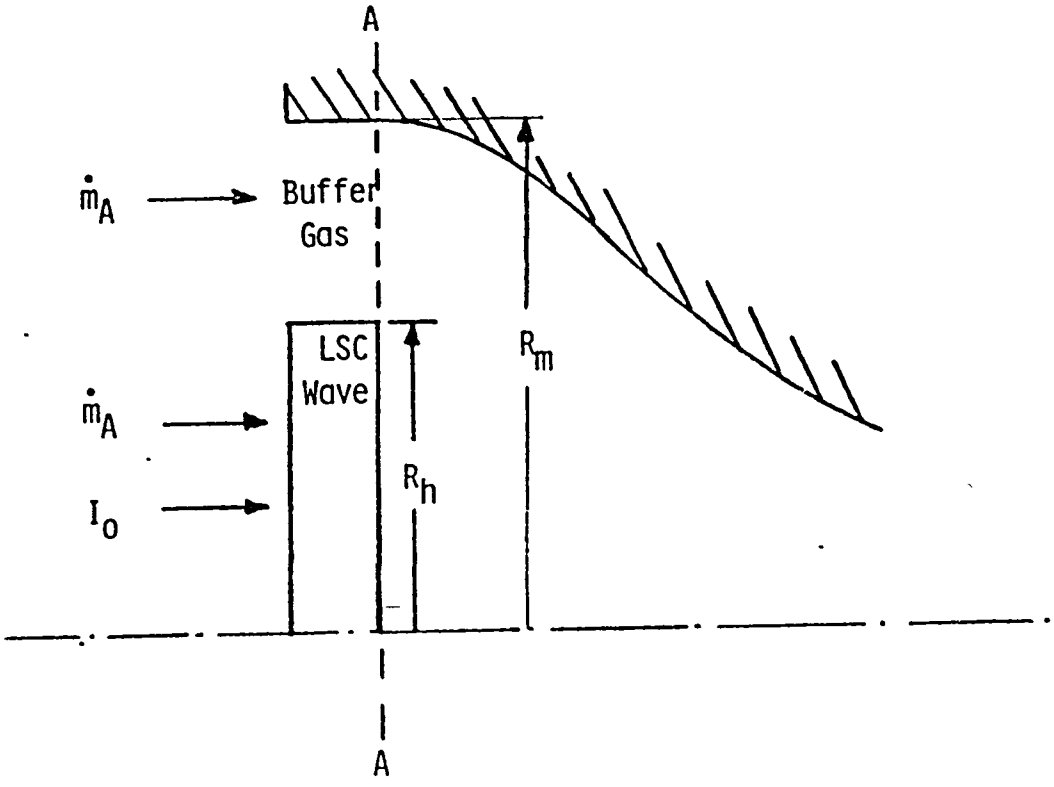

Figure H-1 Diagram showing coupling of LSC wave (Program LSCWCS) to thrust chamber (Program CLHTE). Station A-A is the initial station for Program CLHTE.

The conditions at the station A-A in the LSC wave (velocity, $\dot{m}_A$, temperature, pressure) are used as initial conditons for the start of the two-dimensional thrust chamber design calculation in the radius region up to R_h. In the annulus between R_h and R_m, the initial conditions are determined from the buffer gas flow. However, the incoming buffer gas conditions themselves are not used. Instead, the energy lost by transverse conduction from the LSC wave up to station A-A is added to the incoming buffer gas flow. The resulting gas conditions are used as initial conditions in the thrust chamber design calculation in the annulus from R_h to R_m.

The energy lost, per unit thickness of the LSC wave, in the transverse direction, is modeled in Appendix G as

$$\frac{dq}{dx} = \frac{C_{LC}}{R^2} \int_{T_o}^{T} \lambda_{Ce}\, dT + \frac{C_{LR}}{R^2} \int_{T_o}^{T} \lambda_R\, dT \qquad \text{(H-1)}$$

per unit transverse surface area. Thus, the total energy lost is

$$Q = \pi R^2 \int_0^{A\text{-}A} \frac{dq}{dx}\, dx \qquad \text{(H-2)}$$

where the integral is taken up to station A-A.

This energy is assumed to be absorbed by the buffer gas, which has a mass flow rate of $\dot{m}_A$ per unit area, through an annulus of area $\pi(R_m^2 - R_h^2)$. Then the additional energy per unit mass added to the buffer gas is

$$\frac{Q}{\dot{m}_A \pi (R_m^2 - R_h^2)} \equiv \Delta H \ . \qquad \text{(H-3)}$$

An energy balance for the buffer gas from inlet to station A-A is then

$$h_o + u_o^2/2 + \Delta H = h_{bf} + u_{bf}^2/2 \qquad \text{(H-4)}$$

where the subscript bf refers to the buffer gas at station A-A. Similarly, a mass balance requires

$$\dot{m}_A = \rho_o u_o = \rho_{bf} u_{bf} \cdot \qquad \text{(H-5)}$$

The pressure is assumed not to change through the LSC wave so $p_{bf} = p_o$. Since the caloric equation of state $h_{bf}(p_o, T_{bf})$ and the thermal equation of state $\rho_{bf}(p_o, T_{bf})$ are assumed known for the buffer gas mixture, Eqs. (H-3, H-4 and H-5) are sufficient to determine the state at station A-A when the incoming state $(\ )_o$ is known.

This procedure completely specifies the state of the gas at station A-A, the initial station of the thrust chamber design calculation. It consists of a hot core and a cool buffer annulus, both made of the same gas mixture. Then the flow equations specified in Appendix E can be applied to calculate the thrust chamber shape and heating.

It should be noted that the present (September 1980) version of the thrust chamber design computer code does not contain a radiation model for the high temperature (> 6000 K) gas emerging from the LSC wave. It should therefore be used with caution until such a model has been included.

APPENDIX I

EXPERIMENTAL EMEASUREMENTS OF ABSORPTION OF 10.6 μm RADIATION BY WATER VAPOR

Experimental Methodology and Limitations

An existing shock tube facility was used to measure the absorption coefficient of water vapor for 10.6 μm radiation at high temperatures. The shock tube is a well understood experimental tool and is ideal for creating the pressures and temperatures required for the proposed measurements. Small shock tubes are relatively inexpensive to operate and take the gas mixture almost instantly to a known high temperature and pressure. Test times up to a millisecond in duration are possible, which are more than sufficient to simulate the heating process in a laser-heated thruster.

As shown in Fig. I-1, a shock tube consists of a high pressure section and a low pressure section separated by a diaphragm. When the diaphragm bursts, the high pressure gas flowing into the low pressure section acts as a piston, compressing and accelerating the low pressure gas ahead of it. Processing of the low pressure gas is accomplished by a shock wave which travels ahead of the piston. When the shock wave passes through the test section at the end of the shock tube, it reflects off the end wall and reshocks the previously shocked gas, compressing it further. It is usual to specify the conditions in the high pressure region (the driver gas) by the subscript 4, conditions in the undisturbed low pressure section (the driven gas) by subscript 1, the gas conditions behind the incident shock wave by subscript 2, and behind the reflected shock wave by subscript 5. This is shown in the position versus time plot (Fig. I-1b). Measurements are made in the test section in regions labeled 2 and 5.

The shock wave heats the processed (or driven) gas, resulting in an enthalpy per unit mass Δh, which is easily and accurately calculable when the shock velocity U_s is known. The enthalpy of the processed gas is approximately doubled when the shock wave is reflected off the end wall. High temperatures require a high enthalpy per unit mass, thus implying high shock

THE SIMPLE SHOCK TUBE

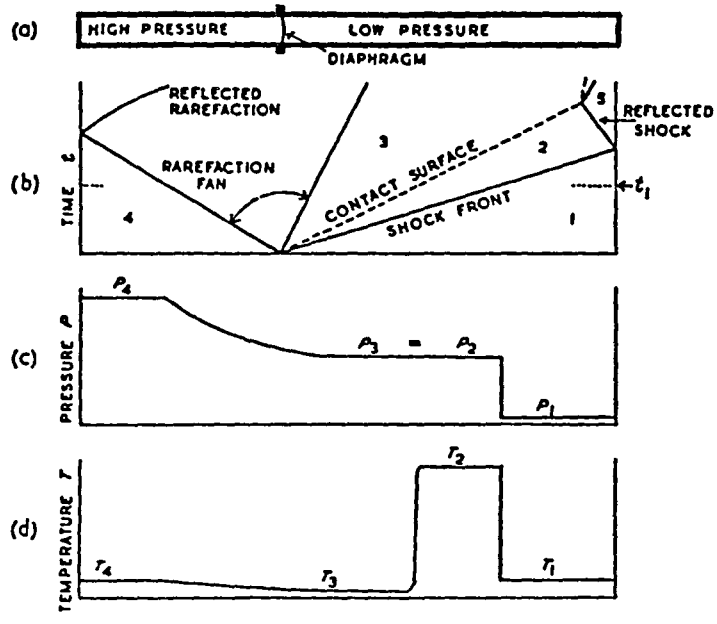

(a) *Conventional shock tube* (b) *An* $(x-t)$ *diagram showing progress of the shock wave, the rarefaction fan and the contact surface separating driver and experimental gases* (c) *The pressure distribution along the tube at time* t_1 (d) *The temperature distribution at time* t_1

Fig. I-1 (from Ref. I-1)

velocities. The velocity of the gas piston increases as the pressure ratio across the diaphragm increases but cannot exceed a value of a few times the initial sound speed in the driver gas ($U_{piston} < \frac{2}{\gamma-1} a$, where γ is the specific heat ratio and a is the sound speed in the driver gas), even with an infinite pressure ratio. Therefore, driver gases with high sound speeds are desired. Most shock tube drivers use hydrogen, and in the PSI shock tube, room temperature hydrogen at up to 200 atmospheres pressure is used.

An idealized representation of the temperature, pressure and laser energy transmitted which will be observed at the test section is shown in Fig. I-2. Until t_i, when the incident shock passes, the low values of temperature and pressure of the quiescent driven gas are observed, together with the incident laser intensity I_o. When the incident shock passes, at t_i, the temperature and pressure rapidly rise to the higher values T_2 and p_2. The transmitted laser intensity, I_t, is reduced because of the absorption in the shocked gas. When the reflected shock passes, at t_r, a second jump in temperature and pressure occurs, to T_5 and p_5. The transmitted laser intensity again drops because of further absorption in the hotter, higher pressure gas behind the reflected shock.

When performing an experiment in water vapor, there are limitations on the choice of initial pressure in the driven gas (region 1 in Fig. I-1b). The initial pressure in this low pressure section of the shock tube is determined by the allowable range for the partial pressure of water vapor. The low pressure limit is determined from the requirement that any condensed water on the shock tube walls must not affect the measured water vapor mole percent of the gas in the tube. At low partial pressures of water vapor there will be at most a monolayer of water due to chemisorption, and we have estimated (using theories of Langmuir, Brunauer, Emmett and Teller in Ref. I-2) that van der Waals forces also yield a monolayer of water molecules on the shock tube walls. To eliminate any effect of this monolayer on the gas in the tube, we have calculated that the partial pressure of water vapor in the driven gas must be greater than 10^{-3} atm.

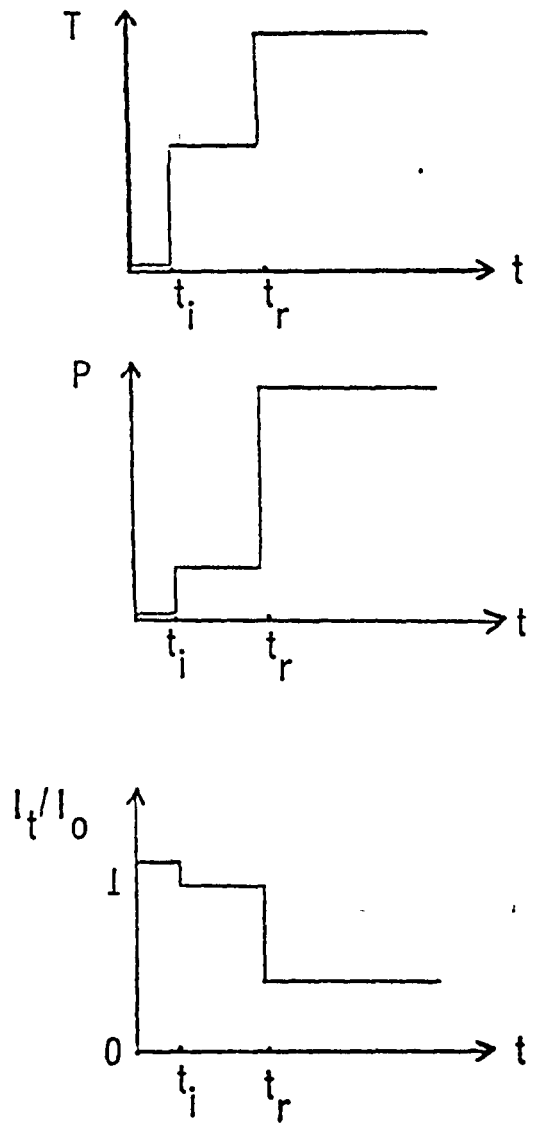

t_i - arrival time of incident shock at test station

t_r - arrival time of reflected shock at test station

Fig. I-2 Idealized temporal profiles of temperature, pressure, and transmitted beam intensity for test station near end wall.

Similarly, if the pressure in the low pressure section is raised to the point where the vapor pressure of water exceeds the saturation vapor pressure at the coldest point in the system, water will condense out at that point, again making it difficult to control the amount of water in the tube. Therefore, the maximum vapor pressure of water is limited to 2×10^{-2} atm, the saturation vapor pressure at 20^{o}C.

Within these high and low pressure limitations, we have determined the range of temperatures and pressures attainable in the shock tube by performing a series of calculations for the water vapor mixtures using chemical equilibrium computer codes to determine the pressure and temperature behind the incident and reflected shocks (regions 2 and 5 in Fig. I-1b). The results of these calculations are presented in Figs. I-3 and I-4. Calculations were made of the pressure and temperature behind the incident and reflected shocks for numerous water vapor mixtures. The mole percent of the water vapor was varied from 2% to 16%. An example result for 10% H_2O in H_2 is presented in Fig. I-3. In this plot the pressure p_2 denotes pressure behind the incident shock and p_5 denotes the pressure behind the reflected shock. The pressure and temperature behind these shocks are increased by increasing the driver pressure (and thus, the shock strength). The upper limit to the pressures is reached with the driver pressure at 200 atm. Lines are drawn corresponding to the two limiting values of the initial <u>total</u> pressure in the low pressure section (i.e., p_1 = .01 atm corresponds to the 10^{-3} atm H_2O partial pressure minimum). By connecting the maximum pressure points for the two limits on p_1, we can define operating regimes for the shock tube. These regimes are shaded in Fig. I-3 for both the incident and reflected shocks.

It can be seen that the mixture of H_2O and H_2 permits operation up to 1600 K behind the incident shock and up to 2900 K behind the reflected shock.

A similar plot for a mixture of 10% H_2O in argon is shown in Fig. I-4. This shows a much increased temperature range, up to more than 6000 K. It is easier to raise the temperature of the heavy gas argon than the light hydrogen because the speed of sound is lower in argon.

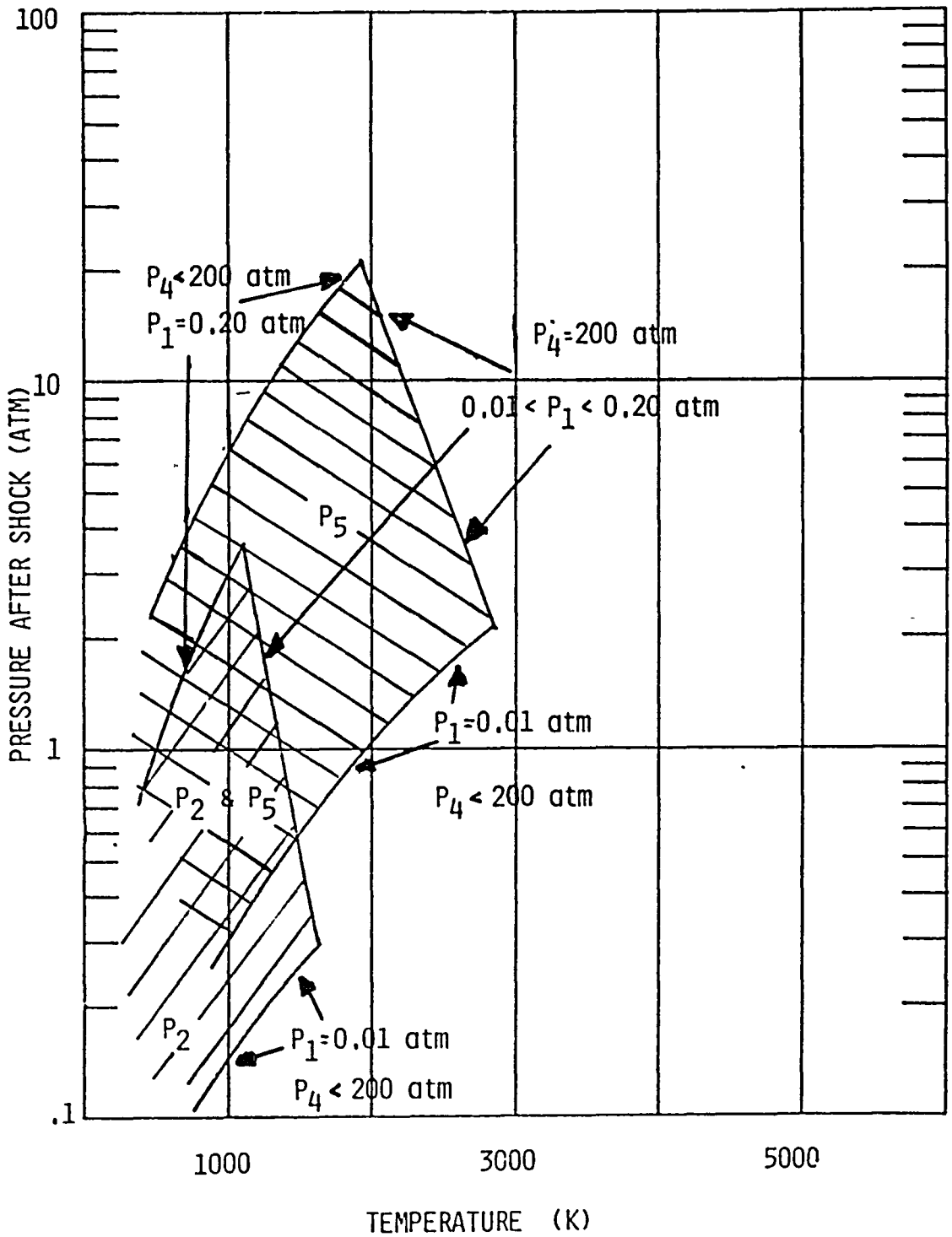

Fig. I-3 Pressure-temperature region which can be reached in a 10% H_2O/90%H_2 gas mixture.

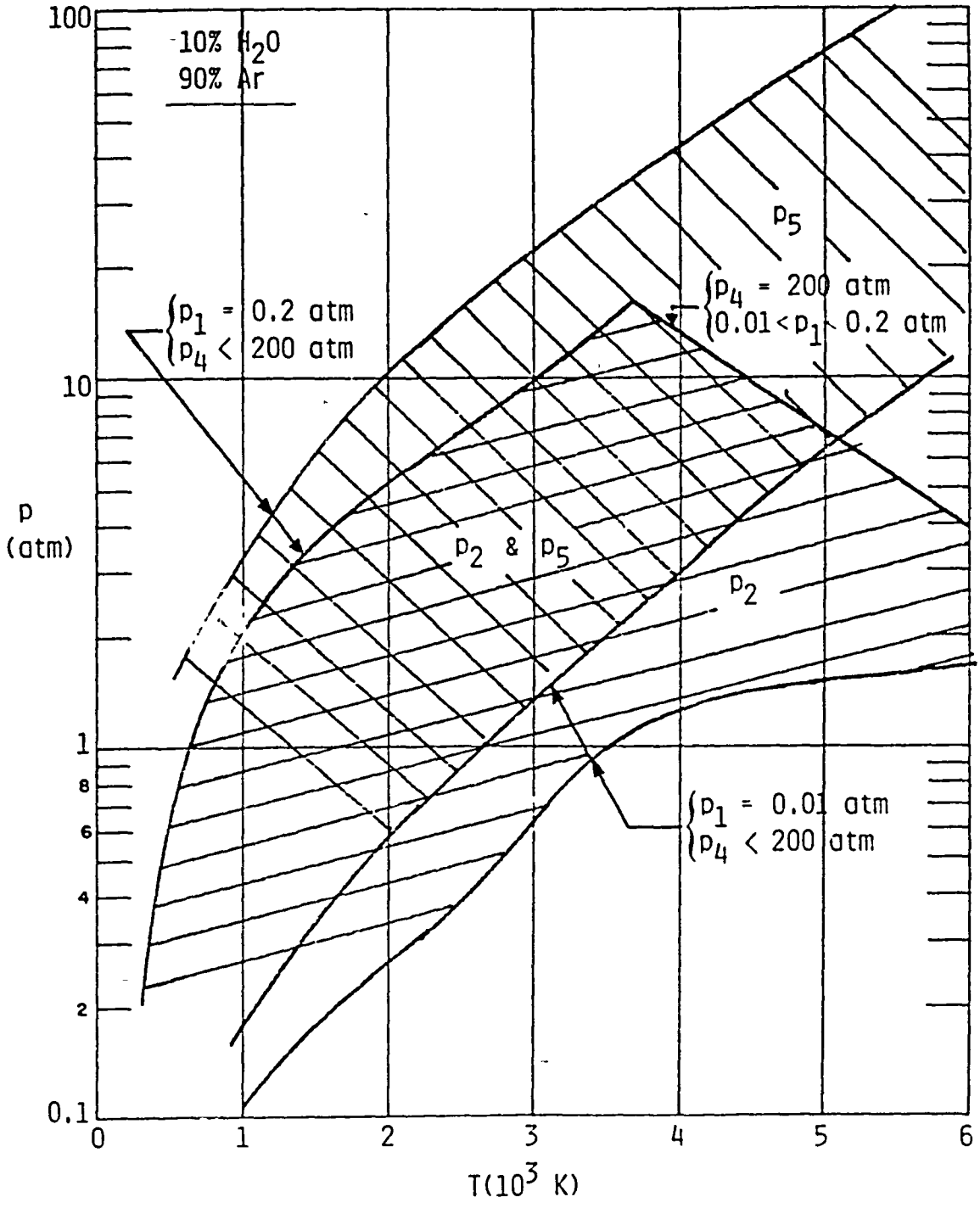

Fig. I-4 Pressure temperature region which can be reached in a 10% H_2O/90% Ar gas mixture.

The preliminary experiments reported here were performed in water-argon mixtures, to take advantage of the higher temperatures which could be reached. For laser propulsion applications, hydrogen is the most desirable propellant so water-hydrogen mixtures are of the most interest. This brings up the question of the relation between the absorption coefficients measured in water-argon mixtures and those which would occur in water-hydrogen mixtures at the same temperature and with the same partial pressure of water vapor.

At low temperature and atmospheric pressure the absorption coefficient is strongly dependent upon the location of the laser line being absorbed relative to the center of the molecular absorption lines of the water vapor molecule. The width of these absorption lines are dependent on the collision partner, i.e., the diluent gas. This would seem to indicate that the measured absorption coefficient could be strongly dependent upon whether argon or hydrogen is the collision partner. However, the number of populated states, and the density and the widths of the molecular absorption lines increase substantially at elevated temperatures and pressures. Therefore, the lines overlap and the collision partner dependence of the absorption coefficient will become less and less important as the pressure and temperature is increased.

Under the present program, experiments were made using the P(20) laser line, with argon as the collision partner. The experiment is being continued at PSI under different sponsorship, and the dependence of water vapor absorption coefficient on both collision partner and laser line will be explored in that program.

The shock tube operating regime must be combined with the constraints resulting from the minimum measurable amount of the absorption which takes place. This constraint places an additional limit on the range of allowable water vapor pressures. There must be sufficient absorption by the H_2O vapor so that it can be accurately measured. The minimum absorption we can measure is 1% of the probe laser intensity. For the shock tube diameter of 3.8 cm, we then need an absorption coefficient k such that $3.8k = 0.01$.

From the literature, we have estimated the absorption coefficient of water vapor (Ref. I-3) and the results are shown in Fig. I-5. From this figure we can find the partial pressure of water vapor at any temperature which will give a value $k = 0.01/3.8 = 0.00263\ cm^{-1}$. Figure I-6 shows the result of such a calculation. Two curves are shown; one assumes that the water molecules remain water molecules even at high temperatures; (that is, the chemistry is "frozen") and the other assumes that the chemistry is in equilibrium. The latter curve should apply everywhere except very near the shock front. With this curve the required vapor pressure starts low at room temperature because the water vapor continuum is helping absorb, and rises until lines become important; then the required pressure falls. It continues to fall until the temperature reaches 2500 K, at which point the water molecule begins to dissociate and the required initial water vapor pressure must rise again. For frozen chemistry the pressure also rises slightly at high temperature. By operating the shock tube with partial pressures of water above the equilibrium curve in Fig. I-5, more than 1% absorption will occur, which should provide sufficient measurement accuracy.

Absorption by water molecules condensed on the windows, through which the absorption measurement will be made, places another limit on the permissible operating partial pressures of water. Liquid water has a large absorption coefficient for 10.6 μm radiation, with a value of k greater than $10^3\ cm^{-1}$; therefore, water must not be allowed to condense onto the windows. Although the initial gas sample will have a sufficiently low partial pressure of water, the shock wave raises this pressure by large factors. This is, of course, no problem in the middle of the shock tube where the gas is hot; however, the gas near the wall, which is at this same high pressure, is at or near the temperature of the wall. Since the saturation vapor pressure of water is a steep function of temperature, warming the test section wall can prevent condensation. The vapor pressure of water as a function of temperature is as follows:

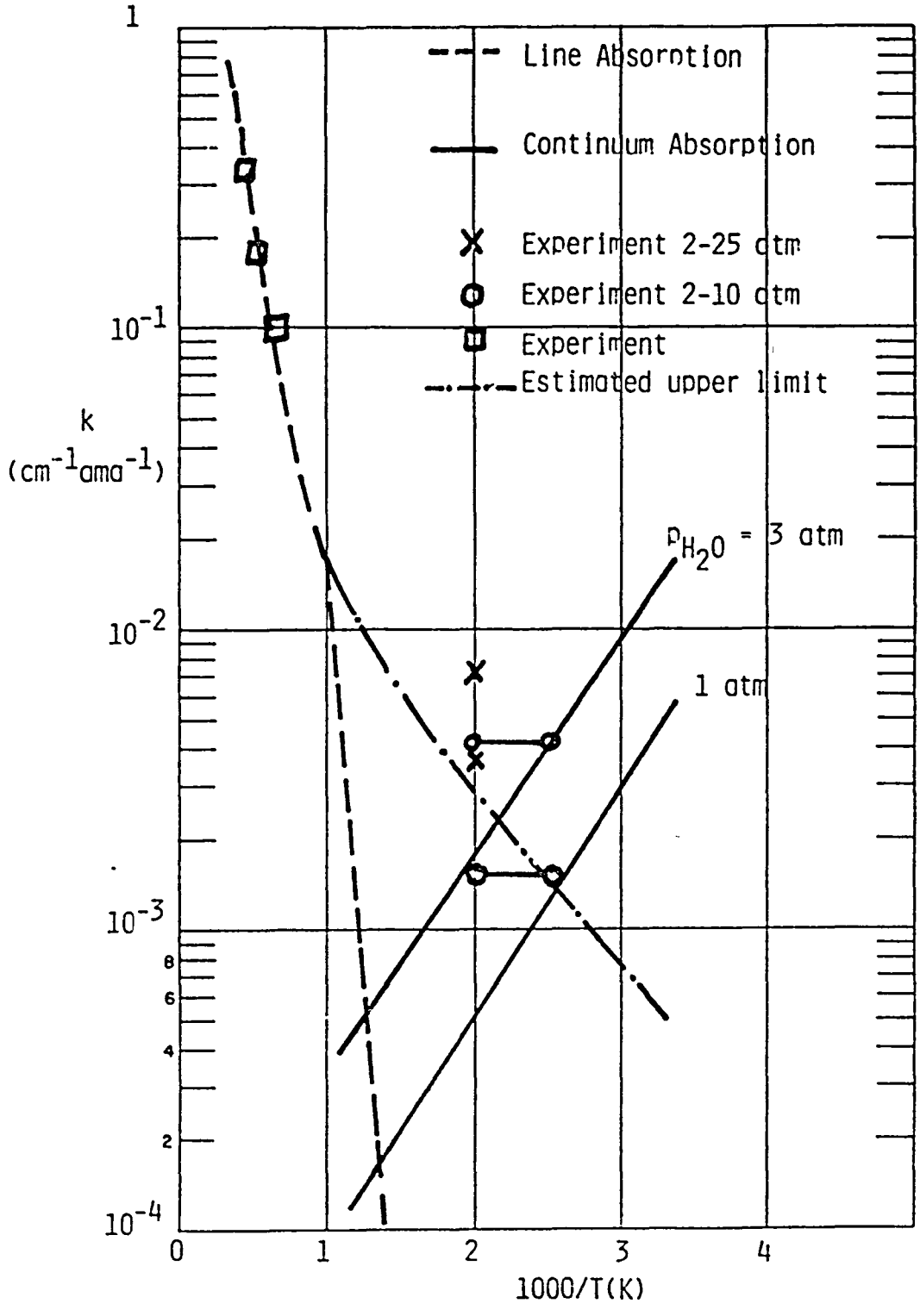

Fig. I-5 Absorption coefficient of 10.6 μm radiation in water vapor.

Vapor pressure p_s = 0.02 atm @ 293 K
0.12 atm @ 323 K
1.0 atm @ 373 K
2.5 atm @ 400 K
4.7 atm @ 423 K

From these values of water vapor pressure, we observed that if the wall temperature could be maintained around 400 K, then condensation would not occur near the windows under experimental conditions. This approach was used early in the program; however, the shock tube overheated, resulting in the melting of several piezoelectric pressure transducers and O-ring vacuum seals. Programmatic constraints did not allow for a major heating system redesign so the heating was reduced to 310 K. At this temperature, the partial pressure of water vapor behind the reflected shock is much greater than the saturation pressure and the effect of condensation (in the cold boundary layer near the windows) had to be investigated. The results of the worst case conditions are presented below.

In the shock tube the separation distance between the shock and the contact surface (region 2) approaches a limiting value because of the wall boundary layer (Ref. I-4). In addition, the cold boundary layer, if it is thick enough, will absorb laser radiation in a manner different from the uniform hot gas in the center of the tube. It is necessary to estimate the contribution of this boundary layer to the overall absorption measurement.

Studies of the wall boundary layer in a shock tube have been reported by many investigators (Refs. I-5, I-6 and I-7). Here we will use the Mirels and King series expansion solution (Ref. I-7) to estimate the wall boundary layer contribution to the absorption of laser radiation. Consider the case of a free stream temperature of approximately 600 K in region 2, and a pressure of one atmosphere. This can be considered the most serious case for boundary layer contributions because the absorption coefficient of water vapor at the laser wavelength has a minimum at about 600 K (Fig. I-5). Thus, the absorption coefficient in the boundary layer is higher than in the center of the tube. The mixture is taken to be 20% H_2O and 80% H_2. The

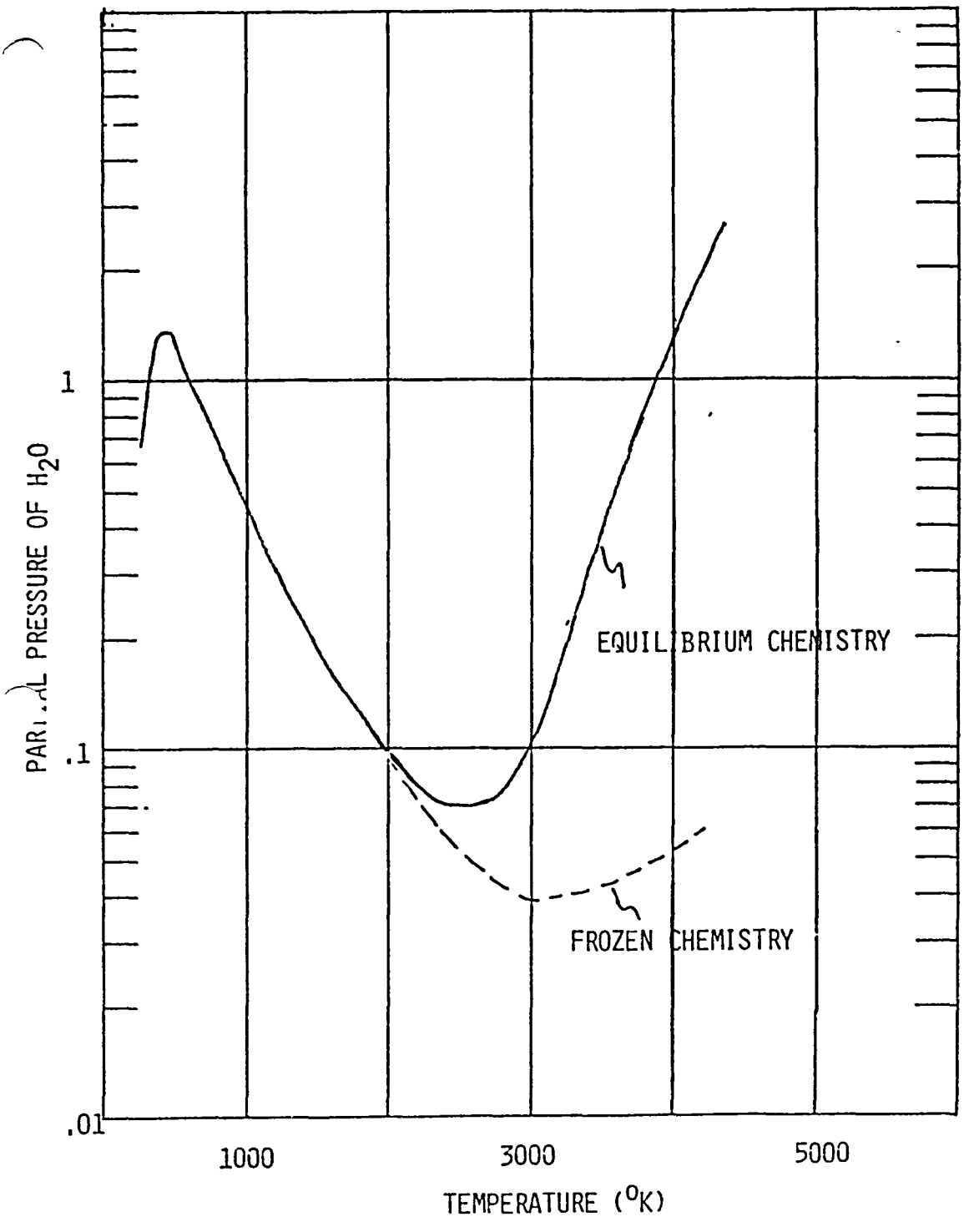

Fig. I-6 Conditions which produce 1% absorption in water vapor.

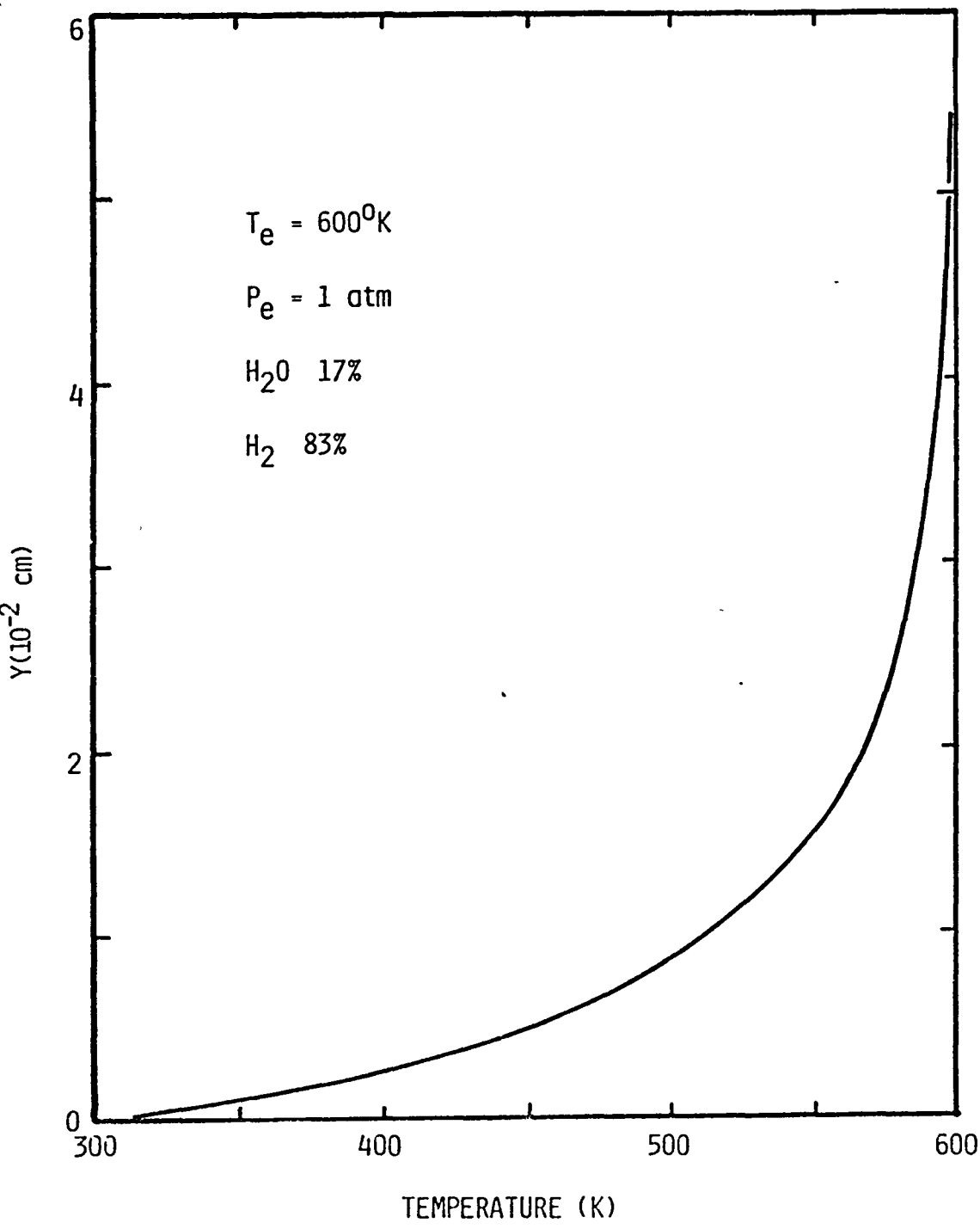

Fig. I-7 Shock tube boundary layer temperature profile at X = 4.2 cm.

experimental test time will be ≃ 20 μsec with a shock speed of approximately 2.1×10^5 cm/sec (from a shock tube calculation). We will calculate the wall boundary layer profiles at a distance of 4.2 cm from the shock.

From the zeroth order solutions, we find that the boundary layer thickness at 4.2 cm behind the shock is approximately 4.5×10^{-2} cm (2.4% of the shock tube diameter). In order to estimate the wall boundary layer contribution to the overall absorption of laser radiation, the temperature profile at X = 4.2 cm, where X is distance behind the shock, is also needed and shown in Fig. I-7. We can evaluate the integral $\eta \cong \int k\, dy$ where k(T) and y are the absorption coefficient of water vapor and the normal distance from the wall, respectively. For the free stream portion (in the tube center), $\eta \cong 7. \times 10^{-4}$. The wall boundary layers give $\eta \cong 1.2 \times 10^{-5}$ and this is approximately a 1.7% effect. The above calculation is for a pressure of 1 atm. As the pressure is raised to 50 atm while the temperature is maintained at 600 K, the wall boundary layer contribution to the laser radiation absorption becomes approximately 12 percent. Therefore, we conclude that boundary layer effects will not seriously influence the accuracy of the absorption measurement.

Experimental Apparatus

Figure I-8 is a photograph of the 1.5" I.D. shock tube during the set-up period for the NASA water vapor absorption coefficient measurements. In the foreground is the driver, connected to the 22' long driven section. At the far end there is a 10" long test section where measurements are made and finally a 9 cubic foot dump tank is used to bleed the tube to atmospheric pressure after a shot. The line tunable CW CO_2 laser and the optical detection system are located on the table perpendicular to the tube at the test section. Behind the table is the power supply for the laser. The laser absorption measurement system will detect a 1% change in absorption. (The heating tapes to raise the wall temperature had not been installed when the photograph was taken.) Also located on the table but not readily visible is a 0.25 m Jarrell-Ash Spectrometer used for laser wavelength calibrations and a Scientech power meter to measure the laser output.

Fig. I-8 The PSI 1.5 Inch Shock Tube Facility

Figure I-9 is a schematic representation of the shock tube gas handling system. Gas mixtures used in a test are prepared in the mixing tank. The tank is heated to prevent condensation of H_2O, and can be evacuated to a hard vacuum with the diffusion dump. The water is added from a flask through a valve at one end of the tank. The water vapor pressure is monitored by a Validyne DP-7 variable reluctance pressure transducer. Diluent gas is then added to the water vapor by injection through a spray bar located on the central axis on the tank, and the total pressure of the gas is measured.

The pressure in the driven section of the shock tube is monitored by a thermocouple gauge before filling. Gas from the mixing tank is valved into the tube and the pressure is monitored by the Validyne transducer.

The driver is evacuated to a rough vacuum before pressurization. Driver gas is supplied by a six cylinder manifold, and the fill pressure is monitored by a Bourdon-type pressure gauge equipped with a check valve to hold the diaphragm burst pressure. When the diaphragm bursts, the shock wave is created and propagates through the driver section toward the test section. The pressure behind the shock wave was originally measured by seven piezoelectric transducers at 2.5 ft intervals upstream of the test section, and the shock velocity was determined by measuring the time interval between successive pressure transducers. After the tube overheated and damaged the transducers, the shock speed was determined by measuring the shock transit time between one transducer upstream of the test section and the main transducer at the test section.

The test section and absorption measurement system are located at the end of the driver section and are shown schematically in Fig. I-10. The output of a PSI-built line-tuned single mode CW CO_2 laser is directed through the test section to measure the absorption in the shocked gas. The windows in the test sections were 3/4" in diameter by 0.2" thick zinc sulfide. Originally NaCl windows were used; however, the thermal shock caused surface crazing after only one shot.

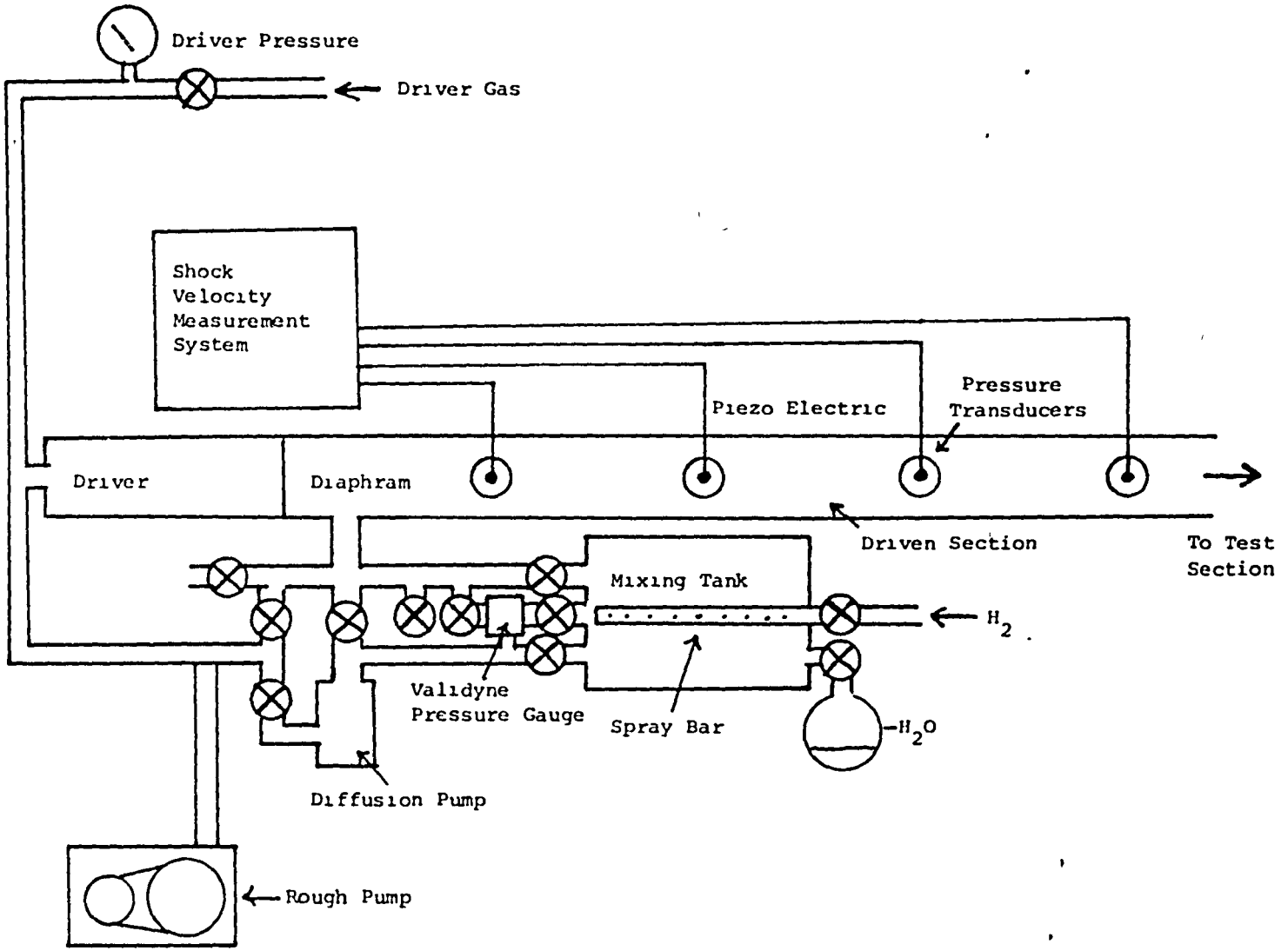

Fig. I-9 Schematic of shock tube gas handling system

A HgCdTe detector was used to monitor the absorption of the hot gas during a shot. Before the shot, the beam was blocked to obtain the 0% transmission level; no absorption is observed in the cold gas. A Kistler piezoelectric pressure transducer measures the pressure history in the test section during the absorption measurement. An end wall is located 1.5" downstream from the windows to create the reflected shock; this allowed sufficient time for measurements behind the incident shock. Idealized traces of the temperature, pressure and absorption in the test section are shown in Fig. I-10.

After the experiment, the gas in the tube automatically bleeds into the dump tank through a check valve, eliminating the need for a downstream diaphragm. The data was collected by a CAMAC data acquisition system and processed by the PSI PRIME 400 computer after each shot.

Experimental Results and Discussion

Shock tube runs were conducted in H_2O/Ar mixtures to measure the absorption coefficient of water vapor. In the early checkout runs, large fluctuations in the transmitted laser beam intensity were observed, with a 10 to 20 μs period, after the gas was shock-heated.

Two possible sources of these fluctuations were identified. One was a 7% increase in the cross-sectional area of the shock tube in the test section, where flat windows were mounted in the walls of a round tube. The passage of the incident and reflected shock waves through this area generates weak secondary waves which could cause small density changes in the hot gas. This in turn could cause changes in the index of refraction of the gas, move the transmitted laser beam around on the detector, and cause fluctuations in the signal measured.

A second possible cause could be a parasitic coupling of the disturbances in the hot gas to the gas in the laser cavity, causing fluctuations in the laser output.

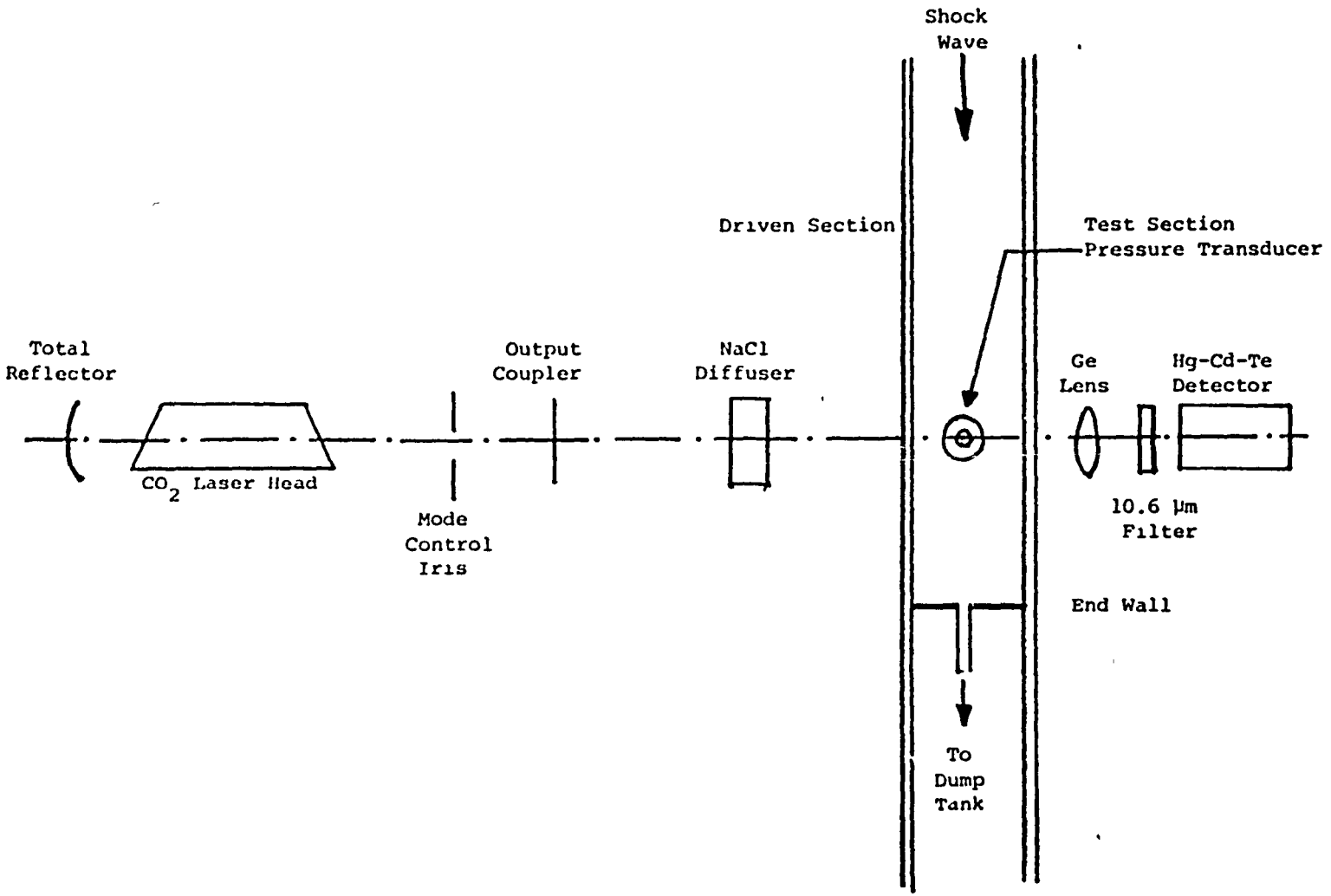

Fig. I-10 Schematic diagram of the IR absorption measurement system.

In the present program it was not possible to design and build a new test section to eliminate the area change, so both problems were attacked by a reconfiguration of the optical system. The collimated laser beam was diffused by inserting a roughened NaCl flat in the beam before it entered the test section. A lens was used to image the center of the test section onto the detector. The optical diffuser decouples the laser from the test gas to reduce the possibility of parasitics being generated. Diffusion of the laser beam illuminates the test section more uniformly and reduces the effect of local density fluctuations on the beam.

This optical configuration reduced the fluctuations to a few percent of the transmitted beam intensity. However, it also reduced the transmitted intensity sufficiently that broad-band emission from the hot gas in the test section, after the reflected shock, was comparable to the original laser intensity. To reduce this emission, the optical bandwidth of the detection system was reduced by inserting a 10.6 μm (1.7 μm FWHM) interference filter in front of the detector. The hot gas emission was substantially reduced, but not eliminated by the filter. To further reduce emission effects, the data runs were made by performing two identical shots at each experimental condition, one with the laser off to measure gas emission, and one with the laser on to measure both gas emission and transmitted beam intensity. Subtraction of the detector signal for the two runs yielded the actual absorption.

The temperature and pressure of the test gas was calculated using the measurement of the incident shock velocity. This measurement was made in the uniform portion of the shock tube upstream of the test section. However, the gas in which the absorption was observed was processed after the shock moved into the test section, where the area increased by 7%, which caused the shock to slow down. A small correction was applied to the measured shock velocity to account for this slowdown.

The correction was obtained from the theory of shock dynamics in channels of varying area (Ref. I-8), which expresses the change in shock Mach number from an original value M_o to a new value M, when the area changes from an original value A_o to a new value A. The expression for the new Mach number is

$$M = M_o - \frac{A-A_o}{A} \frac{1}{g(M_o)}$$

where

$$g(M_o) = \frac{M_o}{M_o^2-1} \left(1 + \frac{2}{\gamma+1} \frac{1-\mu_o^2}{\mu_o}\right)\left(1 + 2\mu_o + M_o^{-2}\right)$$

$$\mu_o^2 = \frac{(\gamma-1)M_o^2 + 2}{2\gamma M_o^2 - (\gamma-1)}$$

The temperature and pressure changes are then found by perturbing the equations for temperature and pressure jump across a shock wave.

A typical computer output trace of the pressure measured in the test section is shown in Fig. I-11, with the jumps at the incident and reflected shocks clearly visible. Also shown is the detected signal with the probe laser off. The signal shows a slight increase when the reflected shock arrives, due to hot gas emission. The second shot of this pair of shots, with the laser on, is shown in Fig. I-12. The pressure trace is nearly identical. The 100% laser transmission line is shown, together with the measured trace. A small amount of reduced transmission (absorption) is seen after the incident shock, and a much larger amount after the reflected shock. The figure shows that the level of the transmitted signal still varies, so a value was determined by averaging over 50 μs of digitized data (50 points in Fig. I-12).

Five shots have been made by the method described, and for each shot a measurement was made behind the incident shock and the reflected shock. The results are shown in Fig. I-13. The points labeled 2 are incident shock measurements, and those labeled 5 are reflected shock measurements. These results, and their relation to the values used in the modeling, are discussed in the main body of this report in Chapter IV. Table I-1 presents the results in tabular form.

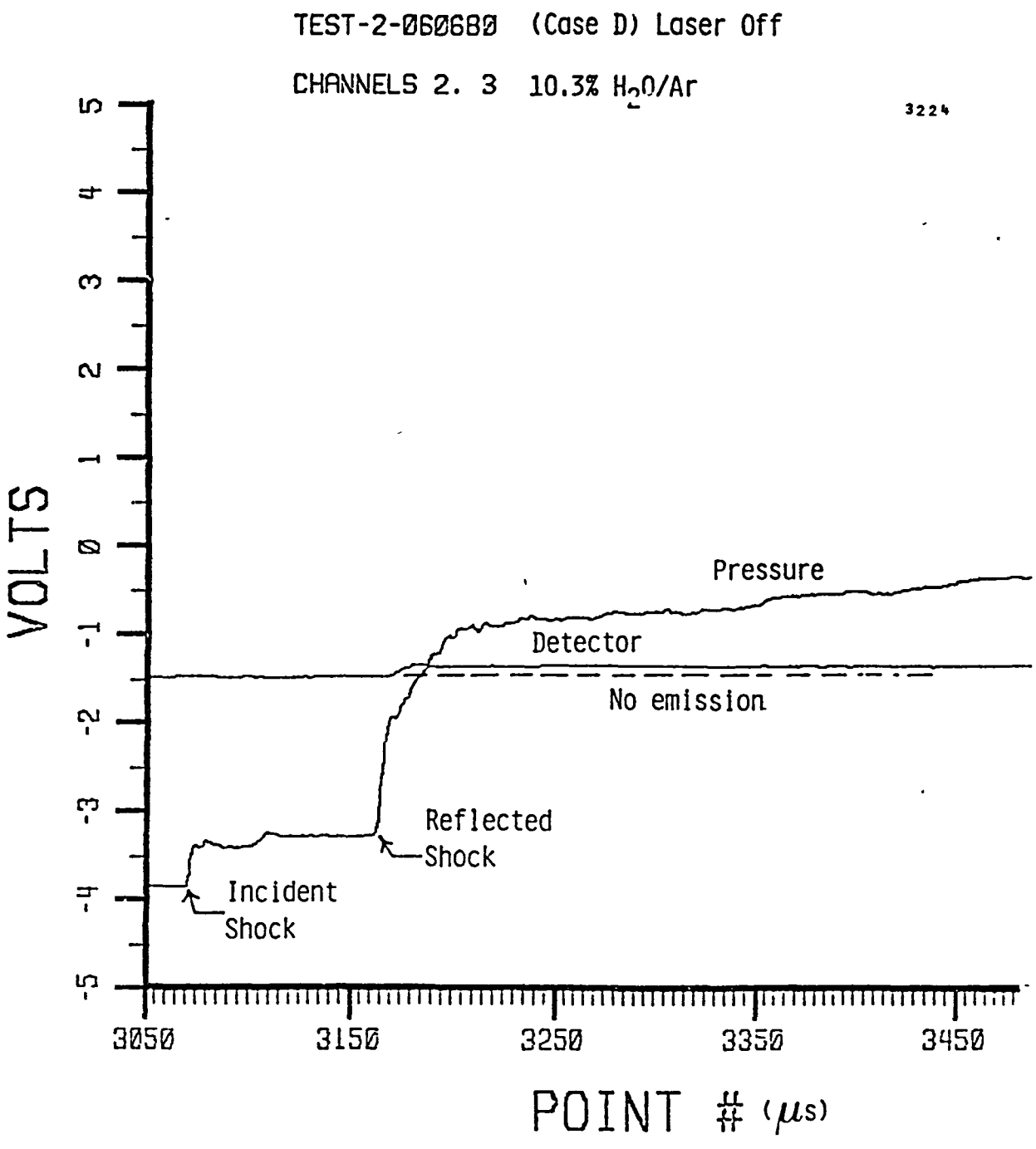

Fig. I-11 Experimental pressure and detector traces with probe laser off.

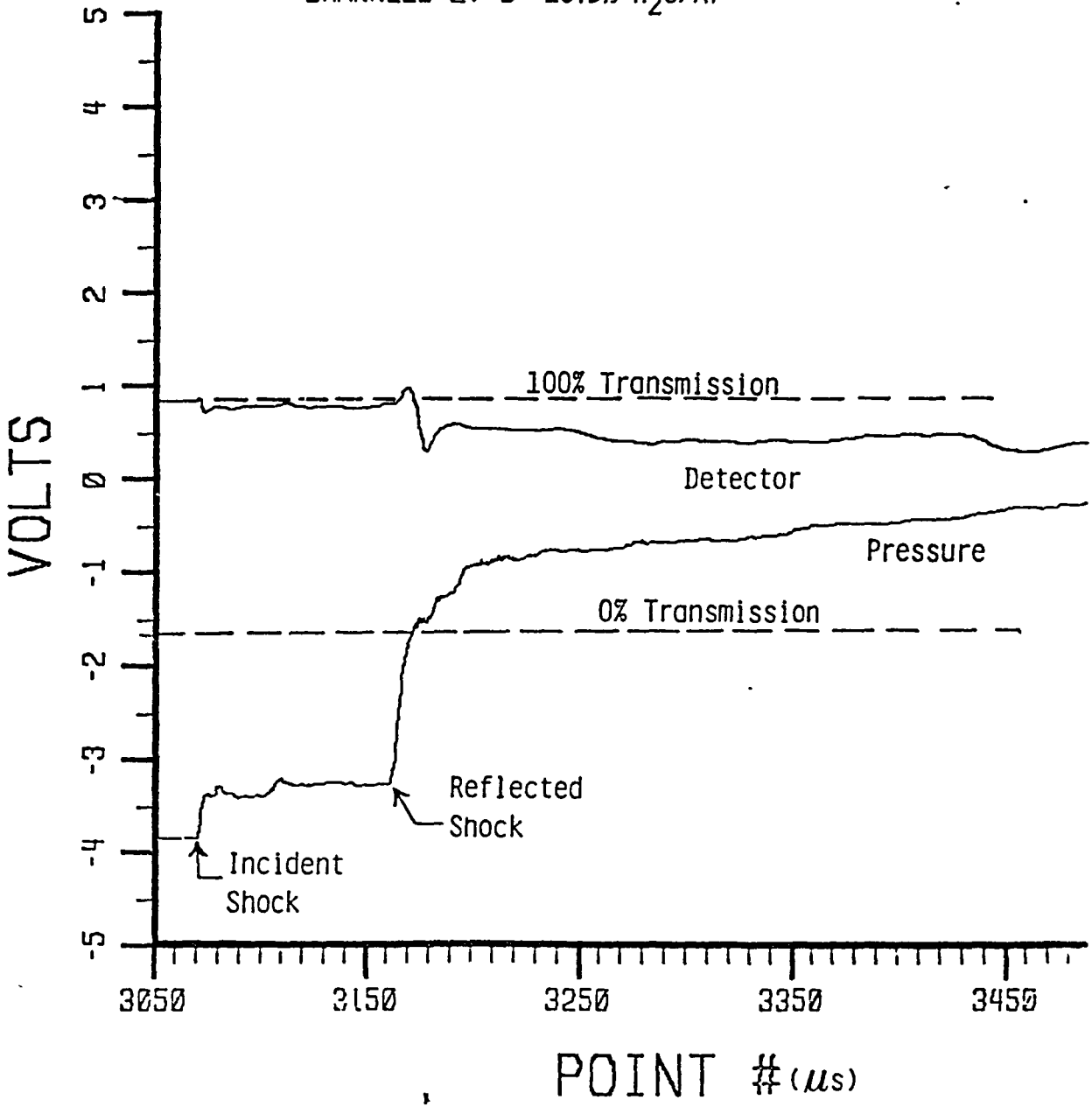

Fig. I-12 Experimental pressure and detector traces with probe laser on.

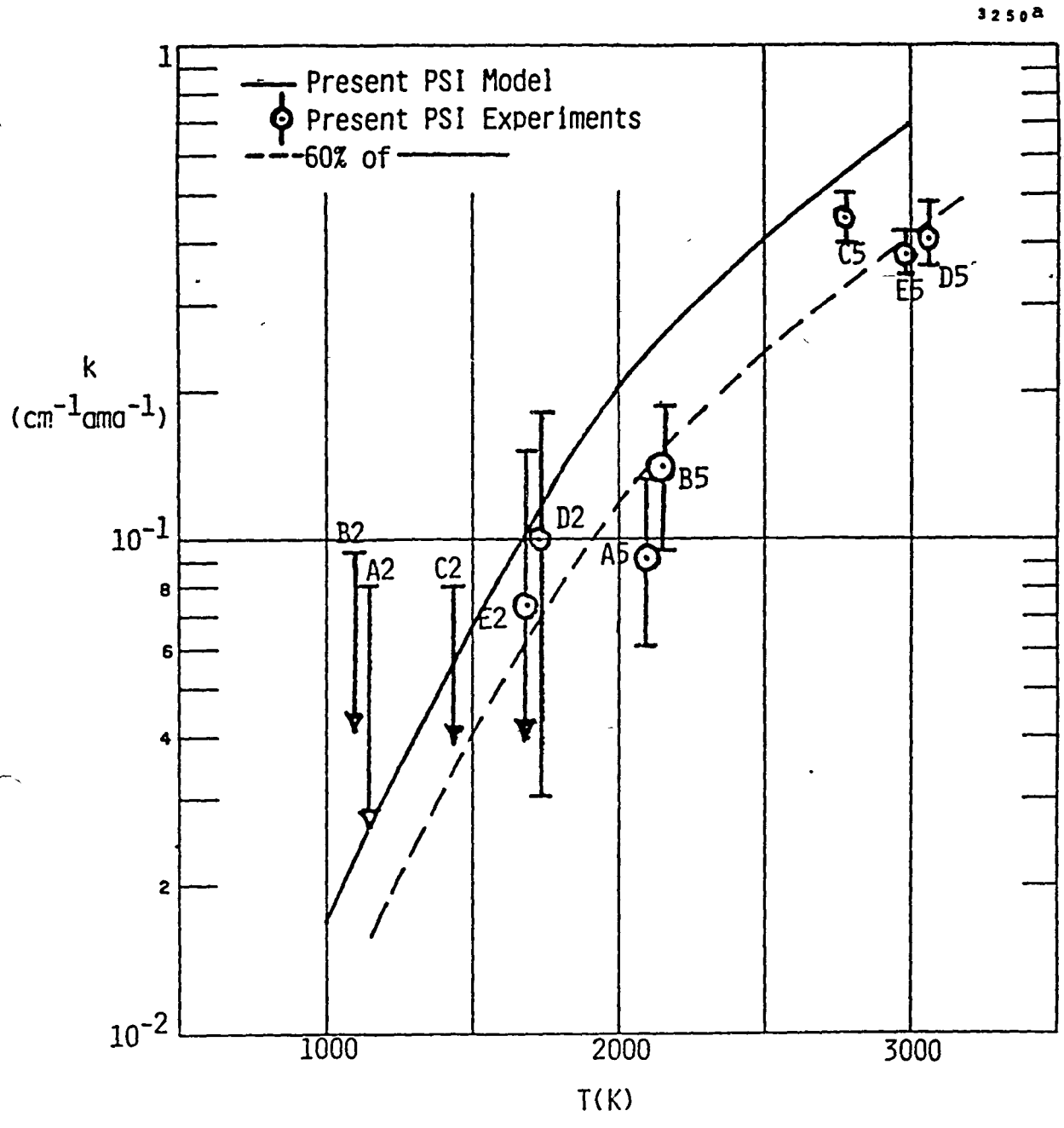

Fig. I-13 Measurements of the absorption coefficient of 10.6 μm taken at the P(20) line in water vapor from the present experiments.

TABLE I-1

EXPERIMENTAL PARAMETERS

Run	Gas Composition
A	16.7% H_2O in Ar
B	2.00% H_2O in Ar
C	4.96% H_2O in Ar
D,E	10.3% H_2O in Ar

Incident Shock Conditions

Run	T_2 (K)	p_2 (atm)	ρ_{H2O} (ama)	% Trans	k ($cm^{-1}ama^{-1}$)
A	1148	1.69	0.0664	>99	<0.040
B	1106	11.3	0.0566	>99	<0.047
C	1435	7.02	0.0663	>99	<0.032
D	1721	4.50	0.0733	97.2	0.10
E	1681	4.38	0.0729	98.0	0.073

Reflected Shock Conditions

Run	T_5 (K)	p_5 (atm)	ρ_{H2O} (ama)	% Trans	k ($cm^{-1}ama^{-1}$)
A	2101	8.04	0.171	94.2	0.092
B	2146	49.0	0.123	93.7	0.14
C	2770	33.4	0.141	78.5	0.45
D	3064	22.8	0.162	77.9	0.41
E	2999	22.1	0.167	77.8	0.38

The error bars shown are those due to an estimated 2% error in reading the transmitted laser intensity. They do not account for signal fluctuations, or possible errors in the temperature and pressure corrections due to the area change in the test section.

As mentioned above, this experiment is continuing at PSI under other sponsorship. In that work a new test section will be used, and other experimental problems will be eliminated. The present results should be looked upon as preliminary. They do, however, provide encouraging evidence that the absorption coefficients used in the modeling are within a factor of 2 of the actual values.

REFERENCES FOR APPENDIX I

I-1 Gaydon, A. G. and Hurle, I. R., The Shock Tube in High Temperature Chemical Physics, Reinhold Publishing Corp., New York, 1963, p. 1.

I-2 Adamson, A. W., Physical Chemistry of Surfaces, Interscience Publishers, John Wiley & Sons, New York.

I-3 Kemp, N. H. and Lewis, P. G., "Laser-Heated Thruster Interim Report," Contract NAS8-33097 (PSI TR-205) Woburn, MA, February 1980.

I-4 Duff, R. E., "Shock-tube Performance at Low Initial Pressure," Phys. Fluids, Vol. 2, 207-216, 1959.

I-5 Roshko, A., "On Flow Duration In Low Pressure Shock Tubes," Phys. Fluids, Vol. 3, 835-842, 1960.

I-6 Mirels, H., "Shock Tube Test Time Limitation Due to Turbulent-Wall Boundary Layer," AIAA Journal, Vol. 2, 84-93, 1964.

I-7 Mirels, H. and King, W. S., "Series Solutions for Shock Tube Laminar Boundary Layer and Test Time." Aerospace Corp. Dept. TDR-469 (5240-10)-15, June 1965.

☆US GOVERNMENT PRINTING OFFICE 1981-740-066/379 REGION NO 4

END

DATE

FILMED

JUN 12 1981

End of Document